Reduced Mode Sapphire Optical Fiber and Sensing System

Final Scientific/Technical Report

DOE Award Number:	DE-FE0012274
Sponsoring Program Office:	National Energy Technology Laboratory
Technology Area:	Plant Optimization Technologies
Recipient Organization:	Virginia Polytechnic Institute & State University Office of Sponsored Programs Research Building XV 1880 Pratt Drive, Suite 2006 Blacksburg, VA 24060
Principle Investigator/Lead:	Dr. Gary Pickrell Professor of Materials Science and Engineering pickrell@vt.edu (540) 231-3504
Principle Investigator	Dr. Anbo Wang
Report Preparer:	Dr. Daniel Homa Research Scientist dan24@vt.edu (410) 262-4775
Report Submission Date:	March 30, 2019

CPT
CENTER FOR PHOTONICS TECHNOLOGY

DISCLAMER

ACKNOWLEDGMENTS

This material is based upon work supported by the Department of Energy under Award Number DE-FE0012274.

EXECUTIVE SUMMARY

This is the final technical report for the Virginia Tech Center for Photonics Technology (VT-CPT) research project entitled "Reduced Mode Sapphire Optical Fiber and Sensing System". The objective of the five-year effort was to develop a low modal volume (LMV) single crystal sapphire fiber and demonstrate its advantages in current state-of-the-art sapphire-based temperature sensors and in novel distributed ultra-high temperature sensing systems.

The project, sponsored by the Crosscutting Research Program, began in 2014 and had the original goal of developing the next generation of harsh environment sensing systems. After successfully completing the original scope of the award, the project was expanded and extended to allow for the development of harsh environment packaging and testing of a prototype sensor system. These novel fiber optic sensing technologies provide real-time, accurate, and reliable temperature measurements at distributed locations in existing coal-fueled electricity generating units to improve the overall performance, reliability, and flexibility of the nation's coal-fired power plant fleet. In the final year (2018) of the project, prototype sensing systems were successfully deployed and operated in small commercial coal and natural gas fired boilers at the Virginia Tech Power Plant. The harsh environment quasi-distributed temperature sensing technology was advanced from a (Technology Readiness Level) TRL=1 to a TRL=7 by demonstrating the full validation of the sensing system prototype in a relevant industrial environment.

The real-time, accurate and reliable monitoring of temperatures at distributed locations is expected to lower operating costs by allowing more accurate measurement of the harsh conditions inside a boiler system to better control its operation. The technologies developed by Virginia Tech's Center for Photonics Technology will support the mission of the National Energy Technology Laboratory (NETL) to advance energy options to fuel our economy, strengthen our security, and improve the environment. Technical accomplishments during the program are summarized briefly here and described in detail in the remainder of the report.

- Fabrication of sub-micron single crystal sapphire fiber (for the first time)
- Observation of Raman Stokes and Anti-Stokes peaks in sapphire fiber (for the first time)
- Fabrication of FBGs in sapphire fiber via the point-by-point method (for the first time)
- Fabrication of FBGs in a few-mode sapphire fiber (for the first time)
- Measurement of fiber attenuation in the time domain in sapphire (for the first time)
- Distributed Raman temperature measurements in sapphire fiber (for the first time)
- Quasi-distributed FBG based temperature measurements in sapphire fiber
- Demonstration of few to single mode operation in sapphire fiber (for the first time)
- Theoretical analysis of novel micro-structured sapphire optical fibers
- Development of harsh environment packaging for fiber optic sensors
- Development of a user-friendly interface for sensor diagnostics and temperature monitoring that can be accessed remotely via a mobile device
- Successfully installed and operated a prototype distributed temperature sensing system in a commercial coal-fired boiler for over 1 month
- Successfully installed and operated a prototype distributed temperature sensing system in a commercial gas-fired boiler for over 2 months

TABLE OF CONTENTS

LIST OF FIGURES

LIST OF TABLES

1 INTRODUCTION

This is the final technical report for the Virginia Tech Center for Photonics Technology (VT-CPT) research project entitled "Reduced Mode Sapphire Optical Fiber and Sensing System". The objective of the five-year effort was to develop a low modal volume (LMV) single crystal sapphire fiber and demonstrate its advantages in current state-of-the-art sapphire-based temperature sensors and in novel distributed ultra-high temperature sensing systems. The first-of-its-kind technologies that were developed in this project will support current and future power generation technologies and boost efficiencies, with minimal to no environmental impact [1-11].

New sensor and control technologies will be essential to achieving the goal of developing "seamless, integrated, automated, optimized, intelligent" coal derived power plants [12, 13]. Specifically, real time monitoring of spatial and temporal distributions of temperatures in power plants will aid operators in removing pollutants, such as NO_x, at the source. Thus, plant efficiencies will improve, waste will be minimized, and operating costs will decrease. Traditional temperature monitoring techniques such as those that utilize optical pyrometers and precious metal thermocouples are limited by temperature and can be cost prohibitive and invasive if deployed in large numbers to obtain pseudo-distributed temperature measurements. Therefore, there has been significant interest in fiber optic sensing technologies to provide reliable and accurate fully distributed temperature measurements.

Mature fiber optic sensing technologies that utilize fused silica optical fibers have a proven track record of performance, but the extremely high temperatures and harsh environments have slowed implementation in power plants. Unfortunately, in the vast majority of power plant applications, fused silica is not able to withstand the chemically corrosive environments at temperatures in excess of 800°C. Subsequently, researchers have aggressively pursued single crystal sapphire as a "drop-in" replacement for fused silica to enable optical fiber sensing technologies such as Fabry-Perot (F-P) Interferometry and Fiber Bragg Gratings (FBGs) [14,15]. The high temperature stability and chemical corrosion resistance of sapphire fiber has made it the only choice in highly corrosive, high temperature sensing applications above 1000°C. Extremely high-quality sapphire fibers are available, but to date, the lack of a core-cladding waveguide structure and the highly multimode nature of these fibers has limited sensing capabilities and ultimate performance [16].

In this program, we developed a waveguide structure and the associated processing techniques for the fabrication of a low modal volume single crystal sapphire optical fiber. A fully distributed Raman backscatter temperature sensing system was demonstrated for the first time with single crystal sapphire fibers. A quasi-distributed temperature sensing system was developed with the use of FBGs fabricated in single crystal sapphire fibers via the point-by-point method. A novel fiber-in-ceramic tube (FICT) harsh environment sensor package was developed for successful deployment and operation of prototype sensing systems installed in a coal-fired boiler and gas-fired boiler in a commercial power plant at Virginia Tech. The harsh environment quasi-distributed temperature sensing technology was advanced from a (Technology Readiness Level) TRL=1 to a TRL=7 by demonstrating the full validation of the sensing system prototype in a relevant industrial environment.

2 TECHNICAL BACKGROUND

2.1 Harsh Environment Sensing and Monitoring for Coal Power Plants

A secure and efficient source of energy is critical to the stability of our nation, as well as the health and welfare of our citizens. In 2011, our nation's coal mines produced more than a billion short tons of coal, and more than 90% of this coal was used by U.S. power plants to generate approximately 42% of the country's nearly 4 trillion kilowatt-hours of electricity [12,13,17]. Clean coal technologies provide the potential for improved efficiency, reduced emissions, and dramatic improvements in the next generation of power plants. The Energy Policy Act of 2005 is a commitment to the research and development of novel clean technologies that will ultimately improve production efficiencies [18].

The importance of a continuous and reliable supply of energy to power the nation has recently come to the forefront of discussion/policy with persistent threats to the security and capacity of U.S. energy infrastructure. The use of coal mitigates some of these concerns because the facilities were designed to operate non-stop, providing a continuous supply of energy. Unfortunately, the shutting down of 420 coal operational units, with a combined capacity of more than 60 gigawatts (GW), puts the nation in an untenable situation. To approach full utilization of the remaining coal fired power plants, there is a need to improve operating efficiencies, minimize downtime, and adherence to regulatory environmental policies [13].

To meet the demands of the dynamic and fluid energy landscape, there is a push to propel utilities to next-level efficiencies and plant operation by leveraging technological advances such as advanced manufacturing, Industry 4.0 principles, and digitization and optimization strategies [12,13]. Sensor and control technologies provide the foundation that will enable operators to fully utilize these technological advances for reliable system integration, addressing cybersecurity concerns, and plant optimization [12,13].

Specifically, readily available temperature sensing technologies are often limited and do not provide the sufficient and timely information necessary to improve efficiencies, minimize downtime, and reduce toxic emissions. Techniques that utilize optical pyrometers and precious metal thermocouples are used primarily for detection and prevention of catastrophic events and are typically deployed as single-point measurements. Furthermore, these devices are limited by temperature and can be cost prohibitive and invasive if deployed in large numbers to obtain pseudo-distributed temperature measurements.

Mature fiber optic sensing technologies are attractive options for these applications, due in part because they are immune to electromagnetic interference (EMI) and offer distributed measurements over long spans with high accuracy and low noise. Nonetheless, the extremely high temperatures and harsh environments have slowed implementation in power plants. The most widely used optical fiber material, fused silica, is not able to withstand the chemically corrosive environments at temperatures in excess of 800°C. Subsequently, researchers have aggressively pursued single crystal sapphire as a “drop-in” replacement for fused silica to enable optical fiber sensing technologies such as Fabry-Perot (F-P) interferometry and FBGs [16]. The high temperature stability and chemical corrosion resistance of sapphire fiber has made it the only choice for the most demanding environments.

2.2 Single Crystal Sapphire Optical Fibers and Sensors

The high temperature stability and corrosion resistance of single crystal sapphire optical fibers that make them an attractive option for harsh environment applications also make them very difficult to process. To date, an adequate cladding material has yet to be identified for temperatures in excess of ~300°C. Sapphire fibers coated with polymer coatings have been successfully deployed in relatively benign environments, but these are limited to relatively low temperatures, on the order of a few hundred degrees Celsius [8]. Researchers have attempted to develop high temperature cladding materials based on magnesium/aluminum oxides, sol gel derived aluminum oxide materials with and without organic binders, precious metals, and novel composite structures [20-24]. Albeit, challenges related to dopant diffusion, contamination, thermal expansion mismatch, detrimental phase changes and reliability have limited acceptance in the industry. [16,20,21].

Single crystal sapphire fibers do not maintain a traditional optical fiber structure with a core and claddings, and are typically deployed with the surrounding environment (air) as the effective cladding, as shown in Figure 2. Although high quality sapphire fibers are available, the lack of a

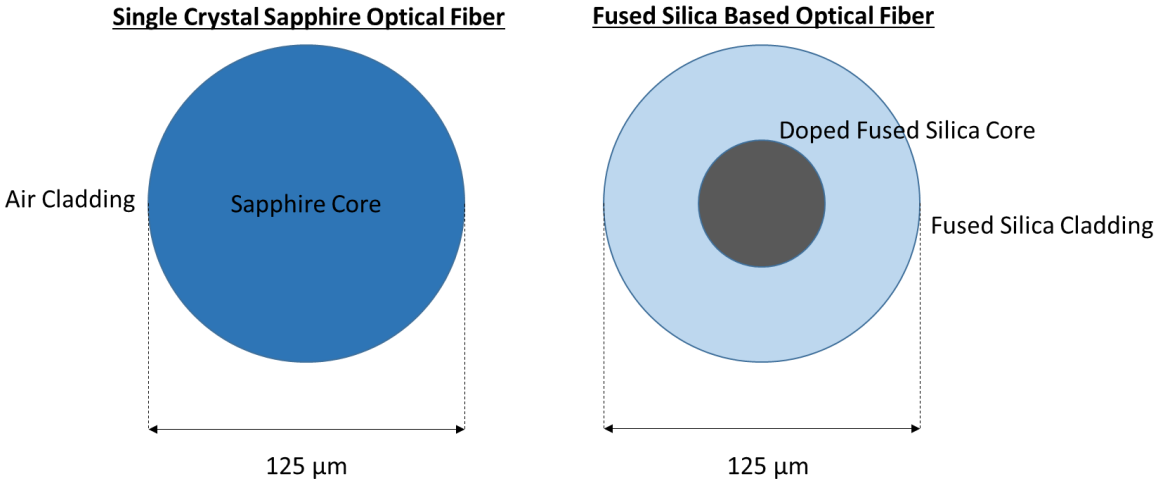

Figure 1. Structure of single crystal sapphire and fused silica based optical fibers.

cladding and very large refractive index difference between sapphire and air allows for the propagation of a very larger number of guided modes, which is detrimental to the performance of the sensing fiber and system.

Single crystal sapphire fibers deployed with air as the cladding maintain a very large numerical aperture (NA) due the large refractive index difference between the single crystal (SC) sapphire core and air cladding [19, 21]. The numerical aperture is defined as,

$$NA = \sqrt{n_{core}^2 - n_{cladding}^2} \quad , \tag{1}$$

where n_{core} is the refractive index of the core and $n_{cladding}$ is the refractive index of the cladding. At an incident wavelength of 532 nm, the refractive index of the core (SC sapphire) and cladding (air) are 1.772 and 1.0, respectively. Thus, the numerical aperture, calculated via Equation 1, of

the SC sapphire fiber is ~1.46, which is extremely large. As a comparison, the NA of traditional fused silica based multimode fiber is on the order of 0.20 – 0.275.

The number of guided modes can be determined by combining Maxwell's equations and boundary conditions, then solving for the Helmholtz equation. The V number, which is a normalized frequency parameter that determines the number of modes of a weakly guiding, step-index fiber, is defined as,

$$V = \pi \frac{d}{\lambda} NA \quad , \tag{2}$$

where d is the core diameter, λ is the incident wavelength, and NA is the numerical aperture. Thus, the V number is shown to increase with the core diameter and numerical aperture.

The number of guided modes, M, can be estimated for fibers with large V numbers via the following,

$$M = \left(\frac{4}{\pi^2} \right) V^2 \quad . \tag{3}$$

The number of modes guided in the fiber will increase dramatically with an increase in NA and/or core diameter. The estimated number of modes that will propagate in an unclad sapphire fiber with a diameter of 125 μm is on the order of approximately 189,000 at an operating wavelength of 532 nm. Although this a rough approximation because the single crystal sapphire fiber maintains a rounded hexagonal cross section as opposed to one that is perfectly circular in cross section and uniform in diameter as well as optically isotropic, the general trend and order of magnitude of the modal volume is accurate. The operating wavelength must also be taken into consideration for the design of the sensing system due to the inverse relationship between modal volume and wavelength.

In comparison, a commercial grade fused silica based multimode step-index fiber with a NA of 0.20, and core radius of 50 μm will support approximately 5,600 modes. Conversely, a single mode fiber with a NA of 0.12 and a core of ~10 μm only supports 1 mode. Typically, the NA and/or core size of fused silica-based optical fibers can be modified through selective doping of the core and/or cladding with different materials, but this cannot be easily done in single crystal sapphire fibers. Furthermore, any potential dopants in single crystal sapphire fiber deployed at extreme temperatures can readily diffuse into (or out of) the core.

The highly multimode nature of single crystal sapphire optical fibers yields unpredictable light transmission through the fiber and unreliable sensing performance. The extremely large number of modes that propagate in the fiber tend to limit the accuracy, resolution, and ultimate performance of the chosen sensing schemes. Nonetheless, due to the enormous potential of single crystal sapphire, multiple single-point temperature sensing technologies have been developed using this fiber despite the high modal volume greatly lowering the signal contrast obtained in all methods. The high modal volume in sapphire fiber has limited the possibility of fully distributed sensing in high temperature applications, where sapphire fiber is the only suitable choice. The wide acceptance of sapphire fiber sensing technologies requires a paradigm shift from waveguide structures with improved optical confinement and reduced modal volume.

2.3 Proposed Technology and Research Approach

The objective of the proposed research was to develop a low modal volume (LMV) single crystal sapphire fiber and demonstrate its advantages in current state-of-the-art sapphire-based temperature sensors and in novel distributed ultra-high temperature sensing systems. A relatively simple and cost-effective processing technique was demonstrated for the fabrication of a reduced diameter single crystal sapphire fiber with low modal volume. Comprehensive theoretical analysis of micro-structured waveguide designs demonstrated the modal reduction capabilities of a novel "wind-mill" single crystal sapphire optical fiber. In addition, the construction of laser heated pedestal growth (LHPG) system lays the foundation for the exploration of the mass-production of LMV single crystal sapphire optical fibers.

A Raman backscatter based distributed temperature sensing system was fully developed and demonstrated with operating temperature in excess of 1400°C (± 4°C) with a spatial resolution less than 20 cm. Furthermore, a point-by-point method for the fabrication of fiber Bragg gratings was successfully demonstrated for single crystal sapphire optical fiber for the first time. A quasi-distributed temperature sensing system based on these FBG sensors for operation with temperatures in excess of 1400°C. A prototype distributed temperature sensing system was fully ruggedized and integrated for the successful deployment and operation in coal-fired and gas-fired boilers in a commercial power plant at Virginia Tech. The multidisciplinary research effort, combining expertise in electrical and computer engineering with materials science engineering, was essential to the development of the reliable harsh environment fiber optic sensing systems that were motivated in this project to improve and protect the fleet of fossil fuel-based energy generation facilities in the nation.

3 LOW MODAL VOLUME SINGLE CRYSTAL SAPPHIRE FIBERS

3.1 Laser Heated Pedestal Growth of Single Crystal Sapphire Fibers

3.1.1 LHPG System Design

The most common methods employed to fabricate single crystal sapphire fibers are Laser Heated Pedestal Growth (LHPG) and Edge-defined Film-fed Growth (EFG). The LHPG technique was selected for this work because of its affinity for the synthesis of sapphire fibers, inherent flexibility, and its demonstration as a commercially viable manufacturing technique. All the fibers utilized for the creation of the low modal volume fibers were fabricated via LHPG and purchased from Micromaterials Inc. In addition, an LHPG system was designed and constructed for the in-house growth of single crystal sapphire fibers with unique geometries and properties to enhance sensor performance.

In the LHPG process, the tip of a sapphire source rod is melted with a focused CO_2 laser beam. A seed crystal precisely located and dipped into the melt and then drawn more rapidly than the source sapphire rod that is fed into the system. The growth and size of the resultant fiber can be controlled by the feed rate of the sapphire feed rod and the pull rate of the seed crystal (resultant fiber). The fiber diameter can be well controlled over long lengths (1-3 meters) with the integration of a diameter micrometer or vision system, a laser with is adequate stability, a

controlled growth environment and precision optics. The LHPG system is relatively inexpensive and preferable over other techniques for experimentation and fiber growth.

Generally, the basic elements of the system can be categorized into one of four major components: (1) mechanical system, (2) optical system, (3) control system and the (4) health, safety and environment (HSE) system.

1. *Mechanical System* – includes the growth chamber, optics table, translations stages, fiber and preform chucks, and several framework and precision mechanical components.
2. *Optical System* – includes the CO_2 laser, gold coated oxygen free copper flat and parabolic mirrors, polarizer, attenuator, modulator, HeNe guide laser, and beam splitting mirrors. The uniform heating necessary for this technique will require the use of one or more special optics such as a reflaxicon, beam profiler, and/or top-hat optics.
3. *Control System* - includes feedback loops from the diameter measurements, laser power meters, traverse rates of the linear stages to the laser, attenuation, stage motors, and other optical components.
4. *HSE System* – will be required for the use of the CO_2 laser. All the health and safety requirements must be met for the operation of the LHPG system. Components of the HSE system include the proper safety glasses to operate the laser, gas handling equipment and procedures, lock out – tag out components and procedures, signage, operating procedures, and an HSE safety plan.

Basic schematics of two slightly different LHPG system approaches are shown in Figures 2 and 3 [25, 26]. The major differences arise from the beam shaping technique and fiber drawing system. A reflaxicon optic is utilized to create a laser beam "ring" profile in the system .

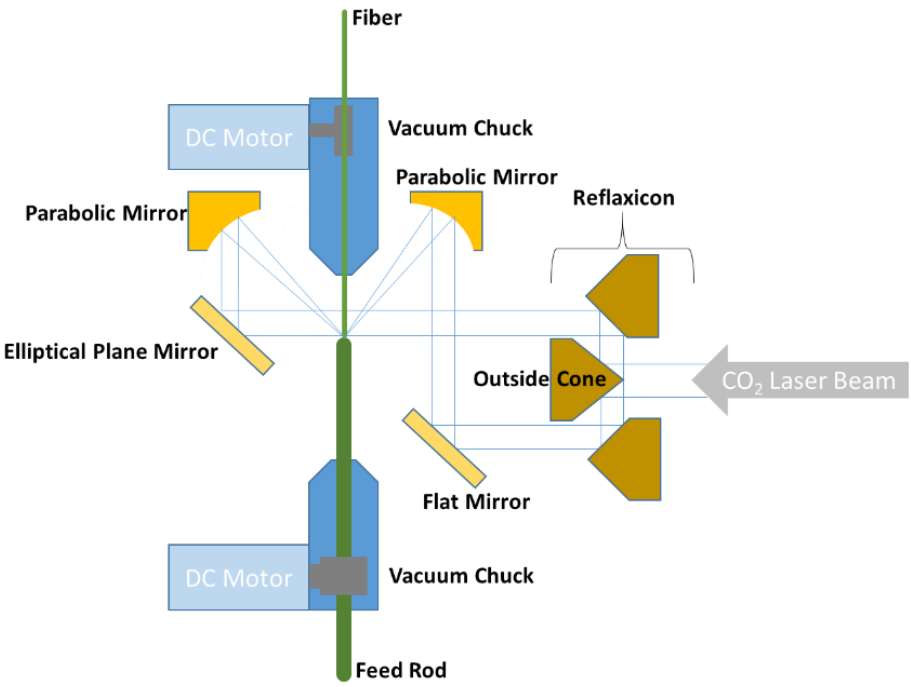

Figure 2. LHPG system design with reflaxicon optic (U.S. Patent 4,421,721) [25].

Conversely, the system shown in Figure 3 utilizes a graded reflectivity or Gaussian mirror to create a "super-Gaussian" or "top-hat-like" laser beam profile. Furthermore, the fiber drawing approach shown in Figure 2 uses a translation stage as opposed to the system of wheels shown in Figure 3. A specialized multi-dimensional tractor system was also explored as a third, possibly preferable option. Optimization and stability of the beam profile and fiber pulling system are necessary for the fabrication of high quality single crystal sapphire fibers.

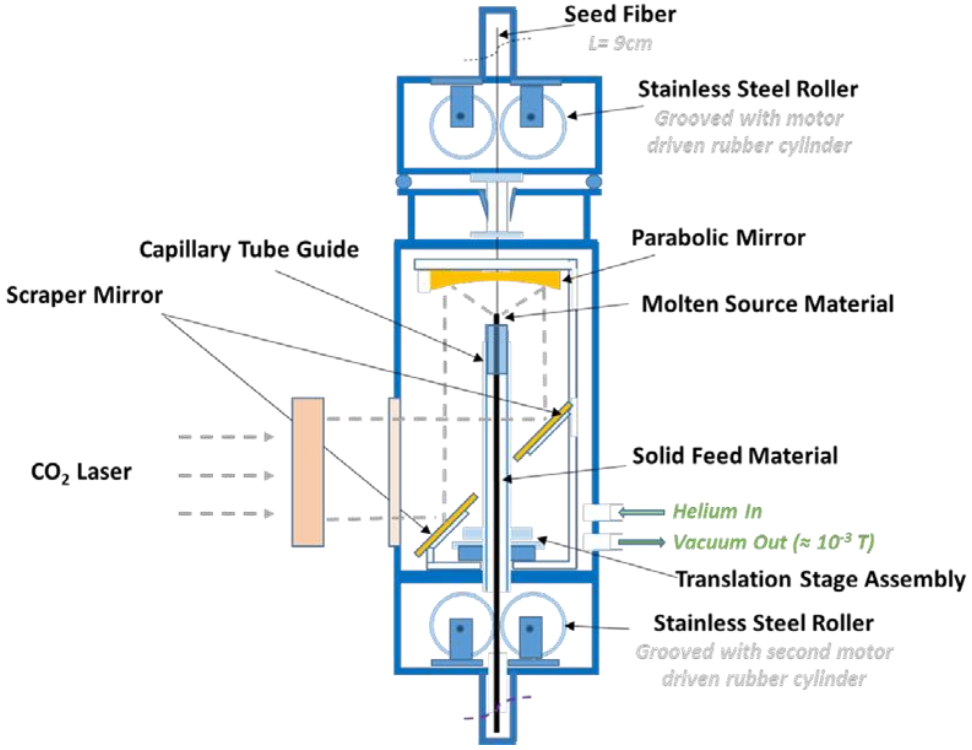

Figure 3. LHPG system design with graded reflectivity mirror optic (U.S. Patent 5,607,506) [26].

The first system design iteration of the LPHG system included an optical chamber with a reflaxicon optic, a beam shaping system for the CO_2 laser, and mechanical system with translation stages for the preform feed and fiber draw. The preliminary optical system in the chamber in LHPG system is shown in Figure 4. The CO_2 laser beam is first dispersed by the reflaxicon intoa ring shape. The scraper mirror reflects the light into vertical direction, and the customized parabolic mirror focuses all light to a point at the surface of the sapphire source rod. The top pin chuck pulls the sapphire fiber/seed upward. At the same time, the bottom pin chuck pulls the sapphire rod upward at a relatively slower speed (The screws and nuts are removed from the picture for clarity purposes). The out of chamber design with beam steering optics and control of the LHPG system is shown in Figure 5 for both 2D (a) and 3D (b) views. The optical table has a dimension of 36 in. by 48 in. The components, labeled numerically in the figures, are listed in Table 1.

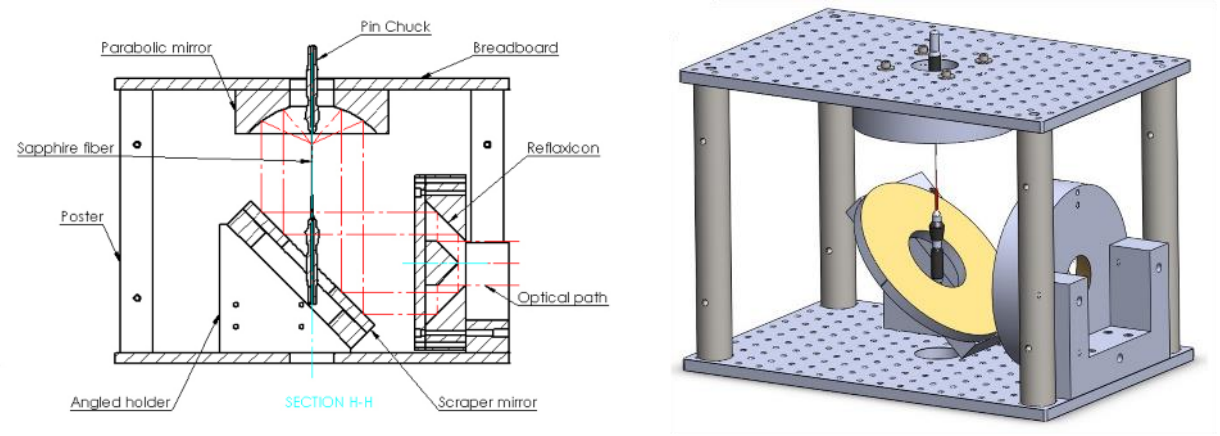

(a) (b)

Figure 4. (a) Mechanical drawings of optical chamber to include the reflaxicon and mirrors.

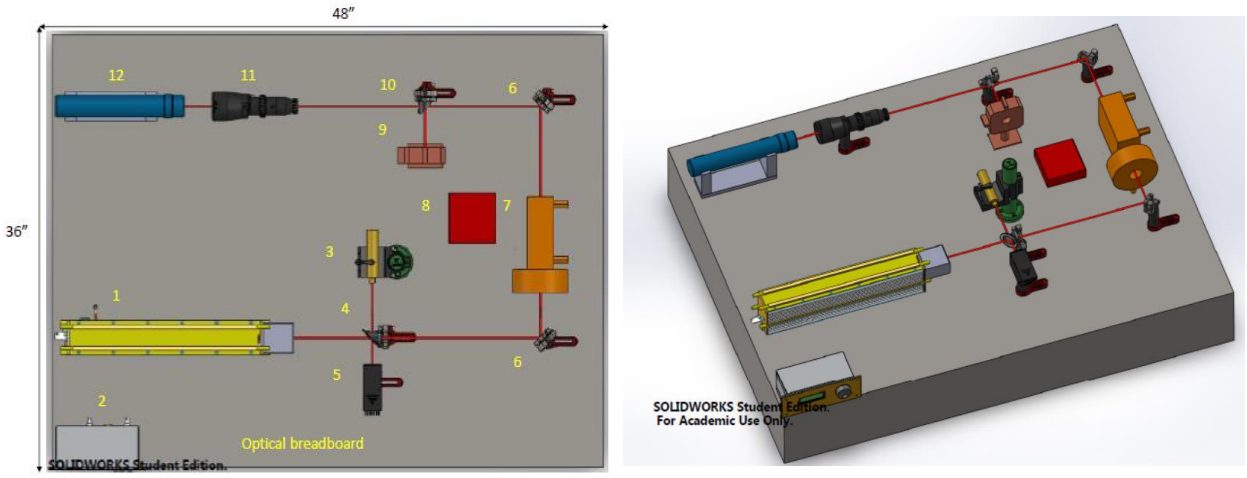

(a) (b)

Figure 5. (a, b) LHPG out of chamber, beam shaping design on optical table.

Table 1. "Outside the Chamber" Components

Label	Component	Vendor
1	CO2 Laser	Coherent
2	Controller Kit	Coherent
3	HeNe Laser	Thorlabs
4	Beam Combiner	II-VI Infrared
5	Beam Trap	Thorlabs
6	CO2 laser mirror	Thorlabs
7	Attenuator	Edmund Optics
8	Power meter	Edmund Optics
9	Sensor	Edmund Optics
10	Beam Splitter	II-VI Infrared
11	Beam Expander	Edmund Optics
12	Top Hat Optics	Edmund Optics

3.1.2 LHPG System Construction and Operation

The LHPG system was constructed with all the major components and the integration of the necessary features to assure the safe and efficient operation the system. Generally, the LHPG system consists of a laser generation system, an optical layout for beam focus and guidance, a growth chamber, mechanical pulling stages, and observation devices, as shown in Figure 6. The optical layout of the LHPG system is also shown in Figure 7. The optical components were secured to a Newport optical table that possesses pneumatic vibration dampers on all four corners. Optical power was produced by a Coherent Model GEM 100-L CW CO_2 laser which is designed to give a very stable, high output power (100 W, +/- 3%) at wavelength of 10.6 um. The laser beam is steered into the growth chamber using several 45º coated mirrors and

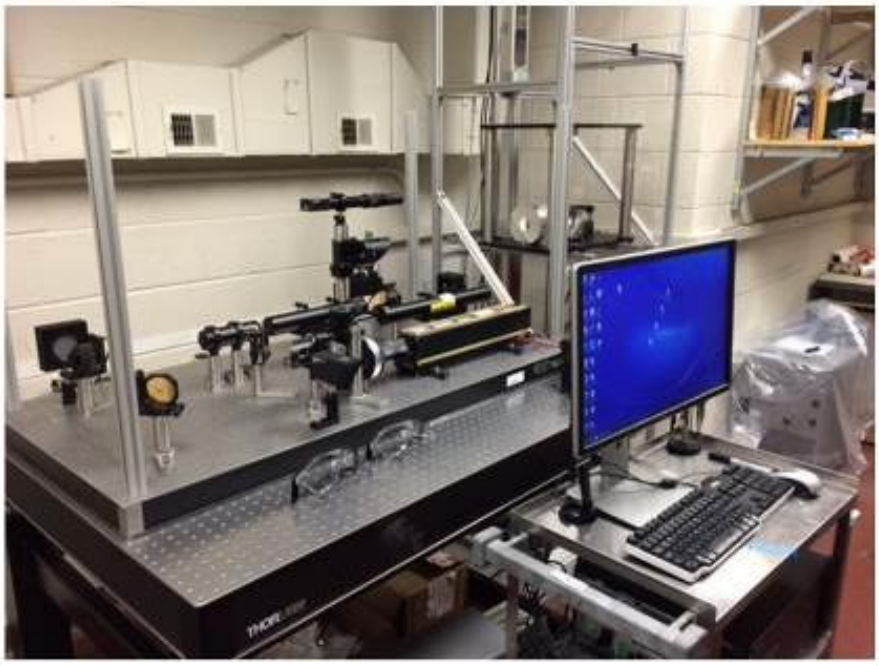

Figure 6. Overview of the LHPG system

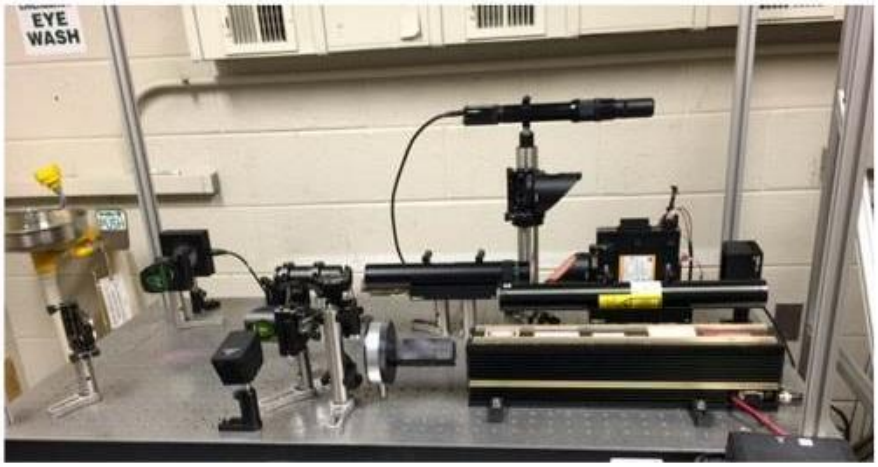

Figure 7. The optical layout of the LHPG system projects, attenuates, and guides the laser beam to the growth chamber.

combined with a 632.8nm HeNe laser beam to enable the easy and safe tracing of the CO_2 laser path. A polarizer-analyzer-attenuator (II-VI, Inc. Model: PAZ-20-AC-6) sits on the optical route to provide accurate step attenuation of the output laser power and further improve the power stability of the laser beam prior to entering the growth chamber. A beam expander and flat-top beam shaper (Edmund, Model: 62471 and 84360) was also included in the beam path to enable beam expansion and the conversion of the Gaussian-shaped beam into a collimated flat-top beam.

The growth chamber of the LHPG system is shown Figure 8. After passing through the beam expander and flat-top beam shaper on the optical table, the beam encounters the apex of the inner mirror cone of the reflaxicon. The reflaxicon consists of a primary conical mirror surrounded by

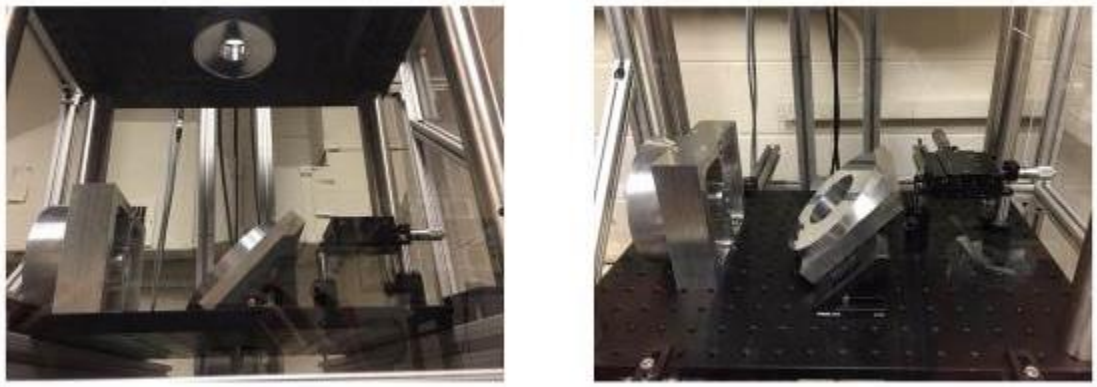

(a) **(b)**

Figure 8. The layout of the growth chamber accommodates the presence and movement of the feedstock and fabricated sapphire fiber while focusing the laser light into a central hot zone.

a larger conical mirror. Both conical mirrors are coaxially located with respect to each other and have an identical conical angle of 45º. The reflaxicon converts the solid circular beam into an annulus ring with minimum radiation loss. As the beam leaves the reflaxion, it is reflected off a doughnut-shaped mirror (called the "scraper mirror") located 45º to the beam propagation direction, with the center hole accommodating the vertical translation of the upper pulling arm. The scraper mirror directs the radiation annulus onto a parabolic mirror, which then focuses the beam back to the focal point at the alumina rod feedstock, thereby forming the hot zone.

The mechanical system is shown in Figure 9. The translation of the feed and the seed rod are controlled by two high precision linear stages manufactured by Parker-Hannefin (Figure 9(a)). These precision ball screw linear stages are controlled by high-resolution servo drives and an automation controller, which may be programmed to exhibit the required movement. A side view of the LHPG system is shown in Figure 9(b); the growth process will be observed from the front side of the growth chamber. A long-distance microscope (Edmund) located on the optical table transfers an image of the nascent sapphire fiber to a point grey CCD video camera (Model GS3-U3-50S5M-C) which may then be viewed, saved, and enhanced on the attached computer. Furthermore, the in-situ images of the hot zone were processed to determine the dimensions of the growth region, which will then be utilized in a control loop for the diameter control system.

(a) **(b)**

Figure 9. (a) The mechanical linear stages of the LHPG system enable precise addition of alumina feedstock and growth of sapphire optical fiber. (b) Side view of the LHPG system.

Closed-loop-control software was written for an automatic diameter control system, as shown by the basic flow chart in Figure 10. A Labview program was written to continuously process the image of the melt zone to obtain a diameter measurement that is then used to modulate the CO_2

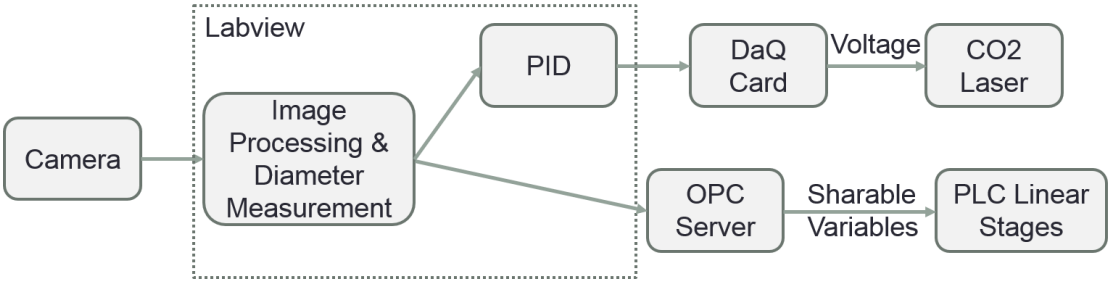

Figure 10. Flowchart for the automatic diameter control for the LHPG system.

laser power and the traverse rates of the linear stages, as shown in Figure 11. Single crystal sapphire fiber with a diameter of 115 microns was drawn over a length 22 cm with a diameter variation less than 2%. For example, sapphire fiber growth was performed at a fixed pulling rate at 50 μm/s in air by using around 20 W of applied laser power for the chosen feed and seed rods. Several sapphire fibers with lengths of approximately 20 cm were routinely fabricated on the LHPG system. The drawn fibers were optically clear to the naked eye and under optical microscope examination. One such fiber with diameter of ~115 μm is shown, macroscopically, in Figure 12(a) and upon magnification via an optical microscope in Figure 12(b). Diameter variations on the order of 1.7% were readily achieved, which is comparable to those commonly reported in the literature.

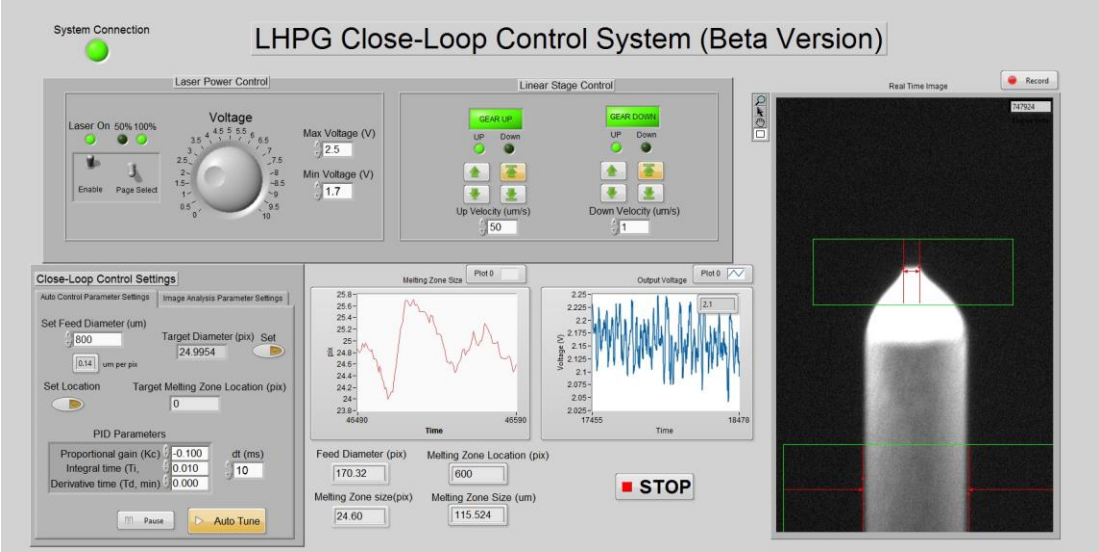

Figure 11. "Screen shot" of the LHPG closed loop control system.

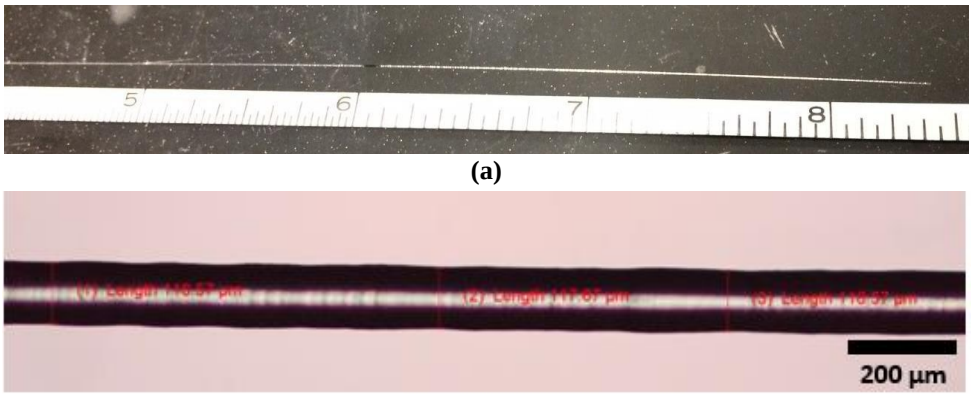

(a)

(b)

Figure 12. (a) As- grown ~240µm diameter sapphire fiber. (b) As grown sapphire fiber with diameter of 115 µm under optical microscope.

3.1.3 LHPG System Improvements

The LHPG system at Virginia Tech was successfully designed, constructed, and commissioned for the growth of single crystal sapphire fibers. The desire to fabricate higher quality and unique sapphire optical fibers has provided the impetus for optimization of the system components. A novel beam shaping system was proposed to improve system performance and reduce system complexities.

The components for the improved beam shaping optical system design as shown in Figure 13. Two ZnSe axicons are used to transform the beam into a ring and the two additional mirrors route the beam to an "off-axis" parabolic mirror with a central hole to the translation of the drawn fiber. The double axicon is more cost effective than a reflaxicon, which is the most commonly used optical device in LHPG systems. Furthermore, this new approach is simple, compact, enables easier optical alignment and allows for the use of a smaller growth chamber. It is anticipated that the proposed system modifications will further simplify the operation of the LHPG system and produce higher quality single crystal sapphire fibers.

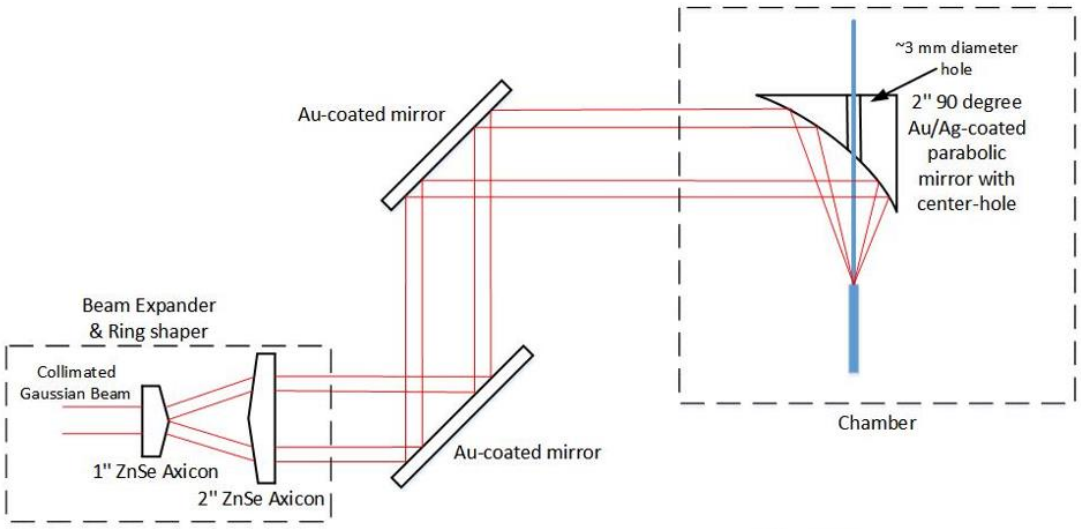

Figure 13. Improved beam shaping optics for the LHPG system.

3.2 Reduced Diameter Single Crystal Sapphire Fibers

The modal volume in single crystal sapphire optical fibers can be minimized by reducing the diameter of the waveguide. The efficient reduction in modal volume was successfully demonstrated for single crystal sapphire optical fibers etched via a hot-wet acid etching technique. The equipment and processes were developed to effectively tune the single crystal sapphire fiber diameter and characterization of the modal volume, demonstrating the efficacy of the approach. The ability to tune the waveguide properties of single crystal sapphire optical fibers via simple and cost-effective post processing techniques creates a paradigm shift in ultra-high temperature fiber optic sensing.

3.2.1 Hot-Wet Acid Etching Technique

The basic etching reactions for the phosphoric acid portion (Eq. 4 and Eq. 5) and sulfuric acid portion (Eq. 6 and Eq. 7) have been documented in the literature as [27-31]:

$$Al_2O_3 + 6H_3PO_4 \rightarrow 2Al(H_2PO_4)_3 + 3H_2O \quad (4)$$

$$Al(H_2PO_4)_3 + Al_2O_3 \rightarrow 3AlPO_4 + 3H_2O \quad (5)$$

$$Al^{3+} + nSO_4^{2-} \rightarrow Al_2(SO_4)_n^{3-2n} \quad (6)$$

$$2Al^{3+} + 3SO_4^{2-} + xH_2O \rightarrow Al_2(SO_4)_3 \cdot xH_2O \quad . \quad (7)$$

The Al_2O_3 dissolves into the acids as solvated Al^{+3} ions and the acids dissociated into a number of their respective ionic species [32]. The reactants are transported to the fiber surface, react, and the products in solution are transported away from the interface. A more thorough description of the reactions can be found in selected publications [30-33].

At temperatures above 300°C, both sulfuric and phosphoric acids exhibit chemical changes. First, both acids will dehydrate to diacid form:

$$2H_3PO_4 \rightarrow H_4P_2O_7 + H_2O \quad , \quad (8)$$

$$2H_2SO_4 \rightarrow H_2S_2O_7 + H_2O \quad . \quad (9)$$

Further dehydration of pyrophosphoric acid (the diacid form) can result in the formation of a few different varieties of polyphosphoric or metaphosphoric acid, the basic form being:

$$HO(PO_2OH)_xH \quad , \quad (10)$$

where *x* is the number of phosphoric units in the molecule.

Continued dehydration will finally yield anhydrous phosphorus pentoxide, the transformation directly from the diacid occurring as [23]:

$$H_4P_2O_7 \rightarrow P_2O_5 + 2H_2O \quad . \quad (11)$$

Process temperatures up of 343°C were selected to achieve rapid etching of the sapphire while also avoiding the formation of aluminum sulfates on the surface of the fiber. At temperatures above approximately 350-400°C, insoluble $Al_2(SO_4)_3$ and $Al_2(SO_4)_3 \cdot 17H_2O$ products were deposited on the sapphire fiber surface and inhibited further etching of the sapphire [30].

3.2.2 Fabrication of LMV Single Crystal Sapphire Optical Fiber

Relatively simple and effective processing techniques were developed to tailor the geometry and size of single crystal sapphire fibers. Single crystal sapphire fibers were etched in a solution of sulfuric and phosphoric acid at elevated temperatures to create optical fibers with diameters as small as 800 nm, as shown in Figure 14.

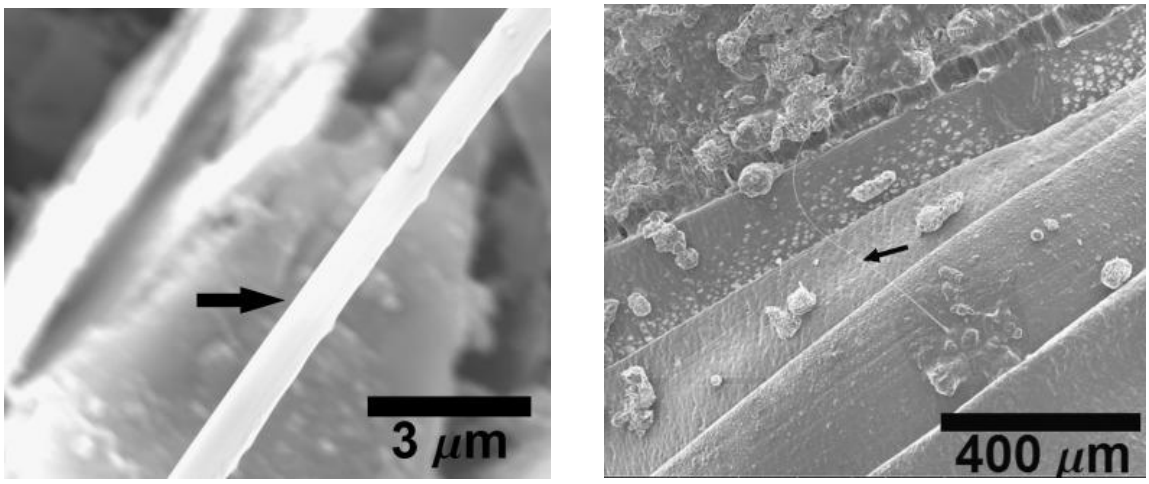

(a) **(b)**

Figure 14. (a) Submicron single crystal sapphire optical fiber. A sapphire fiber with a 50 μm diameter was immersed in a solution of sulfuric/phosphoric acid solution at a temperature of 343 °C for approximately 21 h. (b) An extended SEM image of the submicron single crystal sapphire fiber with a length of approximately 1 mm. The sapphire fiber is indicated by the black arrow.

Bare single crystal sapphire optical fibers with diameters of 50 µm to 125 µm, acquired from Micromaterials, Inc., were etched to the desired the desired diameters. All fibers were fabricated via the laser-heated pedestal growth (LHPG) method. The chemicals used for the acid etching solutions, 99.8% H_2SO_4 and 85% H_3PO_4, were acquired from Sigma Aldrich.

Custom acid etching stations, such as the one shown in Figure 15, were constructed for etching of the single crystal sapphire fibers. For this system, a custom hotplate was fabricated with G-28 refractory brick (Sheffield Pottery), 20-gauge 80% Nickel-20% Chromium resistive heating wire (Omega), and a 20A Variable Transformer. The solution temperature was continuously monitored using a Digi-Sense 20250-01 Type-K thermocouple thermometer (Davis Instruments). The acid etching solution was contained in a covered glass beaker (Kimax).

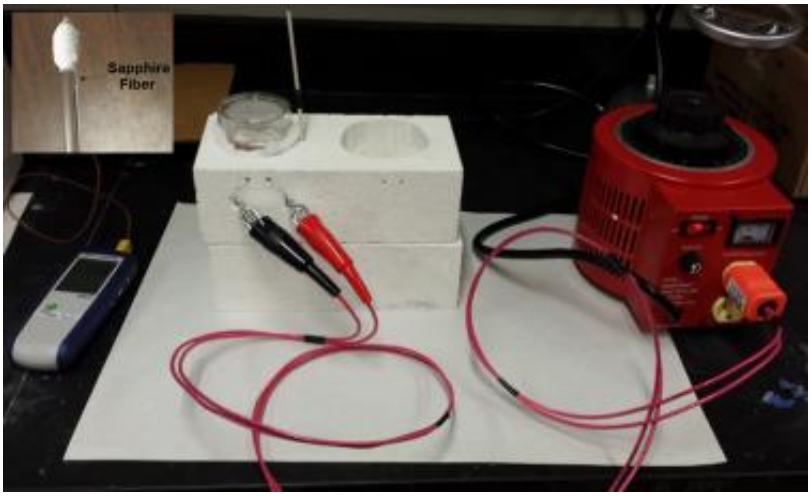

Figure 15. The wet acid etching system includes a glass beaker heated with a custom hotplate consisting of refractory brick, resistive heating wire and a variable transformer. The temperature was monitored with a glass-shielded thermocouple. The inset shows a fiber attached to a ~5 mm diameter glass rod with Teflon tape prior to immersion in the etching solution. The sapphire fiber is indicated by the black arrow.

Prior to etching, fibers were attached to a ~5 mm diameter glass rod using Teflon tape, as shown by insert in Figure 15. This configuration assured that the position of the fiber was consistent throughout the etching process. The etching solution was maintained at a temperature of approximately 343°C with a 15% standard voltage setting on the variable transformer. The solution was not stirred. In addition, the fibers were periodically removed from the etching solution to measure the diameter. The samples were removed from the boiling acid solution at-temperature to avoid the deposition of etch products upon cooling of the solution. An Olympus BX51 optical microscope with Stream Motion image analysis software was utilized to measure the fiber diameters. Furthermore, Extended Focal Imaging (EFI) was used to maintain focus at varied working distances within the same image. The final fiber diameter was imaged using a FEI Quanta 600 FEG scanning electron microscope.

In the first set of experiments, the single crystal sapphire fibers were immersed in a 3:1 sulfuric to phosphoric acid solution to determine the etch rate. As shown in Figure 16, the diameter of the fiber was reduced at a rate of 2.3 µm/hr. Furthermore, as seen in the inset, the material

removal rate increased as the exposed surface area decreased with etch time. After a total of 20.5 hours of etching at temperature, the final fiber diameter was approximately 800 nm.

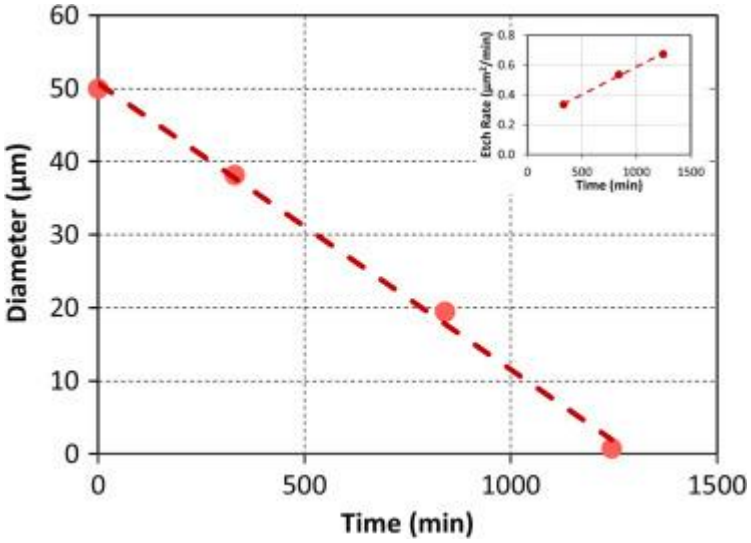

Figure 16. The change in diameter of the sapphire fiber exposed to the acid etching solution, as a function of time. The inset shows the increase in etch rate as a function of time due to the gradual reduction in surface area.

The influence of the solution chemistry on the etching process was further evaluated by determining the activation of energy for the sulfuric acid, phosphoric acid, and 3:1 molar ratio solutions. The activation energy of the etching reaction was determined by the rate of reaction as a function of temperature, per an Arrhenius relationship, as shown by the following,

$$k = Ae^{\frac{-E_a}{RT}} \quad , \tag{12}$$

where A is a constant related to the fit of the experimental data, k is the rate constant (the experimentally measured value for the extent of the reaction, which in this case is the rate of etching), R is the gas constant, and T is the temperature in Kelvin. In a reaction with linear dependence on temperature (as was observed in this study), rearranging the Arrhenius equation by taking its natural logarithm allows for simple extraction of the value for the activation energy. The natural logarithm of the Arrhenius equation becomes

$$\ln(k) = -\frac{E_a}{R}\left[\frac{1}{T}\right] + \ln(z) \quad , \tag{13}$$

and the activation energy was found by plotting ln(k) versus 1/T. The activation energy is essentially equivalent to the slope of the linear fit multiplied by the gas constant.

The single crystal sapphire fiber samples were held in the etching solution for 3 hours. The etching time was reduced to 1 hour for samples immersed in sulfuric acid at 330°C and 337°C to prevent complete evaporation. The experiments were repeated at least three times at a given temperature with a fresh solution and a new fiber, and the fiber diameters were measured at several points along the exposed region of the fiber.

Samples etched with the detailed procedures and custom equipment maintained a surface of very high quality, as shown in Figure 17(a), but an excessive heating rate will induce the formation of insoluble etch products that deposited on the surface of the fiber, as shown in Figure 17(b).

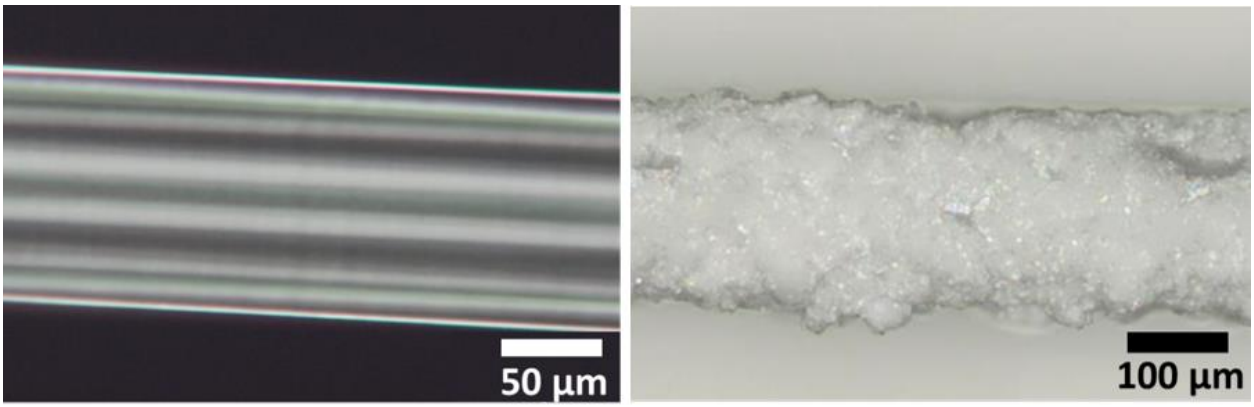

(a) **(b)**

Figure 17. (a) Sapphire fiber with a high-quality surface etched under optimum etching conditions. (b) Aluminum sulfate deposits on the surface of sapphire fiber etched under non-optimum etching conditions.

Often observed with the use of a 3:1 acid mixture, the aluminum sulfate ($Al_2(SO_4)_3 \cdot xH_2O$) deposits form an intermittent mask on the surface that inhibits the etching process. As shown in Figure 18(a,b) the aluminum sulfate deposits as distinctive rectangular crystals that are monoclinic in crystal structure. Subsequently, deposits that remain on the surface will act as scattering centers and degrade the transmissive properties of the waveguide. Furthermore, the surface inhomogeneities that remain upon removal of these etch deposits, via mechanical or chemical means, will also degrade the optical quality of the fiber. The formation of aluminum sulfates must be avoided to assure the optical quality of the single crystal sapphire fibers.

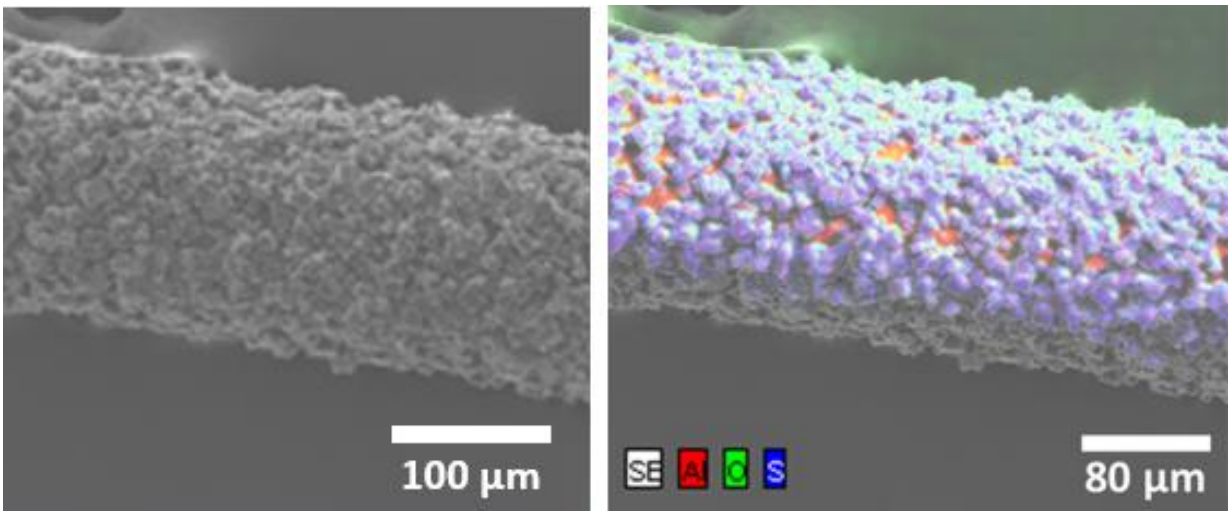

(a) **(b)**

Figure 18. (a) SEM image and (b) compositional analysis of the aluminum sulfate deposits on the surface of an etched sapphire fiber.

The measured etch rates for single crystal sapphire fiber were shown to have a noticeable dependency on the solution chemistry, as shown in Figure 19(a). At temperatures up to ~350°C, the 3:1 H_2SO_4:H_3PO_4 (molar) mixture induced a greater etch rate than either the aqueous

orthophosphoric acid or sulfuric acid solution alone. Generally, the etch rates exhibit a strong linear dependence on temperature irrespective of the solution composition. The etch rates in the orthophosphoric acid begin to deviate from this linear trend at temperatures greater than 350°C due to the transient nature of the solution chemistry throughout the dehydration of the orthophosphoric acid. An opaque white slurry was observed with a change in the compositional ratio of the di/poly/metaphosphoric acid with phosphorus pentoxide. The larger etching rate was attributed to the increasing amount of phosphorus pentoxide in the solution as compared to di/poly/metaphosphoric acid.

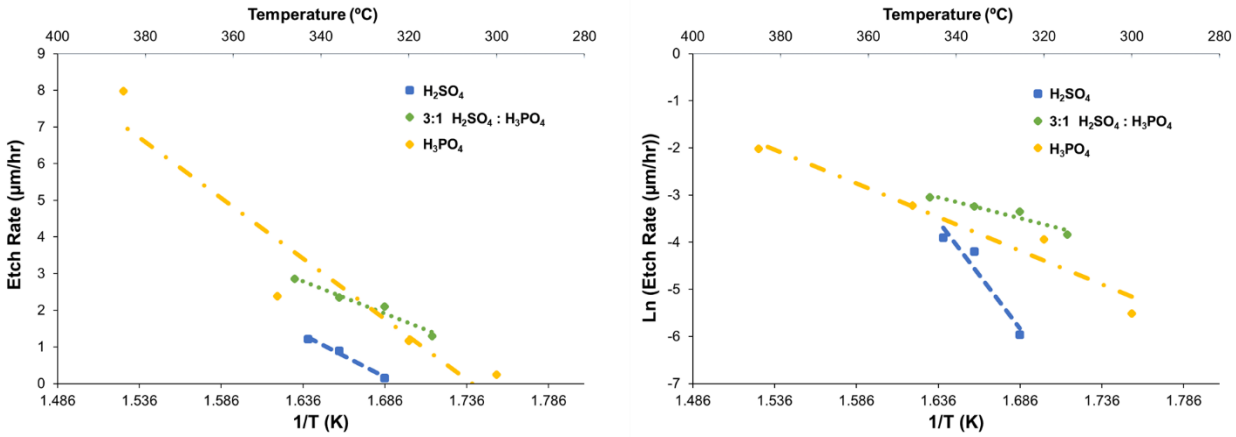

(a) **(b)**

Figure 19. (a) The measured etch rates of single crystal sapphire fibers in sulfuric acid (H_2SO_4), phosphoric acid (H_3SO_4), and 3:1 molar ratio mixture of the two. (b) The natural logarithm of the measured etch rate plotted versus the inverse of temperature; the activation energy is derived from the slope of the curves.

The activation energy for the chemical etching processes was determined by plotting the natural log of the etch rate as a function of temperature, as shown in Figure 19(b). As shown in Table 2, the activation energies derived from this study are comparable to those previously reported for the a-plane and m-plane in the 3:1 molar ratio solution; conversely, the value was lower than

Table 2. Activation Energies for Wet-Acid Etching of Single Crystal Sapphire Fiber

Etch Solution Composition	Activation Energy (kcal/mol)			
	This Study	c-plane [35]	a-plane [36]	m-plane [36]
98 wt% H_2SO_4	90.1	36.5		
85 wt% H_3PO_4	31.5	20	~18.3*	~18.6*
3:1 (molar) H_2SO_4:H_3PO_4	17.8	30.6		

*Average value reported by [21]. Solution composition was found to have an insignificant influence on etch rate.

those reported for the c-plane. The activation energy of orthophosphoric and sulfuric acid reactions with the sapphire fiber surface was ~1.8 and ~5.0 times that of the 3:1 molar solution, respectively, and ~1.6 and ~2.5 times that reported for the c-plane, respectively.

The crystallographic orientations of the single crystal sapphire fiber perpendicular to the c-axis complicate the analysis of the etching process. The chemical reactions that are observed occur at the surface of the fiber on which the a-plane and m-plane are exposed to the acid solution. Although the activation energies for the a-plane and m-plane are similar, the difference in the etch rates produce clear facets on the fiber end-face, as shown in Figure 20. The angled tip of the fiber end face caused by this faceting has been shown to act as a scattering center and must be accounted for in sensor applications.

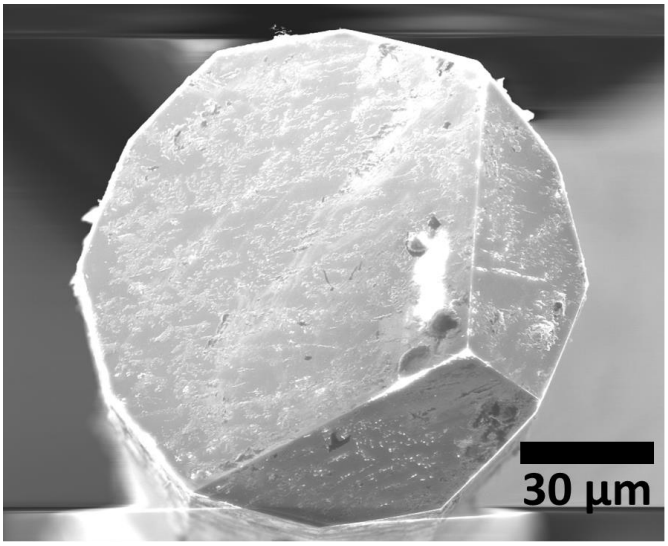

Figure 20. SEM image of the etched fiber end face with facets.

The activation energy that was observed for the 98 wt% H_2SO_4 aqueous solution was found to be greater than both the 85 wt% H_3PO_4 aqueous solution and the 3:1 H_2SO_4:H_3PO_4 mixture, which is consistent with those reported for the c-plane. The higher reactivity of the phosphates with aluminum is reflected in a lower activation energy. The activation energy associated with the 3:1 H_2SO_4:H_3PO_4 mixture was found to be lower than both the sulfuric and phosphoric acid.

The etch rates of the SCSF observed with the 3:1 H_2SO_4:H_3PO_4 mixture was comparable to those reported in the literature for the a-plane and m-plane. On the order of 2 µm/hour at 350°C, the etch rate is more than 4.5 times slower than that of reported for the c-plane (~9.3 µm/hour). The etch rate for the SCSF (~1.6 µm/hr) observed in sulfuric acid at this temperature were comparable to those reported for the c-plane (~1.4 µm/hr). Conversely, the etch rates for the SCSF (~4 µm/hr) at this temperature observed in orthophosphoric acid was significantly greater than those reported for the c-plane (< 1 µm/hr). The variation in etch rates along different crystallographic orientations arises from the complex chemistry of the acidic solutions at elevated temperatures and the interactions with single crystal sapphire.

Sapphire's c-plane orientation is the most atomically dense of all sapphire orientations and is formed of interchanging O-Al-Al-O-Al-O layers that present no crystallographic weaknesses (such as strained or stretched atomic bond lengths) [35]. The high etching rate for the c-plane in the aqueous sulfuric acid solution and the 3:1 H_2SO_4:H_3PO_4 mixture can be attributed to the sorption and catalysis processes that proceed with more intensity on the most packed planes. Its

perpendicular planes (including the a-plane and m-plane) however, contain interchanging O-O-Al-O-Al-O-**O—O**-Al-O-Al-O layers, and the bonds between the extended **O—O** layers are weakened at this strained bond length [35]. The phosphoric acid has been shown to target crystallographic defect sites at a much greater rate than sulfuric acid, which would explain the higher etching rate for the a-plane and m-plane as compared to the c-plane. Furthermore, phosphoric acid will dehydrate at temperatures greater than 300°C to form di/poly/metaphosphoric acid and then phosphorous pentoxide, which has been shown to significantly increase etch ratings. Unfortunately, a significant occurrence of pitting and other surface defects was observed when using pure phosphoric acid as an etchant for SCSF at elevated temperatures (>300°C), as shown in Figure 21.

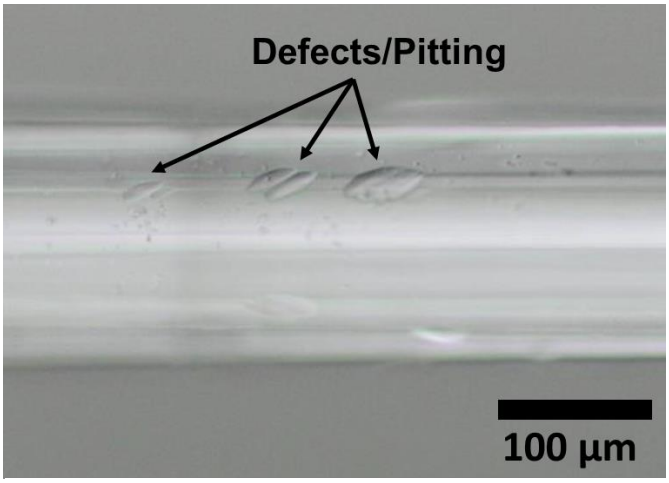

Figure 21. Optical micrograph of pitting and defects on the surface of a SCSF etched in an 85 wt% aqueous solution at 365°C.

The lower etch rates observed for the a-plane and m-plane of the SCSF in the 3:1 H_2SO_4:H_3PO_4 mixture can be attributed to diphosphoric acid's dehydration to polyphosphoric acid and its interaction with the sulfuric acid at temperatures above 300°C. The presence of sulfuric acid in the 3:1 H_2SO_4:H_3PO_4 mixture will molecularly interfere with the polymerization of diphosphoric acid and/or simply contribute more water to the system (as it is also dehydrating to diacid form). The H_2SO_4 has been observed to prevent degradation process of the H_3PO_4 to polyphosphoric acid ($H_4P_2O_7$), polyphosphoric or metaphosphoric acid ($HO(PO_2OH)_xH$), and phosphorus pentoxide (P_2O_5). Therefore, the inhibition of the depolymerization of pure phosphoric acid to phosphorous pentoxide, and to a less extent poly/meta phosphoric acid, limited its contribution to the etching process for the 3:1 H_2SO_4:H_3PO_4 mixture. This phenomenon becomes more pronounced with etching of the a-plane and m-plane of the SCSF as compared to the c-plane because of its slower rate of etching by pure phosphoric acid compared with that of sulfuric acid. Therefore, any additional contribution made by a decreased presence of phosphorus pentoxide and poly/meta phosphoric acid during etching would not have nearly the effect on c-plane surfaces as compared to the m-plane and a-plane surfaces.

Chemical etching via sulfuric/phosphoric acid at elevated temperatures (>300°C) has been shown to be very effective means to modifying the geometry of single crystal sapphire optical

fibers. Significant care must be taken to achieve reasonable etch rates (> 1μm/hr) and the high surface quality required for optical fiber and sensor applications. The solution chemistry, etching temperature, and the subsequent rate of material removal must be optimized to avoid defects such as surface pits and insoluble sulfate deposits.

3.2.3 Performance of LMV Single Crystal Sapphire Optical Fiber

3.2.3.1Numerical Aperture Measurements

The numerical aperture (NA) an optical fiber determines the range of angles at which the fiber can accept or emit light. The NA also helps dictate the number of optical modes that are guided in a silica or sapphire fiber. In distributed temperature sensing systems, a smaller NA can reduce pulse broadening and improve the achievable spatial resolution. Therefore, an accurate and reliable measurement of the NA of the sapphire fiber is paramount. Generally, the NA is defined as the sine of half the angle of a fiber's light acceptance cone, as shown schematically in Figure 22 [37]. All modes of light entering the fiber at angles less than that which correspond to the NA

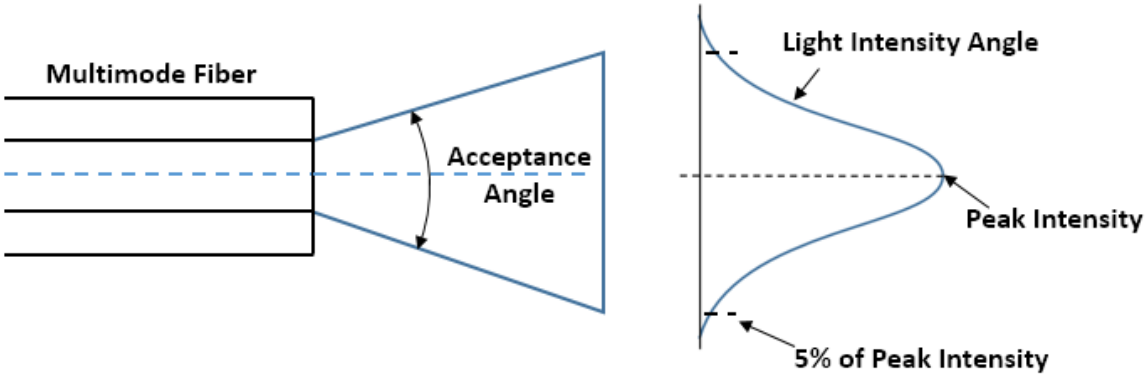

Figure 22. Intensity of light emerging from a multimode fiber falls to about 5% of the peak value at the edge of its acceptance angle [37].

will be bound or confined to the core of the fiber. Therefore, the larger the NA of a fiber, the larger the light acceptance cone. The numerical aperture can be determined from the measurements of the far-field optical power distribution exiting from a one or two meter length of fiber. The light emerging from a multimode fiber spreads over an angle equal to its acceptance angle, and the NA can be calculated from this acceptance angle. For practical measurements, the edge of the beam is defined as the angle where intensity drops to 5% of the peak intensity.

A schematic of the NA measurement and corresponding calculations is shown in Figure 23. In this measurement, the beam profiler was fixed on the optical table and fiber was fixed on a linear stage, which was translated to different positions such as those labeled "A" and "B". The variables shown are defined as the following: "dA and "dB" are the beam diameter of studied fiber at position A and B, "ΔL" is the distance change on the linear stage (ΔL=1/16 inches in this study), "Δd" is the beam diameter different between position A and position B, and "θ" is half of the acceptance angle. The numerical aperture, *NA*, is defined as [38],

$$NA = \sin\theta = \sin\left(\tan^{-1}\frac{\Delta d}{\Delta L}\right). \tag{14}$$

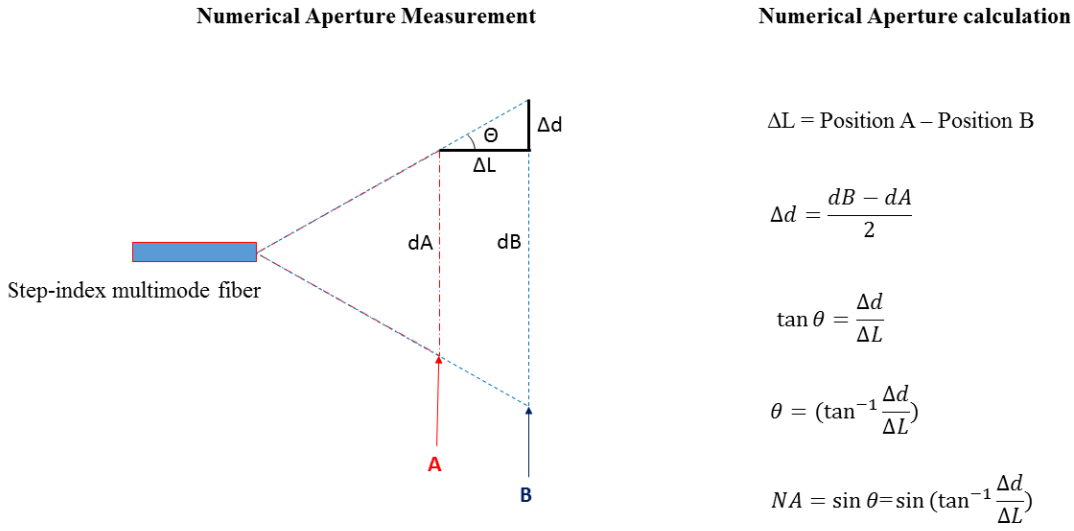

Figure 23. Numerical aperture measurement and calculations [38].

The determination of the NA of the sapphire fibers is essential to understand the waveguide and transmission properties, and ultimately the performance of the chosen sensing approach. In addition, the influence of the waveguide structure (such as the "windmill" and reduced diameter designs) on the NA must be fully understood to optimize the fiber and sensor design.

Three different methods can be employed to characterize the distribution profile of the light exiting the fiber, as shown schematically in Figure 24. In the beam profile method, an optical detector was used to measure the 2D distribution of the light output via two single measurements

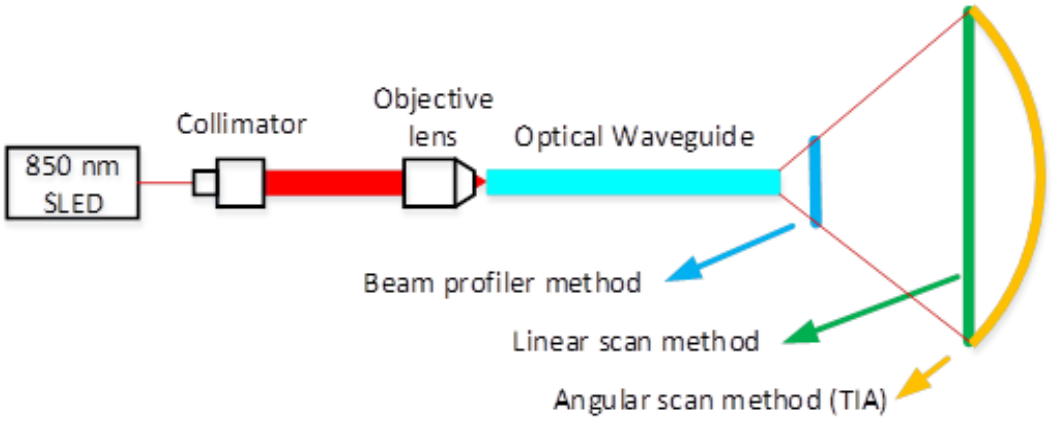

Figure 24. Methods of measuring numerical aperture of a waveguide.

used to calculate the NA. Due to the limited aperture size in the detector, the beam profiler was usually located within 10 mm from the fiber end face. Conversely, in the linear scan method, the

output light intensity was measured along a straight line with a photodetector (PD) and along an angular curve via the angular scan method. The angular scan method is the approved TIA standard measurement method and test procedure for numerical aperture since 2003. The basic requirements for this measurement include a stable light source with a variation less than 10% and bandwidth less than 100 pm HWHM. Although a wavelength of 850 nm (+/- 25nm) is preferred, a constant multiplier can be used to calculate the fiber NA at different wavelengths; for example, the constant is 0.95 for 540 nm and 0.96 for 633 nm. Although a fiber coating is enough to strip the cladding modes, a cladding mode stripper is required for bare fiber. The linear response of the optical detector needs to possess less than a 5% variation over the range of measured intensities. Furthermore, a pinhole aperture may be used to restrict the effective size of the detector to achieve increased resolution. Lastly, the test specimen must be a representative sample of fiber 2.0 m ± 0.2 m in length.

The NA of a step index single mode fiber (SMF) and multimode fiber (MMF) were first measured with the beam profiler method and angular scan method, as shown in Figure 25(a). The results from both methods yielded an NA of 0.14 and were unperturbed upon fiber bending or disruption. Conversely, the NA values determined via the beam profiler method were not consistent for the multimode fiber (MMF). As shown in 25(b), the results varied from 0.16 to

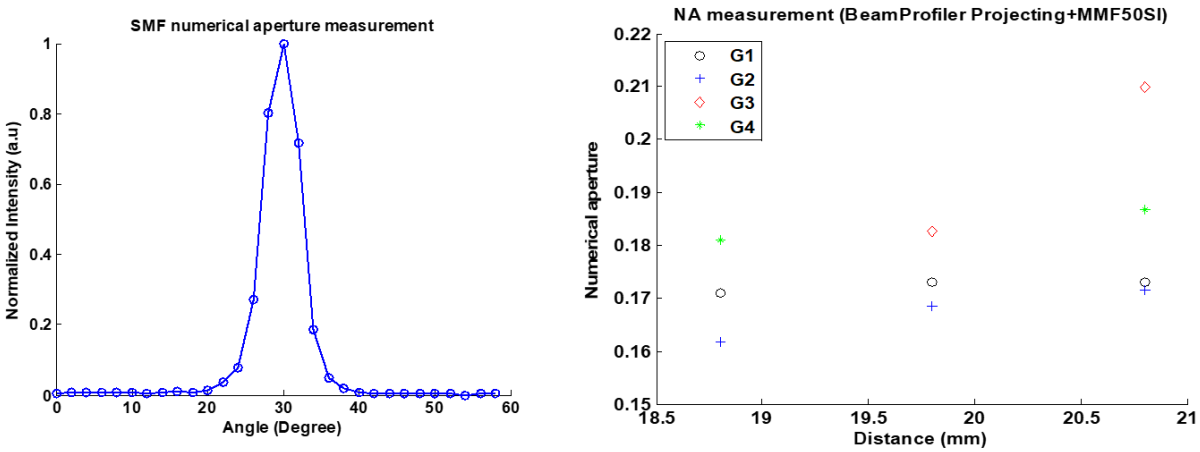

(a) **(b)**

Figure 25. (a) NA measurement result of single mode fiber using angular scan method. (b) NA measurement result of 50/125 µm step-index MMF using beam profiler method. Group 1 (G1) to group 4 (G4) are measured at different time and fiber shape.

0.215. The difference in the measured values was due to mode coupling. A small bending difference to the fiber will dramatically change the modal-coupling pattern. As a result, the test fiber must be completely isolated from vibration for the output intensity pattern to remain constant over the time of testing. Furthermore, the distance from the sensing surface of the beam profiler to the fiber end face can also affect the output light intensity pattern. Although the beam profiler method is a simple and convenient approach, it was found to be only suitable for low NA (<0.15) fiber. Therefore, the other two methods are recommended for higher NA (>0.15) fibers, such as the single crystal sapphire optical fibers.

The light source utilized to evaluate the linear scan method was the same as the one used for the beam profiler method. The PD, PDA36A from Thorlabs, was installed on a 2-D stage that allowed for motion in two directions, parallel and perpendicular to the fiber end face. The scanning area was a rectangular shape, as shown in Figure 26(a). The measured 2-D intensity

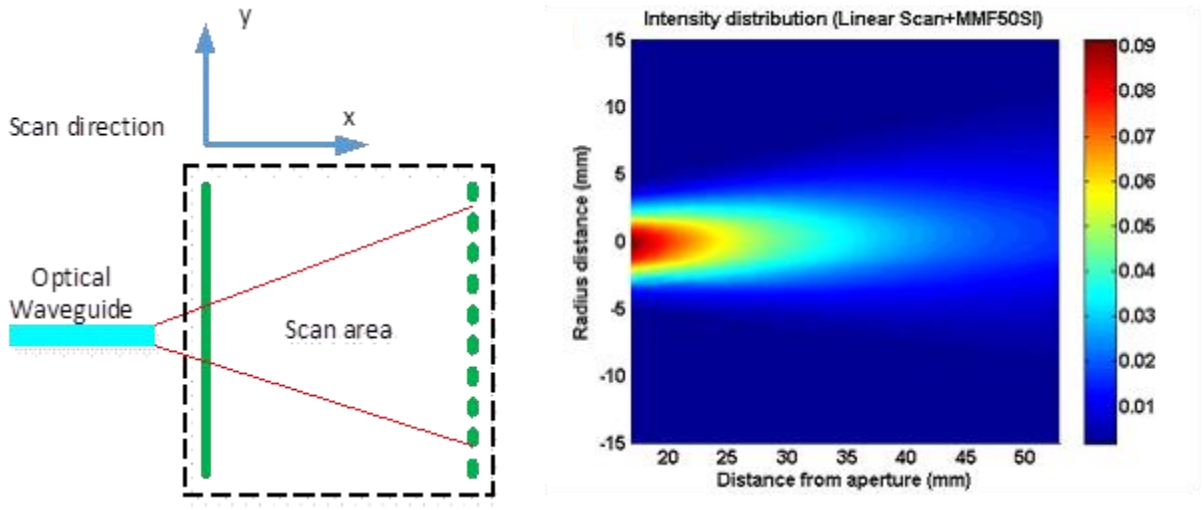

(a) **(b)**

Figure 26. 2D linear scan. (a) The photodetector scans the output light intensity along the x and y-axis and covers the dash-line rectangular area. (b) The 2D map of the output light intensity of a 50/125µm step-index MMF measured with linear scan method.

distribution is shown in Figure 26(b). Based on the 2D intensity distribution, The NA, defined as half of the 5% intensity angle, was calculated based on the 2D intensity distribution along the x-axis. The calculated values reduce exponentially and approach a constant value of 0.189, as shown in Figure 27.

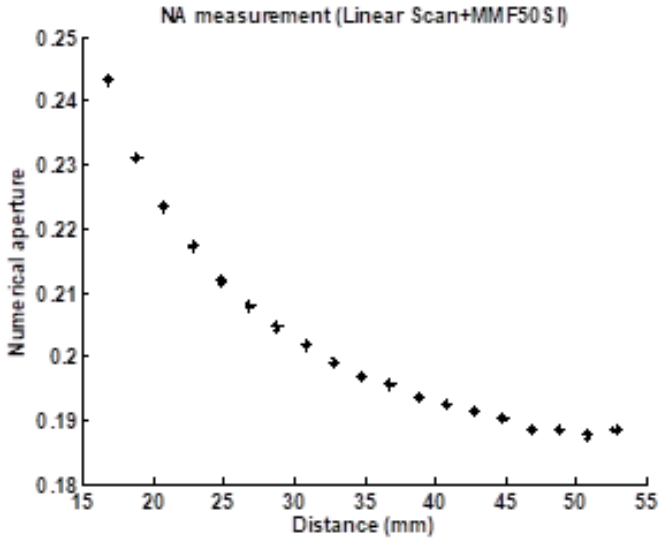

Figure 27. NA measurement result of a 50/125 µm step-index MMF using linear scan method. The NA approaches a constant value when the PD goes away from the fiber end face.

As shown in Figure 28, in the angular scan methods, a scan of the output light intensity is performed along an angular curve in y-direction (Figure 28(a)). By measuring these angular curves at different position along x-direction, a 2D intensity distribution was obtained, as shown in Figure 28(b).

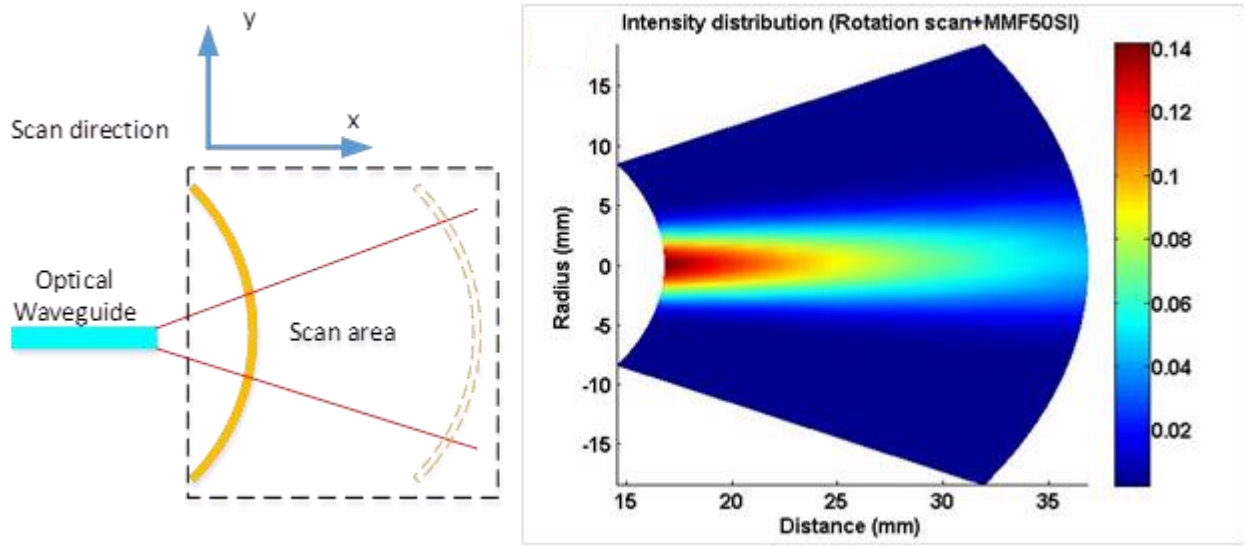

(a) **(b)**

Figure 28. 2D angular scan method. (a) The photodetector scans the output light intensity along an angular curve in y-direction and moves linearly along x-direction. (b) The 2D map of the output light intensity of a 50/125μm step-index MMF measured with angular scan method.

To test he stability of this method, measurements were performed three times with a fiber that was randomly disturbed, with slightly different bending conditions. As shown in Figure 29, the results remained consistent, irrespective of the random spatial condition of tested fiber. The NA measurement results approach a value of 0.203, which were smaller than those obtained by the linear scan method, although the variation was less than 7%. Thus, the annular scan method was employed to measure the NA of the single crystal sapphire fiber.

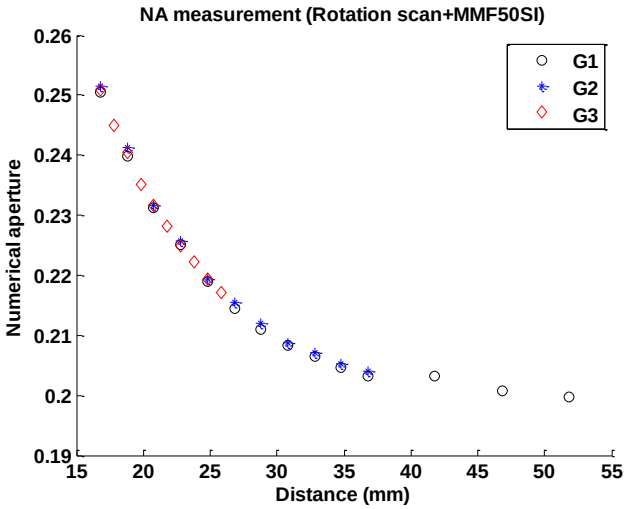

Figure 29. NA measurement result of a 50/125 μm step-index MMF using angular scan method.

The NA of a 0.9 m long, OD 75 µm sapphire fiber was determined via the angular scan method. As shown in Figure 30, the output intensity in the far field was recorded and the calculated NA value was 0.1547. Therefore, utilizing the previously described multiplier constants, the NA at 532 nm was estimated at ~ 0.147. It must be noted that the NA measurement may be reduced by the potential surface scattering that can occur at the interface between the sapphire fiber ceramic tube used to protect the fiber.

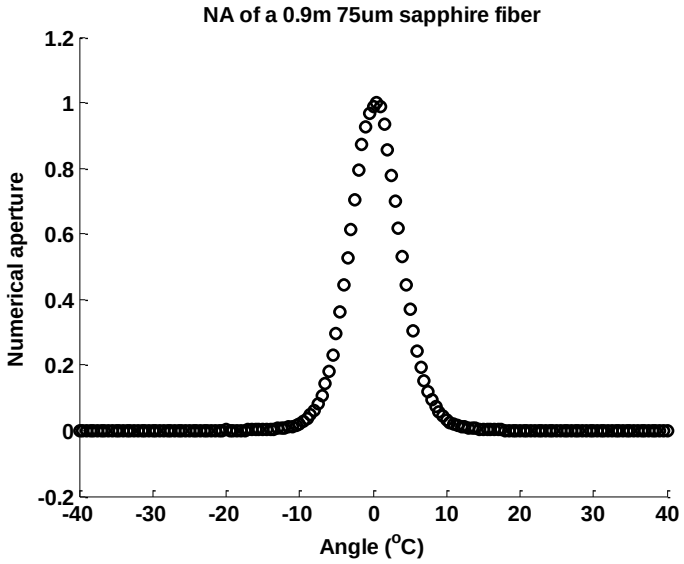

Figure 30. The NA of sapphire fiber at 850 nm.

3.2.3.2Far Field Pattern Measurements

Far field pattern measurements were preformed to to evaluate the reduction in modal volume with the use of the LMV single crystal sapphire optical fiber. Unique etching vessel systems, as shown in Figure 31, were constructed to accommodate consistent etching of straight fiber lengths and protect regions of fiber that should not be etched. In these systems, a fused silica tube was

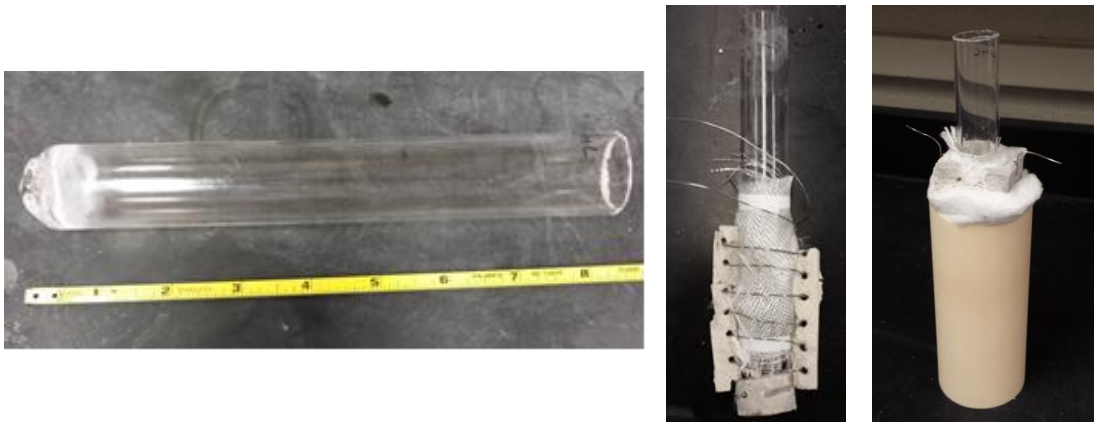

Figure 31. One end of a 1.25" ID fused silica tube was collapsed (left), wrapped with resistance heating wire (middle), and enclosed in an insulated alumina tube (right) to create a vertical straight-fiber etching system accommodating fiber lengths of nearly 20 cm.

cut to length and one end was collapsed to contain the acid mixture and fiber samples; resistance heating wire and insulation were then applied to create an even heating profile along the length of the system. A variable voltage transformer was then connected to the resistance heating wire leads, as in previous systems. The voltage was controlled to reach the desired temperature, which was continously monitored with a glass-protected type-K thermocouple in the etching solution.

Since one end of the sapphire fiber may remain outside of the etching solution, a FC connector was attached prior to etching in an effort to minimize handling after etching and enable optical analysis, as shown in Figure 32. The opposite end of the fiber protruded beyond the end of the PTFE-wrapped glass mounting rod so that far-field intensity patterns could be measured before and after etching.

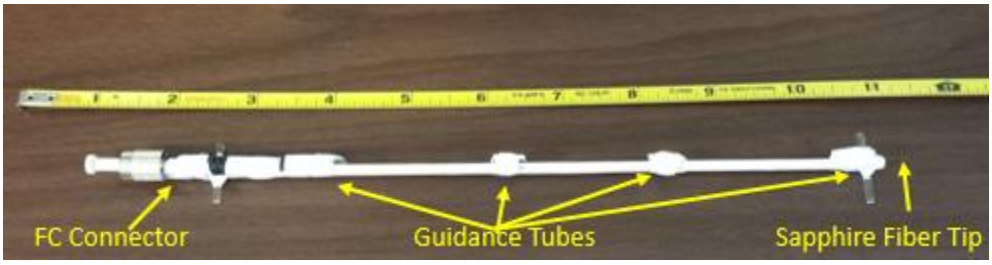

Figure 32. Sapphire fiber attached to a FC connector is mounted to a PTFE-wrapped glass rod with segments of glass tube attached at intervals to maintain fiber orientation throughout etching and testing.

A complementary improvement to sample preparation involved the low-loss protection of the fiber at the air-acid interface present during the etching process. Deposition of aluminum sulfate and aluminum phosphate on the surface of the fiber may occur during the etching process. In a vessel where the fiber is mounted vertically and partially submerged in the etching solution, it was discovered that the location with highest propensity for redeposition lies along the acid-air interface at the top of the acid solution. Removal of the deposits via chemical or mechanical means without damage and/or increased scattering losses was attempted with limited success, as is easily visible in Figure 33.

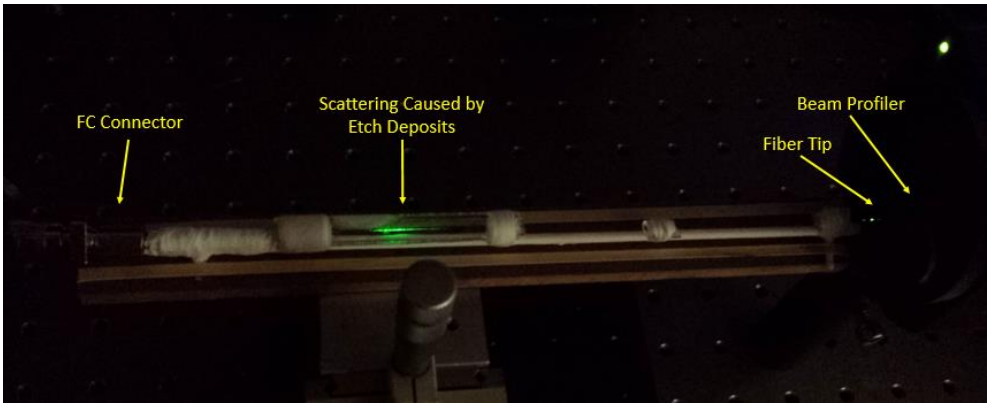

Figure 33. Aluminum sulfate/phosphate deposited on fiber surface at a concentrated location during etching causes significant scattering loss, visible using a 532nm green laser.

Significant efforts dedicated to the development of a reliable, low-loss, non-permanent method to protect this region during etching produced a very effective and relatively simple protection scheme. Using a hydrogen torch and glass lathe, as shown in Figure 34(a, b), borosilicate glass tubing was collapsed on the sapphire fiber to provide a resilient, signal-enhancing protective cladding at the region of the air-acid interface. Hydrofluoric acid was then used to remove all but the few centimeters required to protect this region from the deposition of deposits upon etching. Since the thermal expansion properties of borosilicate glass and sapphire are similar, the configuration has proven to be mechanically reliable upon heating and cooling. Also, while the

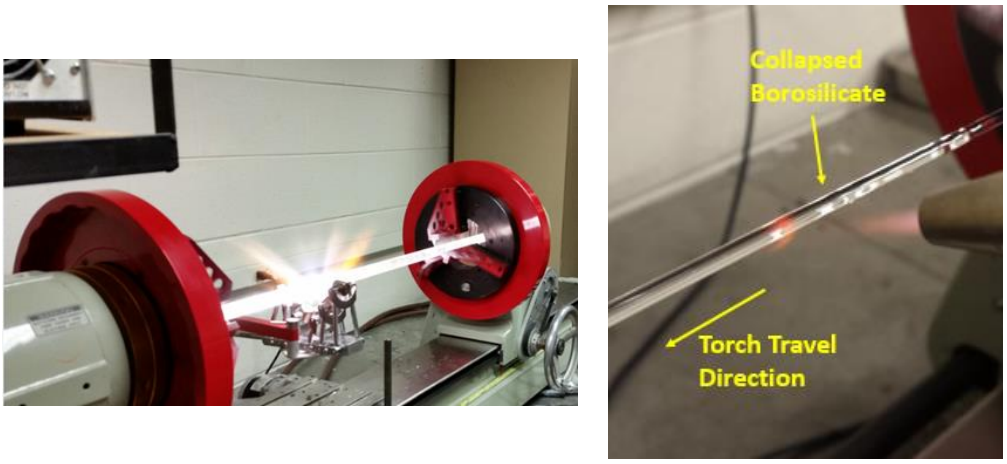

(a) **(b)**

Figure 34. (a) Custom glass-working lathe. (b) Borosilicate tubing provides a protective cladding for the sapphire fiber during etching, applied using a hydrogen torch and glass lathe

length of unprotected, etched fiber is sufficient to eliminate effects of this cladding on measured optical properties compared to bare fiber, the protective borosilicate may easily be removed after etching using HF without risking damage to the sapphire fiber sample.

The NA of a sapphire fiber is not well defined because the fiber is not perfectly circular and uniform in cross section and is uniaxial. Subsequently, much care must be taken upon performing far field pattern measurements. As shown in Figure 35, the difference in numerical aperture and spot size between the MMF and SMF fibers butt-coupled to the single crystal sapphire fiber can have a significant effect on field pattern intensity.

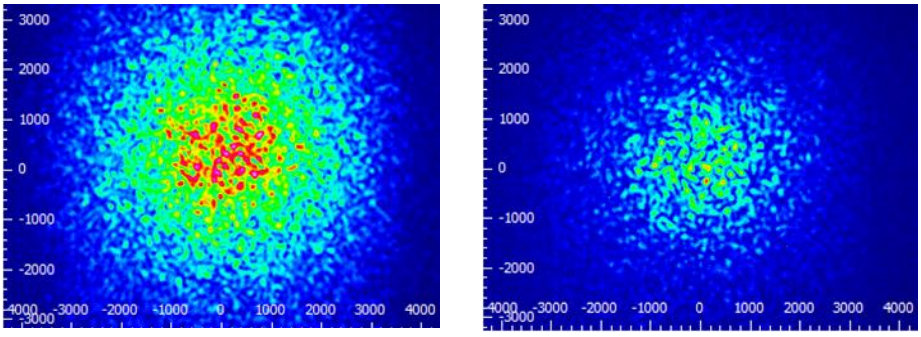

(a) **(b)**

Figure 35. The far-field intensity patterns for a 70 um sapphire optical fiber at a wavelength of 532nm with a MMF (a) or SMF (b) as a lead-in.

The far field measurements were performed after polishing the tip of the single crystal sapphire fiber samples using 100 nm diamond lapping film (Ultra Tec) to remove facets caused by the preferential etching of the r-plane. The far-field patterns of the reduced-diameter sapphire fiber were captured at intervals to collect data at many different diameters. Three 5 mW laser wavelengths were used: 532 nm, 783 nm, and 983 nm (Thorlabs) in order to expand the breadth of data collected per measured diameter. The light emanating from the lasers was focused into the fiber using a 40x objective lens, whose numerical aperture (NA) is larger than that of sapphire, ensuring the modal state would be "overfilled". A BC-106VIS CCD beam profiler (Thorlabs) was used to capture the far-field profiles, which were then catalogued using Thorlabs' BEAM 6.0 software. Most components were mounted on 2-or 3-axis stages to aid alignment. A sample under evaluation using the described setup is visible in Fig. 36.

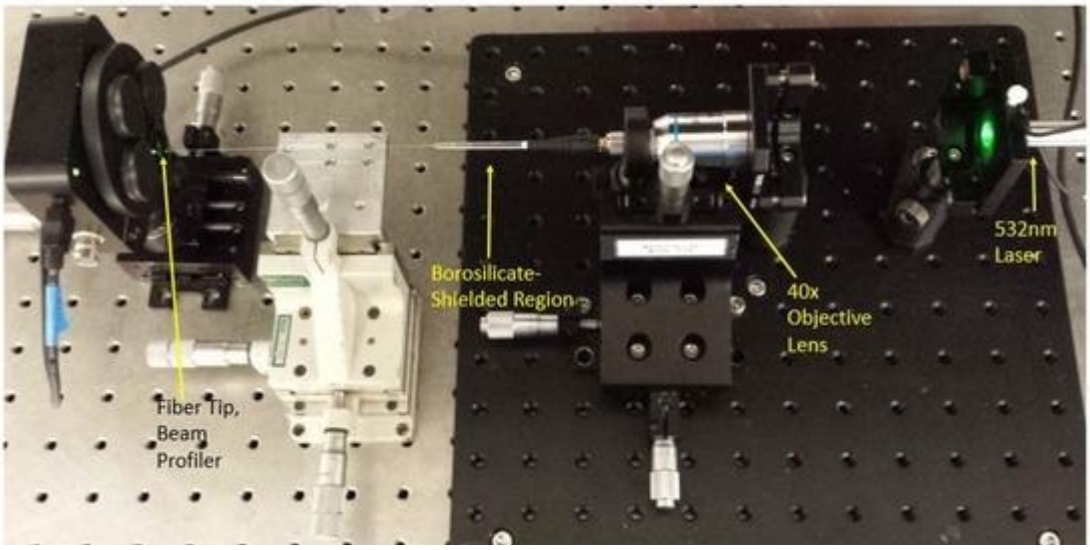

Figure 36. Far-field measurements were taken using a CCD beam profiler and minimal focusing optics. The sapphire fiber with its glass-shielded region, FC/PC connector, and exposed sapphire fiber before etching is seen during analysis using a 5 mW 532 nm laser.

The far-field speckle patterns of the sapphire fiber were captured at several diameters ranging from 125 µm down to a final diameter of 6.5 µm using laser wavelengths of 532 nm, 783n m, and 983 nm, as seen in Fig. 37. At the initial sapphire fiber diameter of 125 µm, where nearly a million modes are theoretically supported at lower wavelengths, the speckle patterns consistent with highly multimodal projections were observed. As the diameter decreased, the number of speckles decreased and individual speckles broadened in diameter, corresponding to the reduction in supported modes causing the interference peaks and valleys to which the speckles correspond.

At a sapphire fiber diameter of 6.5 µm, low order LP_{11} and LP_{01} modes become visible at the tested wavelengths. As may be anticipated, the smaller 532 nm wavelength exhibits the higher-order LP_{01} mode while only the fundamental mode is supported at wavelengths of 783 nm and 983 nm. Modifications were made to excitation conditions to validate these observations. First, the injection angle of the laser into the fiber was altered by 15°; if the observed far-field patters were truly stable, it could be expected that the patterns would not change significantly. This was shown to be the case, as seen at the bottom of Fig. 36; the LP_{11} mode was once again visible at a

wavelength of 532 nm, and the fundamental LP_{01} mode was observed at 783 nm. Only scattered light was captured at the 983 nm wavelength, perhaps due to lack of collimation as the light entered outside the acceptance angle of the fiber, or simply due to alignment difficulties for this particular measurement.

Additional modifications to the input conditions further bolstered the conclusion that fabrication of single-mode air-clad sapphire optical fiber was successfully demonstrated. The previous measurements were taken via direct input of the laser sources, using an objective lens to focus light into the optical fiber. In Figure 38, the far-field projections observed through direct laser input were compared to those observed when 1 m and 2.5 m patch cables (SMF-28e and 50/125 step-index MMF, respectively) were butt-coupled to the sapphire fiber, receiving the laser light themselves through direct input.

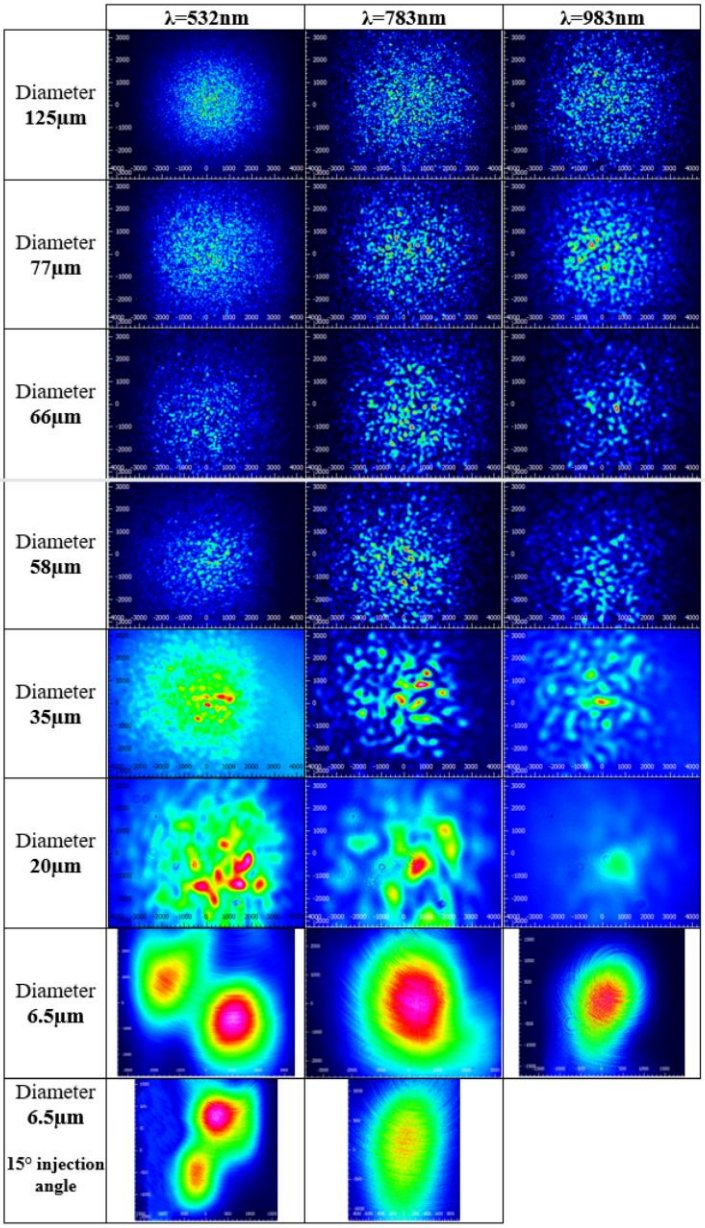

Figure 37. Far-field measurements were taken at varying diameters using laser wavelengths of 532 nm, 783 nm, and 983 nm. Low-order modes became visible at a sapphire fiber diameter of 6.5 µm, and measurements were consistent when the light injection angle was altered by 15°.

No significant differences were evident in the mode properties exhibited regardless of input method. The LP_{11} mode was still observed at 532 nm whether direct, SMF, or MMF input is used, and the fundamental LP_{01} mode was observed at 783 nm and 983 nm. As anticipated, the intensity of the SMF-input signal was lower than others (preventing the capture of a far-field projection at 983nm due to the insufficient sensitivity of the profiler), but the mode patterns did not change. It may therefore be stated with confidence that air-clad sapphire optical fiber will exhibit single-mode behavior at 783 nm and greater when its diameter is 6.5 µm or less.

The experimental results contradict the theoretical estimations of modal volume for a step-index fiber using standard models that predict the support of ~461-1614 modes at wavelengths of 532-983 nm and an air-clad sapphire fiber diameter of 6.5µm. Per convention step index waveguide

theory, the fiber diameter must be less than 500 nm to achieve single-mode behavior in air-clad sapphire over this wavelength range.

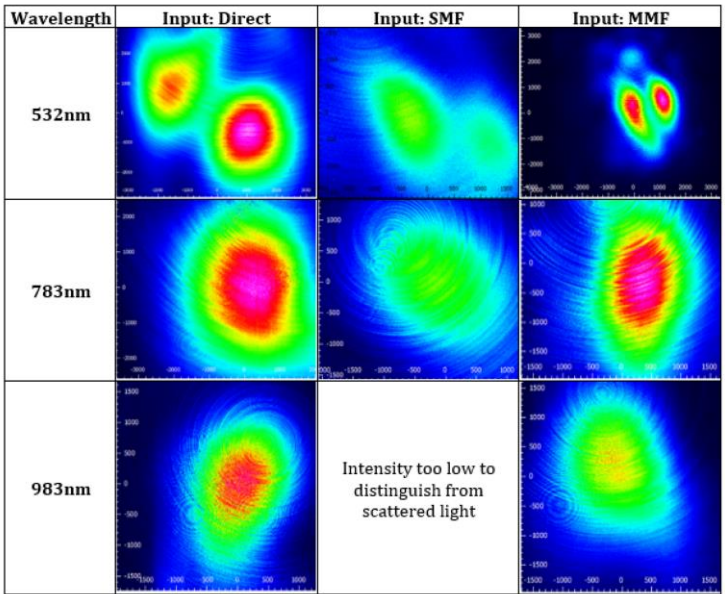

Figure 38. Altering the input conditions by butt-coupling SMF-28e and 50/125 step-index MMF patch cables did not change the mode properties observed using direct input.

The discrepancy arose from the assertion that the NA of a sapphire fiber is not well defined. Traditional step-index waveguide theory cannot be assumed for sapphire fiber because the cross section is not perfectly circular and uniform in diameter as well as optically isotropic. Single crystal sapphire fibers have an approximately rounded hexagonal cross-sectional shape (for the standard c-axis orientation), its surface is not perfectly smooth, and the sapphire crystal is uniaxial. Thus, the calculations of the theoretical numerical aperture of single crystal sapphire optical fiber were not valid for modal volume predictions.

If the theoretical numerical aperture of c-plane sapphire depended solely on the refractive index of core, cladding (air in this case), and ambient environment n_0 (also air), would be 1.4, which is impossible because it is greater than the practical NA limit of 1. It is well-known that the *effective* numerical aperture of sapphire varies greatly from its theoretical NA due to non-circular cross section (sapphire fibers are slightly hexagonal due to its crystal structure), attenuation factors, and other parameters which seem to be influenced by fiber diameter. For instance, researchers and manufacturers have previously reported measured effective NA's of ~0.35 at λ=2.94 µm for unclad sapphire fiber at a diameter of 300 µm and ~0.45 at λ=633 nm and a diameter of 125 µm. Replacement of the erroneous theoretical NA with a measured effective NA would provide calculations that more closely match the experimental observations.

A common method for evaluating numerical aperture of single mode optical fibers was employed to determine the effective NA of the 6.5 µm sapphire fiber measured in this study; essentially, the beam width of the fundamental mode was measured (4σ cutoff intensity) at a nominal distance from the beam profiler and then measured again when moved 1 mm away from the profiler. The resulting calculation of divergence angle provided an approximate measurement of the effective numerical aperture.

Effective NA measurements were acquired using the 983 nm laser, where the 6.5 µm air-clad sapphire fiber was decidedly single-mode. Measurements were first taken on SMF-28e fiber to provide a control for the measurements. Five measurements were taken, yielding a measured effective NA of 0.113 and a standard deviation of 0.029. The published NA of SMF-28e is 0.14, but that is at λ=1313 nm, which exceeded the detection window of the beam profiler used in this experimentation. At 983 nm, SMF-28e appeared to support both the LP_{11} and LP_{01} modes, so the

mode field was somewhat distorted, resulting in less precise mode field measurements because of these hybrid modes. As the sapphire fiber produced a consistent LP_{01} mode, these inaccuracies would not persist in sapphire measurements as exemplified by the 0.008 standard deviation in measurements of the 6.5 μm-diameter sapphire fiber, whose effective NA was measured to be 0.090. Furthermore, by using the effective numerical aperture of 0.090, an excellent agreement between the theoretical model and the observed modal behavior was exhibited. The effect of this NA value replacement is illustrated in Figure 39, where the theoretical maximum radius for air-clad sapphire optical fiber that will support only a single mode is plotted versus input wavelength

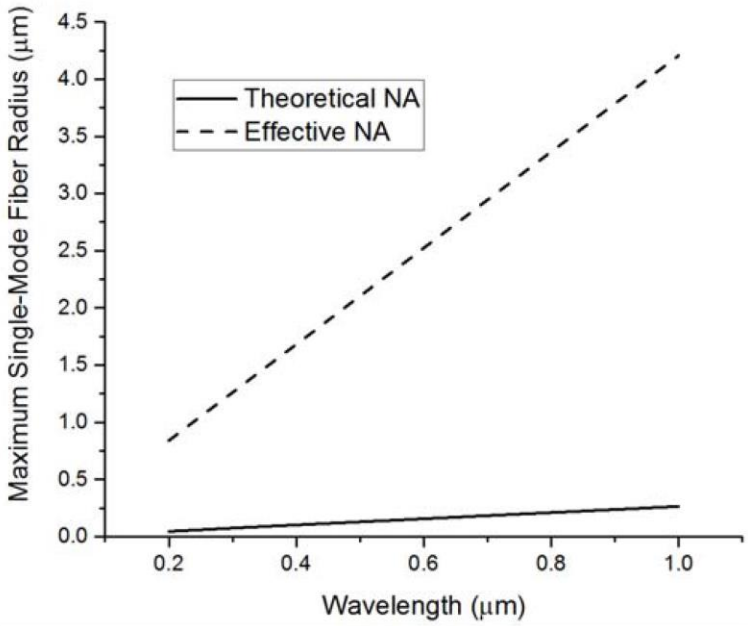

Figure 39. The predicted maximum air-clad sapphire optical fiber radius that will support only a single mode changes significantly when the measured effective numerical aperture (0.090) is substituted for the theoretical numerical aperture (1.4) in step-index approximations. The predicted single-mode cutoff using the measured NA_{eff} in these approximations agreed with experimental observations.

for both numerical aperture values. This plot was generated by solving the standard V-parameter equation ($V = \frac{2\pi}{\lambda} a \cdot NA$) for radius, where V=2.405 is the cutoff for single mode behavior.

The variation between the predicted fiber radius required for single-mode operation as yielded through substitution of effective NA versus and that calculated using the theoretical NA was significant. Using the effective NA measured for the 6.5 μm-diameter sapphire fiber, it was predicted that only the fundamental mode will be supported at wavelengths greater than ~760 nm, which is in fact what was observed experimentally. As it appeared, the effective numerical aperture was significantly dependent upon sapphire fiber diameter. Effective numerical measurements would need to be taken at any given fiber diameter to improve the accuracy of predictions at other fiber diameters, but extrapolation using the NA_{eff} at a diameter of 6.5 μm in the range of 0-9 μm diameter is certainly within a reasonable window of accuracy.

3.2.4 Minimum Bend Radius for LMV Sapphire Fiber

The LMV fiber must also exhibit the necessary mechanical resilience required for system integration and deployment, which can be evaluated via tensile stress applied to the surface of the fiber upon bending. A shown in Figure 40(a), a bend radius of ~ 4 mm was readily achieved with a single crystal sapphire fiber etched from 125 µm to 70 µm. Furthermore, it was shown that the minimum bend radius increases greatly as fiber diameter decreases, as shown in Figure 40(b).

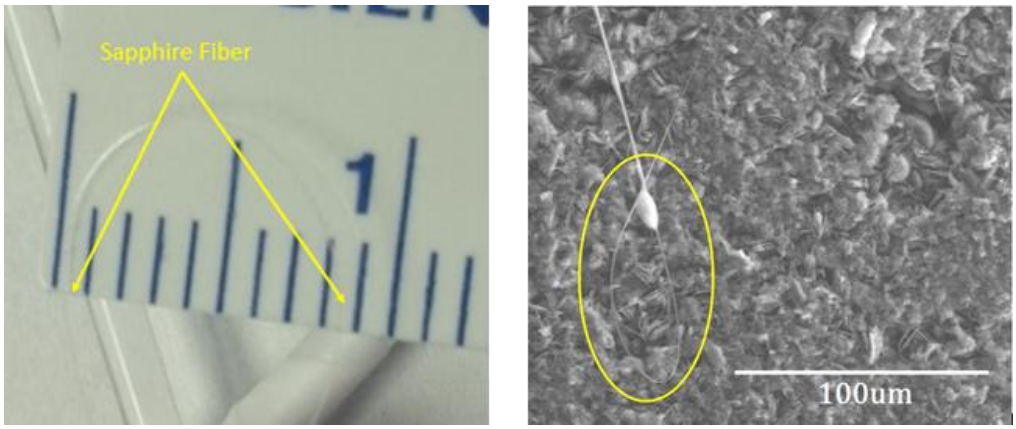

(a) **(b)**

Figure 40. (a) Sapphire fiber etched from 125µm to 70µm demonstrated bend radius of less than 4mm (scale marks represent 1mm). (b) Sapphire microfiber demonstrates bend radius of less than 10µm.

3.2.5 Extended Length LMV Sapphire Fiber

The fabrication of relatively long lengths (~1 meter) of low modal volume sapphire fiber was also a demonstrated for applicable sensing spans. A larger etching system was constructed as shown in Figure 41, with a 1.2 m fused silica glass tube forming the etching enclosure, to etch

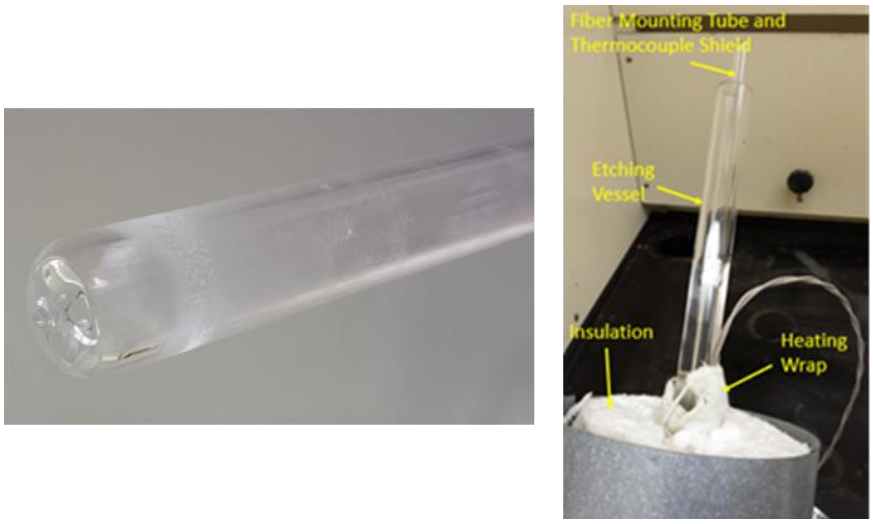

Figure 41. 1" ID fused silica tube with one end enclosed forms the etching vessel (left); heating wrap, insulation, and a fiber mounting tube complete the setup for etching fiber of 1m length (right).

the entire length of a 1 meter sapphire fiber. One end of the tube was collapsed on the lathe, inserted in a mullite tube (to add thermal mass for greater etch rate consistency along the length) and enclosed by Omegalux heating wrap. This entire structure was then surrounded by alumina insulation and a sheet metal casing. The sapphire fiber was mounted to the exterior of a smaller fused silica tube (also with one end collapsed) using Teflon tape; this smaller tube was also used to encase a thermocouple to monitor temperature, as shown in Figure 40 (b).

A 125 µm diameter sapphire fiber was reduced to ~90 µm over the course of approximately 14 hours of etching in the 3:1 H_2SO_4:H_3PO_4 solution, as shown in Figure 42. In this first attempt,

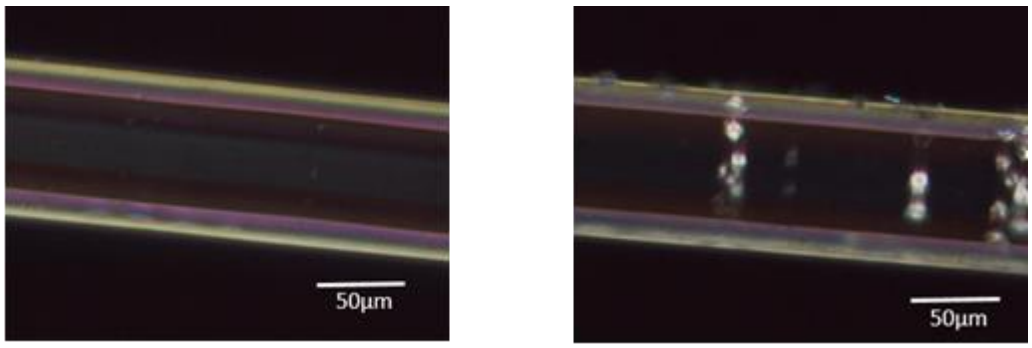

(a) **(b)**

Figure 42. 0.9 m of a 1 m sapphire fiber demonstrates consistent diameter from tip-to-tip after reducing the diameter from 125 µm to 90 µm. The majority of the fiber surface is clean (a); some etch deposits are visible near the air-acid interface region (b).

approximately 0.9 m of the 1 m length of sapphire fiber was consistently etched; the top ~10 cm was exposed to air after evaporation of some of the etching solution. As a result, this top portion was etched to a lesser degree and also accumulated etch deposits at the air-acid interface.

The surface of the fiber was free of permanent deposits (with the exception of the ~10 cm end region at the air-acid interface), though a few removable residues that existed increased the overall attenuation of the fiber. As shown in Figure 43, the as-received 1 m sapphire optical fiber

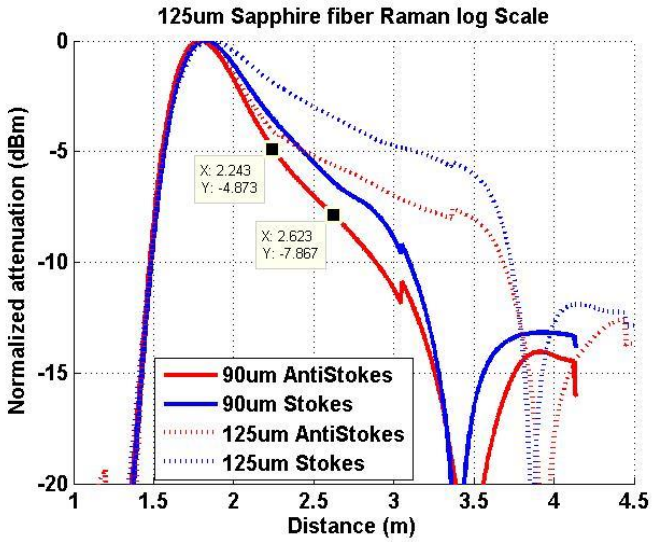

Figure 43. The slope-attenuation measurement technique enables accurate evaluation of loss for comparison between etched and unetched fibers

with a 125 µm diameter maintained an attenuation of approximately 3.5 dB/m. Immediately after etching to ~90 µm, the attenuation was measured to be ~10.3 dB/m. The measured attenuation was further reduced to ~7.8 dB/m after a mild cleaning using isopropanol attenuation. To the best of our knowledge, this has been the first time this type of attenuation measurement has been performed in single crystal sapphire fibers.

To demonstrate the repeatability of the fabrication technique, two long-length sapphire fibers were produced with greatly reduced diameters. One fiber with a nominal diameter of 20 µm was fabricated at a measured length of approximately 0.5 m, as shown in Figure 44. Its diameter tapered smoothly from 23 microns to 16 microns**.** An additional sapphire fiber, tapering smoothly from 51 µm to 38 µm, was fabricated to a length of one full meter in length (Figure 45). In addition, no discernible etching deposits were noted on the fiber and the entire length of fiber was usable. Tapering was caused by slight differences in solution temperature and turbulence caused by gas bubbles traveling the length of the fiber as solution evaporates. Although minor, these small differences are compounded over the many hours required to etch the fiber down to the observed diameters and can be minimized by simply flipping the fiber end-to-end between etching sessions.

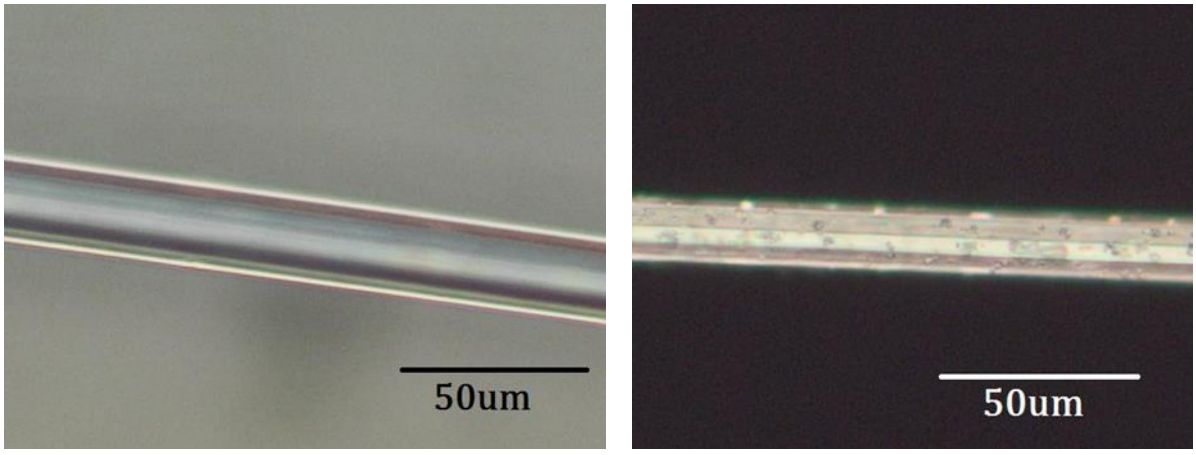

(a) **(b)**

Figure 44. ~0.5m length of sapphire fiber has been created with a diameter tapering from 23µm at its base (a) to 16µm at its tip (b). The deposits seen on the tip region are largely non-permanent and will be removed and imaged again after initial testing is complete.

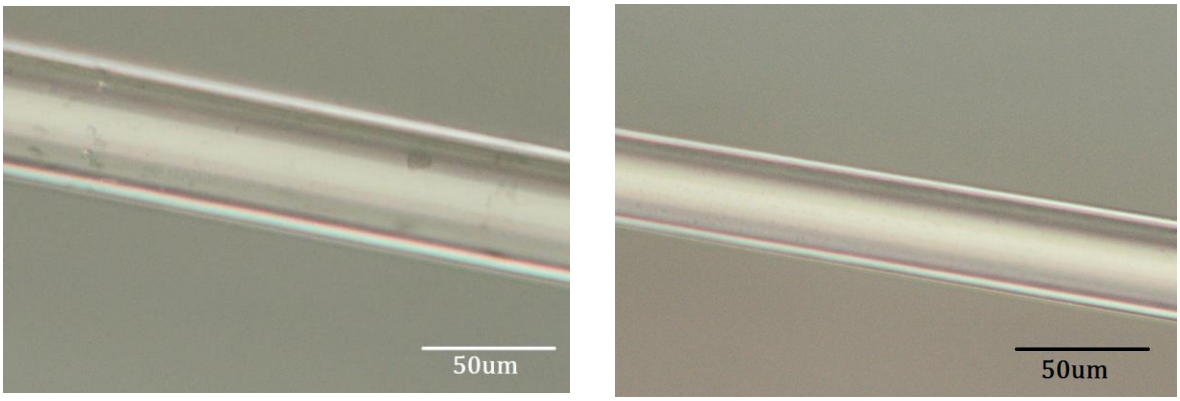

(a) **(b)**

Figure 45. A 1 meter length of sapphire fiber has been etched down to a diameter of 51um (a) to 38um (b).

3.3 Micro-Structured Single Crystal Sapphire Fibers

3.3.1 "Windmill" Single Crystal Sapphire Fiber Design

In addition to the reduced diameter single crystal sapphire fiber, a type of single crystal sapphire optical fiber (SCSF) design was proposed to reduce the number of guided modes via a highly dispersive cladding with a periodic array of high- and low-index regions in the azimuthal direction, as shown schematically in Figure 46. The basic design is similar to "segmented cladding" fibers that have been demonstrated in fused silica based optical fibers [40-43]. The

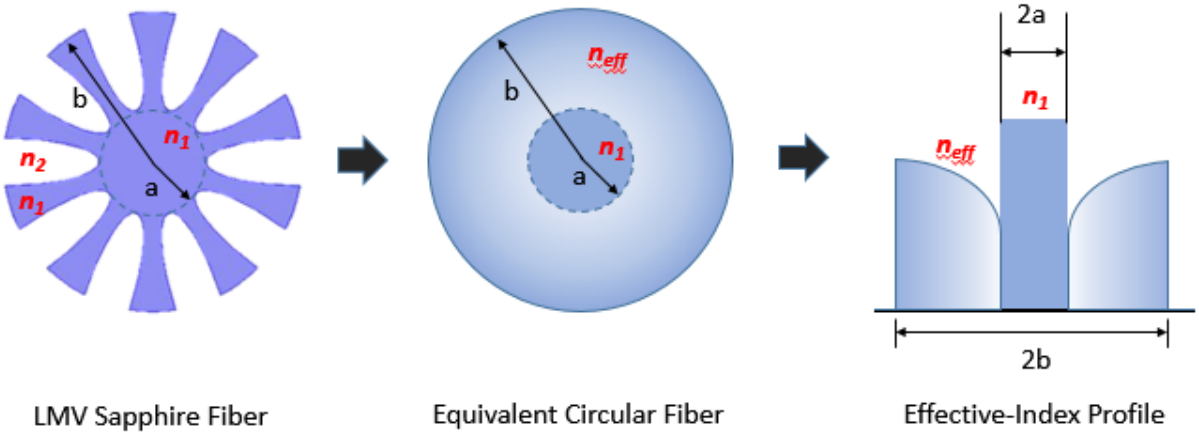

Figure 46. The concept of REIM of the LMV fiber with an equivalent circular fiber with a radially varying effective cladding index profile [39].

structure retains a "core" region in the center of the fiber with alternating high and low index region in the azimuthal direction, and a uniform cladding in the radial direction, akin to a finned dielectric planar waveguide [43-48]. The structure retains a "core" region of pure single crystal (SC) sapphire (n ≈1.77).in the center of the fiber and a "cladding" region of alternating layers of air (n = 1) and SC sapphire in the azimuthal direction that is uniform in the radial direction. The modal characteristics and confinement losses of the fundamental mode were analyzed via the finite element method by varying the effective core diameter and the dimensions of the "windmill"-shaped cladding. The simulation results showed that the number of guided modes was significantly reduced in the windmill fiber design, as the radial dimension of the air and SC sapphire cladding regions increase with corresponding decrease in the azimuthal dimension.

The "windmill" fiber design creates an "effective cladding" in which the average refractive index is reduced, generally, via the average index of air and sapphire which is dependent on the fraction of air and sapphire. The decrease of the fiber's diameter and/or NA, as well as the addition of voids in the cladding reduce the number of modes confined in the core. Confinement loss (CL) due to a finite number of holes can be estimated in a fiber. CL describes the ability of the core to confine the light, which is also known as the confinement capability. SCSF with a low modal volume and high confinement capability is preferred and can be achieved by a proper fiber structure design. Numerical modeling was performed to demonstrate that by controlling the cladding parameters one can achieve modal reduction on SCSF with an acceptable CL of the fundamental mode. In all cases, we do not consider the chromatic dispersion associated with the

refractive index of the material. The "windmill"-shaped SCSF was theoretically evaluated to understand the effects induced by the special geometry of the modal reduction.

Numerical simulations were performed to evaluate the influence of the fiber diameter and structure on the confinement loss (CL), as defined by the following,

$$CL = \frac{2 \times 10^{10}}{\ln 10} \frac{2\pi}{\lambda} \mathrm{Im}\left[n_{eff}^{i}\right] \quad dBm/km \qquad \left(i = x, y\right) \tag{15}$$

where $lm\left[n_{eff}^{i}\right]$ is the imaginary part of the effective index of the guided mode [49]. The refractive index of the core (SC sapphire) and cladding (air) are 1.772 and 1, respectively, at the incident wavelength of 532 nm [50]. A direct linear system solver (UMFPACK), in the COMSOL Multiphysics® software package, was implemented to complete the modal analysis of a selected LMV design by solving near the effective index of the SC sapphire for a discrete number of modes. The number of solvable modes was typically set at 3000. All the simulations were performed through several iterations until a solution converged that met a defined error limit, however, not all the values can be used in the analysis. Three conditions must be satisfied:

1. The effective index (n) should equal or larger than 1;
2. The value of the calculated confinement loss (CL) should larger than 0;
3. There should be "clear" and symmetric patterns for E field distribution.

The first condition arises from the permissible range of refractive indices for modes bound to the "core" region, which should be larger than cladding, but smaller than core [51]. Since the number of modes were defined prior to the simulation, *spurious modes* were included if this set value was larger than the possible number calculated by FEM, as shown in Figure 47. As

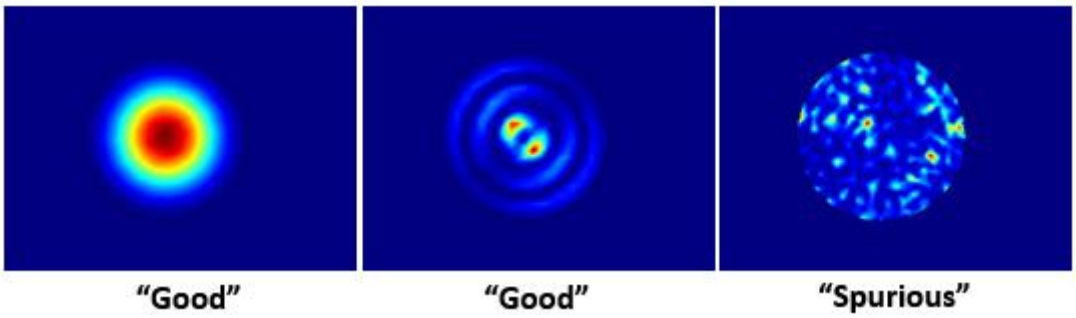

Figure 47. Actual and spurious modes generated upon simulation

defined by Schroeder, et al, a *spurious mode* is "a result of the numerical solution process which does not correspond to one of the physical modes which the waveguide or resonator under consideration actually supports" [52]. The second condition is apparent because the CL is an energy-dissipation-phenomena and therefore must be a positive number. The last condition is predicated by the solutions for the modal equations in step-index fibers [51].

The LMV sapphire fiber is a leaky structure and all the modes suffer from a finite leakage loss that can be tuned to preferentially leak the higher order modes; i.e. the higher order modes will have a higher confinement loss than the lower order modes. As shown, conceptually, in Figure 48, the higher modes tend to propagate in the "wings" of the "windmill" cladding, while the

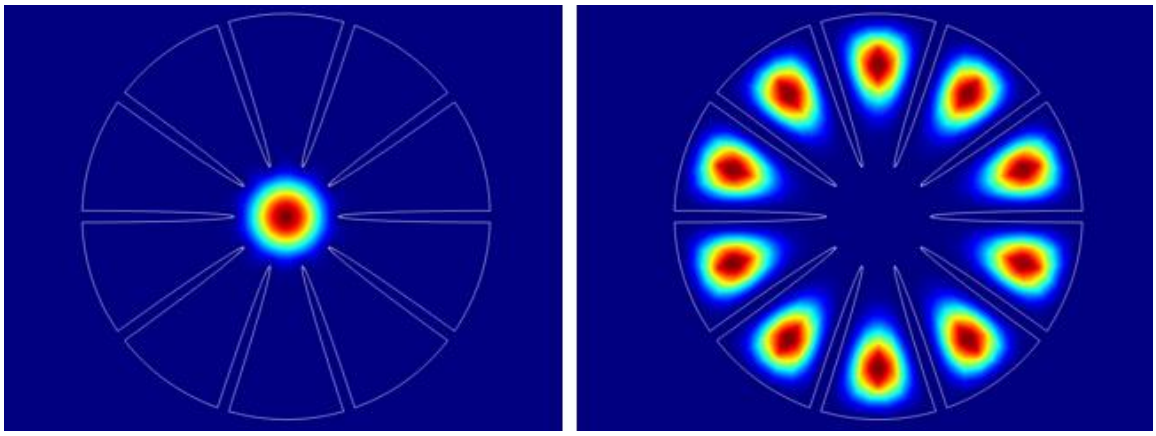

(a) **(b)**

Figure 48. Propagation of (a) the lower order modes in the core region and (b) the higher order modes in the segmented cladding.

lower order modes remain in the "core" region of the fiber. Significantly larger leakage is experienced by these higher order modes with respect to the lower order modes propagating in the core region.

Optical modeling was performed to compare the propagation characteristics between a single crystal sapphire fiber with a diameter of 25 microns and complementary LMV fiber design. Selected images of the power flow in the z for both the LMV fiber design and the standard 25 μm fiber are shown in Figure 49. Although the power flow for the lower order modes, such as LP_{01} and LP_{11}, are similar for both designs, the confinement loss is approximately two order of magnitude greater in the LMV fiber design.

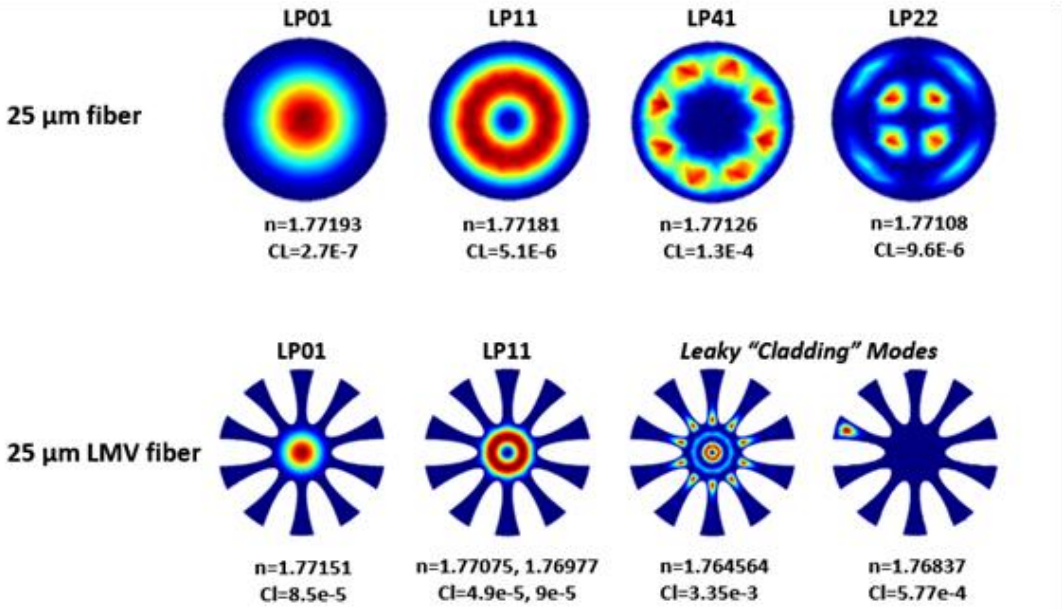

Figure 49. Propagation of (top) the lower order modes in the core region and (bottom) the higher order modes in the segmented cladding.

3.3.2 Theoretical Analysis of Single Crystal Sapphire "Windmill" Fiber Design

In cylindrical coordinates, the Maxwell equations for EM fields in optical fiber with invariant index profiles along z direction can be decomposed into longitudinal and transverse components by[53]:

$$\xi(x,y,z,t) = \{\xi_t(x,y) + \xi_z(x,y)\}\exp[-j(\omega t - \beta z)] \quad , \quad (16)$$

where ξ denotes E or H field and the subscript t and z denote the transverse and longitudinal components respectively. The leakage loss of a particular mode can be represented by the imaginary part of complex propagation constant β. A special boundary condition of the computational domain, a perfect matched layer (PML), is applied to calculate β. A PML is a layer surrounding the computational domain, which can theoretically absorb without reflection any kind of wave traveling towards boundaries. The CL of optical fiber can be estimated by employing a PML. For light propagating along the z direction, the Maxwell equations for optical waveguide with an anisotropic-type PML boundary condition are expressed as [53]:

$$jk_0 s\varepsilon_r E = \nabla \times H \quad (17)$$

$$-jk_0 s\mu_r H = \nabla \times E \quad (18)$$

and [15],

$$\nabla \times (s^{-1}\nabla \times E) - {k_0}^2 n^2 sE = 0 \quad (19)$$

$$\nabla \times \left(\frac{1}{n^2} s^{-1}\nabla \times H\right) - {k_0}^2 sH = 0 \quad (20)$$

with

$$s = \begin{bmatrix} {s_y}/{s_x} & 0 & 0 \\ 0 & {s_x}/{s_y} & 0 \\ 0 & 0 & s_x s_y \end{bmatrix} \quad (21)$$

$$s_x = 1 - \frac{\sigma_x}{j\omega\varepsilon_0}, s_y = 1 - \frac{\sigma_y}{j\omega\varepsilon_0} \quad (22)$$

where:

E: electric field; μ_r: relative magnetic permittivity complex tensors;

H: magnetic field; n: refractive index; λ: being the wavelength;

β: complex propagation constant; s: PML matrix; σ: conductivity profile;

$k_0=2\pi/\lambda$ is the wave number in the vacuum; ω: angular frequency

ε_0: free space dielectric permittivity;

The eigenvalue equations obtained for E and H field are shown as follows [53]:

$$\begin{bmatrix} P_{xx} & P_{xy} \\ P_{yx} & P_{yy} \end{bmatrix} \begin{bmatrix} E_x \\ E_y \end{bmatrix} = \beta^2 \begin{bmatrix} E_x \\ E_y \end{bmatrix} \tag{23}$$

$$\begin{bmatrix} Q_{xx} & Q_{xy} \\ Q_{yx} & Q_{yy} \end{bmatrix} \begin{bmatrix} H_x \\ H_y \end{bmatrix} = \beta^2 \begin{bmatrix} H_x \\ H_y \end{bmatrix} \tag{24}$$

Further detail regarding the P and Q matrices can be found in reference [53]. Solving the eigenvalue equations, the propagation constant β can be obtained in a complex form:

$$\beta = Re(\beta) + Im(\beta) , \tag{25}$$

where Re (β) and Im (β) are the real and imaginary part of β.

And the CL can be calculated by [53, 56, 57]:

$$Cl = 8.686 Im(\beta) . \tag{26}$$

Due to the complex calculation in the eigenvalue equations, we used advanced numerical techniques combined with finite element method (FEM) to perform comprehensive analyses in our study. The CL in optical fiber via the implementation of the FEM method in a commercial software package COMSOL Multiphysics®. A modified eigenvalue equation [53] was applied in FEM analyze:

$$\nabla \times (\mu^{-1} \nabla \times E) - \lambda E = 0 \tag{27}$$

$$\lambda = {k_0}^2 (\varepsilon_r - \frac{j\sigma}{\omega}) \tag{28}$$

Where, λ is the eigenvalue. For time-harmonic problem, the electric field for out-of-plane propagation can be written as [53] :

$$E(r,t) = Re(\tilde{E}(r) e^{j\omega t - \beta z}) , \tag{29}$$

where, $\tilde{E}$ is a phasor and z is the known out-of-plane direction and,

$$\beta = Re(\beta) + Im(\beta) = -\lambda. \tag{30}$$

In practice, SC sapphire optical fibers maintain a hexagonal shape, which becomes more pronounced with the reduction of a diameter. The core shape changes from circle to hexagonal with intermediate transition structure during etching process. Therefore, we used hexagonal with 25 μm, 10 μm and 1 μm inscribed diameters as the core to simulate the etched SC sapphire fiber. The core structure, FEM meshes and simulation result are shown in Figure 50.

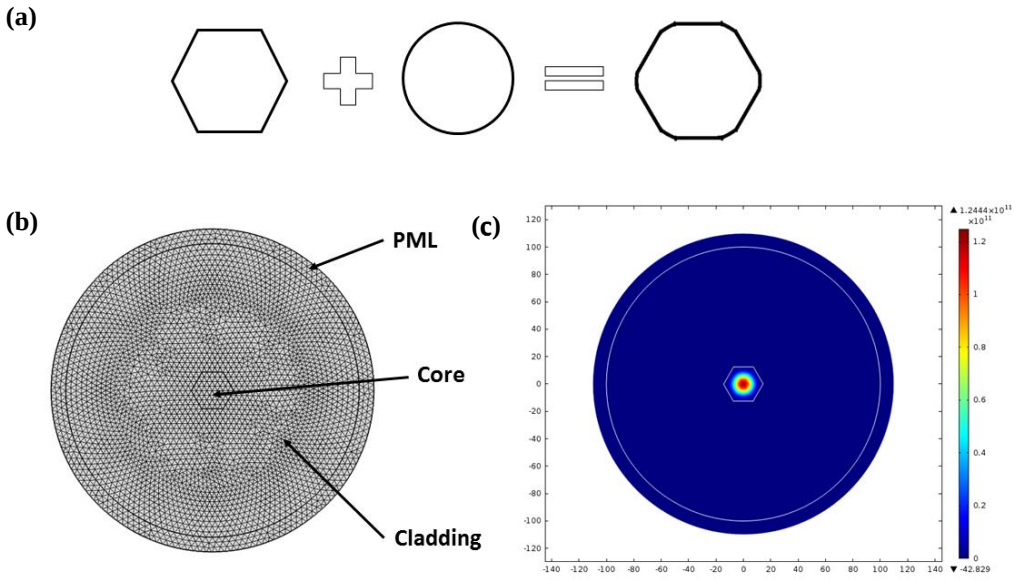

Figure 50. for a SC sapphire fiber, 2-D core structure of hexagonal, circle and transition between the two structures (A); 2-D finite element mesh for a hexagonal core with 25 µm inscribed diameter (B); fundamental mode energy pattern in the E filed for hexagonal core with 25 µm inscribed diameter(C).

SC sapphire fiber structure effect on confinement loss

The CL of a sapphire fiber as function of shape, transition from a circular fiber to a hexagonal fiber. To obtain the transition structure, the diameter of the circle was changed on a fixed inscribed diameter of the hexagonal. Fibers with different inscribed hexagonal diameter are divide into three groups: D25 (25 µm), D10 (10 µm) and D1 (1µm). Figures 51, 52, and 53 demonstrated the CL (y axis) verse effective index (x axis) on the three groups. The CL at the fundamental mode (n_f) for each group is listed in Table 3.

Table 3. Confinement Loss in the Fundamental Mode

Group / Type	D25		D10		D1	
	n_f	CL×10^{-7} (dB/km)	n_f	CL×10^{-5} (dB/km)	n_f	CL×10^{-1} (dB/km)
(A)	1.77193	9.05	1.77154	0.34	1.73079	0.37
(B)	1.77193	5.23	1.77156	1.46	1.73268	1.65
(C)	1.77193	8.67	1.77157	0.43	1.73350	1.39
(D)	1.77193	1.45	1.77157	2.81	1.73370	2.94
(E)	1.77193	4.83	1.77157	2.78	1.73385	3.36

The confinement loss of the fundamental mode in D25 is shown in Figure 44. All the fibers have the same fundamental effective index (1.77193) with CL in the same magnitude (10^{-7} (dB/km)).

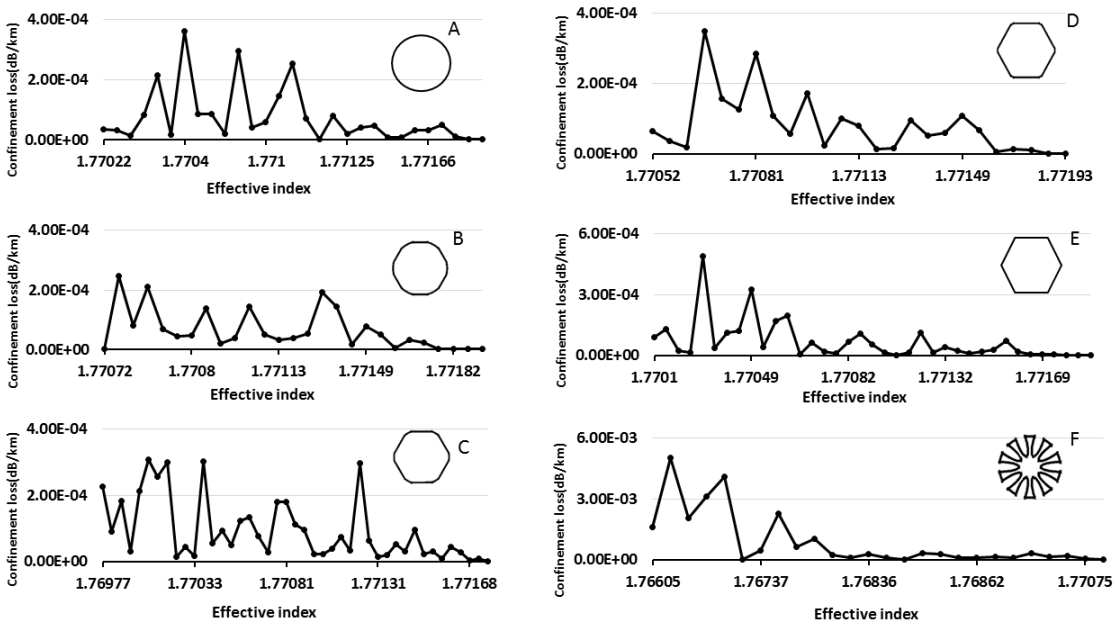

Figure 51. Confinement loss verse different effective index in D25 with 25 μm diameter(A); transition structure fibers with circle diameters of 26μm (B), 27 μm (C) and 28 μm (D); a hexagonal core SC sapphire fiber (E); a "star" core SC sapphire fiber (F); core structures are inserted)

The CL of the fundamental mode in D10 is shown in Figure 45. All the fibers have the similar fundamental effective index range from 1.77154 to 1.77157, and CL in the same magnitude (10^{-5} (dB/km)).

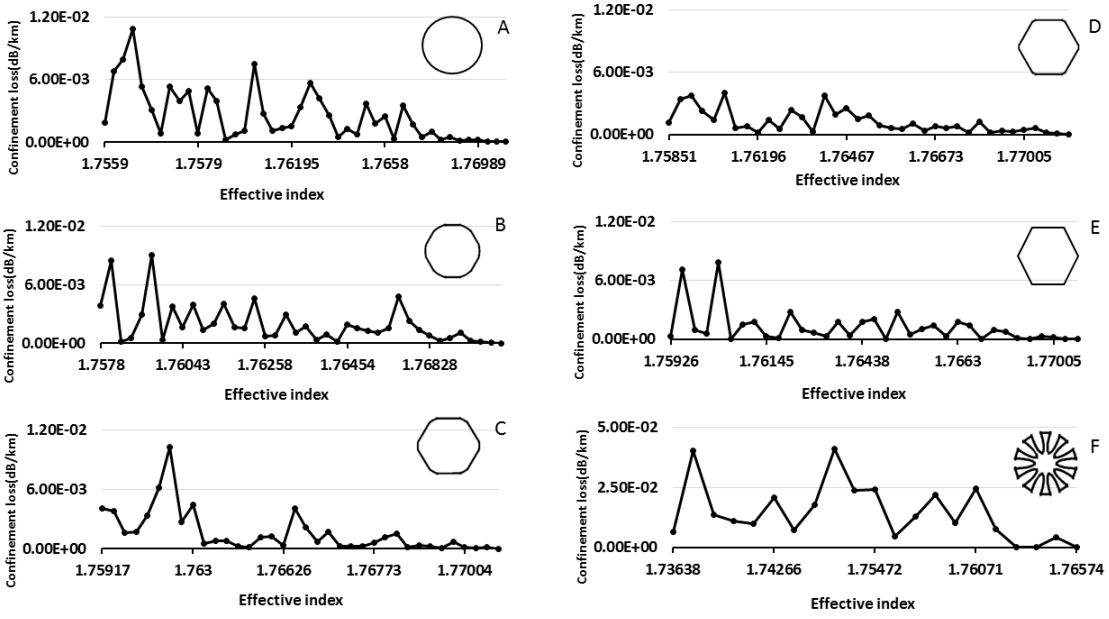

Figure 52. Confinement loss verse different effective index in D10 with 10 μm diameter(A); transition structure fibers with circle diameters of 10.5 μm (B), 10.8 μm (C) and 11 μm (D); a hexagonal core SC sapphire fiber (E); a "star" core SC sapphire fiber(F); core structures are inserted

Figure 46 shows the CL at fundamental mode in D1. All the fibers have the similar fundamental effective index range from 1.73079 to 1.73385, and CL in the same magnitude (10^{-1} (dB/km)).

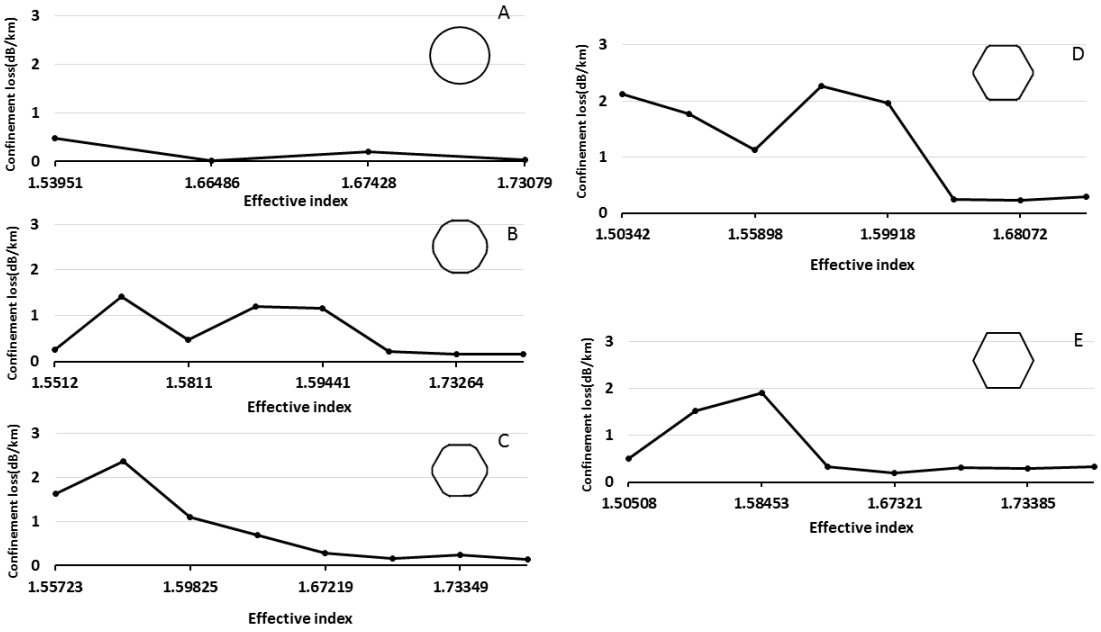

Figure 53. Confinement loss verse different effective index D1 with 1 μm diameter(A); transition structure fibers with circle diameters of 1.04 μm (B), 1.08μm (C) and 1.1 μm (D); a hexagonal core SC sapphire fiber (E); core structures are inserted.

Within each group, there is no significant difference in CL at fundamental mode between fibers due to the same magnitude. In addition, the CL increased with decreasing effective index value. When compared between groups, the CL increased significantly from 10^{-7} dB/km to 10^{-1} dB/km as the fiber's diameter decreased from 25 μm to 1 μm. Therefore, the higher order modes experienced a higher loss than the lower modes. Nonetheless, the shrinkage of fiber's diameter significantly increased CL in all the studied fibers. Since the V number decreased with decreased fiber diameter, a smaller number of modes will be supported in the core and the core has less confinement capability.

Mode reduction by single crystal sapphire "windmill" waveguide design

Considering the difficulty to control and fabricate a cladding on sapphire, another structure of SC sapphire fiber was studied. This new structure named as "windmill" fiber because it has air holes uniformly distributed along radial of the core. The proposed structure is similar to the "segmented-cladding" fiber design previously explored for the application of fused silica based optical fibers. [43,44]. This silica segmented-cladding fiber can maintain single-mode operation with a large core size via the effective index difference between the solid core and the average index of the two materials used in the segmented cladding. The windmill fiber with diameter d has ten ellipse holes with a-semi-axis (a) and b-semi-axis (b) and the center located and radially distributed on the core (Figure 54(a)). Figure 54(b) shows the variations of the core structure with a different a-semi-axis (μm) and b-semi-axis (μm) combination for a 5 μm diameter core.

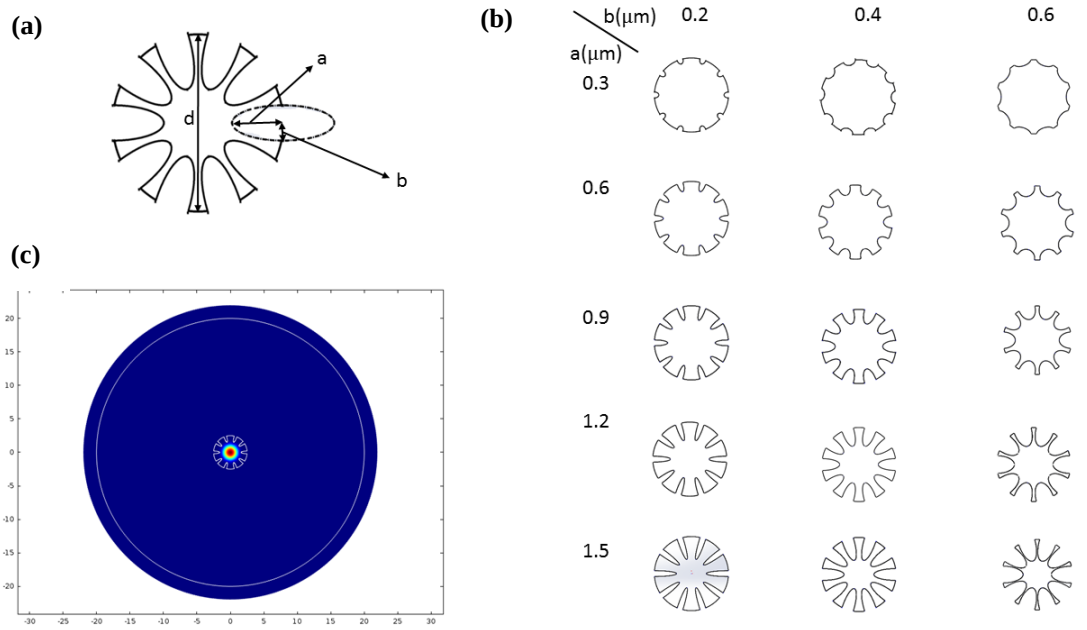

Figure 54. Structure of SC sapphire fiber with a windmill structure (A); "windmill" fiber (d=5μm) with different a-semiaxis and b-semiaxis parameters (B); fundamental mode energy pattern in the E field windmill fiber with d=5μm (C)

The influence of a-semi-axis and b-semi-axis on the guided modes for conventional and windmill fiber with diameter of 70 μm, 50 μm, 30 μm, 10 μm, 5 μm is shown in Figure 55. As expected in the conventional fiber, the guided modes in the fiber decrease with a corresponding decrease in diameter. For the "windmill" fiber, the number of guided modes were plotted with increasing a-semi-axis for three value of b-semi-axis. A comparison of the three sets of curves

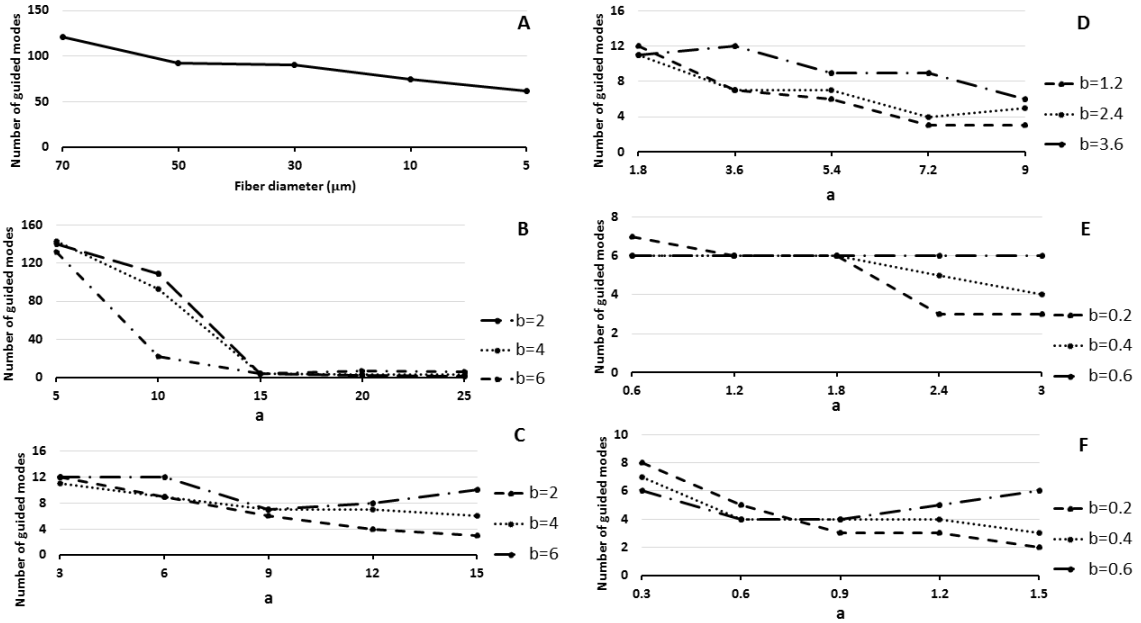

Figure 55. Number of guided mode in conventional fiber with reducing diameter (A); a "windmill" fiber with combination of a-semi-axis and b-semi-axis for 70 μm diameter (B); 50 μm diameter (C); 30 μm diameter (D); 10 μm diameter (E); 5 μm diameter (F).

for all five fibers shows that the number of guided modes for 70 μm, 50 μm, 30 μm, 10 μm, 5 μm conventional fibers are significantly reduced by the windmill structure with the highest a and lowest b combination. It is also observed that the a-semi-axis value has a significant influence on the number of modes in the windmill fiber at the studied wavelength. An as the a-semi-axis increased, the effective core size decreased and, therefore, reduced the guided modes. On the other hand, because the small b-semi-axis value, a decrease in the effective index difference between the core and cladding reduce the NA, which decrease the number of modes propagate in the fiber's core.

Structure parameters and CL in fundamental mode for a windmill fiber in each group is given in Table 4. All the studied fibers, exclude D1, are multimode. In addition, the relationship between the effective index, fiber's diameter and CL has the same tendency as conventional fiber. Compared with conventional fiber in each group, CL in the windmill fiber does not significantly increased. Thus, with a proper design, the modal volume of SC sapphire fiber could be reduced with acceptable confinement loss.

Table 4. Structure Parameters and CL of Fundamental Mode for "Windill" Fibers

Group	d(μm)	a-semiaxis (μm)	b-semiaxis (μm)	n_f	CL (dB/km)
D25	25	8	2	1.77151	1.77×10^{-5}
D10	10	3	1	1.76951	2.55×10^{-4}
D1	1	0.3	0.1	1.59684	0.94926

3.3.3 Theoretical Analysis of Windmill Fiber Designs for Single Mode Operation

The effective-single mode operation in a windmill SCSF can be achieved by evaluating the *a* and *b* parameters for different diameters, *d*, to induce high CL for the HOM and low CL for the FM. To evaluate the feasibility of single mode condition, it is reasonable to calculate the CL of the first two modes, since the CL of the modes increase with their mode order for the chosen fiber structure. A high difference between HOM and FM ensures effective single-mode operation in this windmill SCSF fiber. In reality, it is easier to fabricate a windmill SCSF with a small *a* and large *b* parameter. Thus, we designed and analyzed a windmill SCSF with optimized parameters for effective single-mode operation and anticipated to be more easily fabricated.

The effects of parameters a and b on the CL of FM (in solid line) and HOM (in dashed line) in the windmill SCSF with diameter of 70 μm (a), 50 μm (b) and 30 μm (c), are shown in Figure 56. As indicated in this figure, the CL of both modes decrease with *b*. This is due to fact that, at large *b* values, the core becomes more circular in shape and reduces the confinement loss of individual modes. With an increasing *a* value, the effective core diameter *d.* shrinks and the cladding region is increases, which reduces the CL of the studied modes, for most cases.

At a wavelength of 0.532 μm, the optimized parameters for the windmill SCSF with diameter of 70 μm were deduced to be *a*= 28 μm and *b*=6 μm. Compared with the CL, 0.11 dB/m, of the FM,

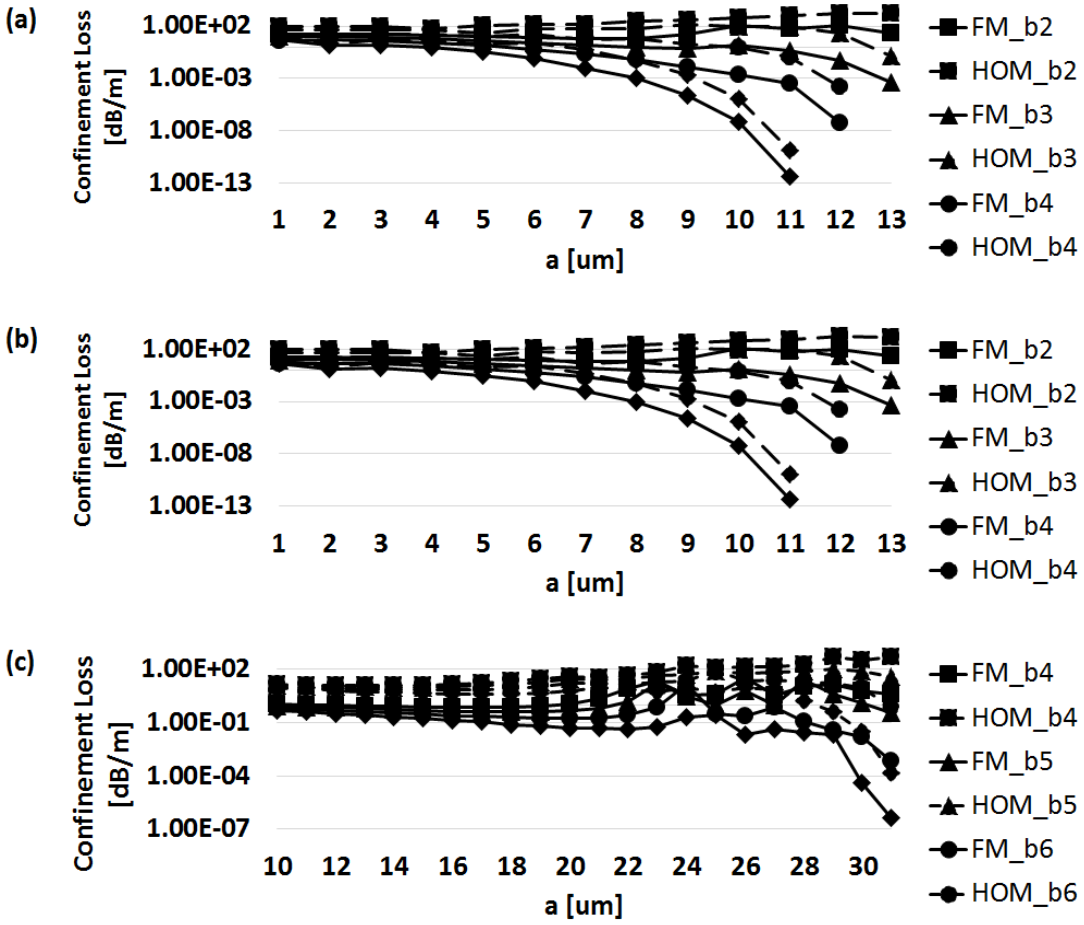

Figure 56. Variation of confinement loss of the FM (solid line) and HOM (dash line) as a function of the parameter a and b for a SCSF with diameter of (a) 70 μm; (b) 50 μm; (c) 30 μm.

the CL of HOM is found to be significantly higher, at 19.19 dB/m. Therefore, a 1.04 meter long waveguide can strip off all the high order modes and ensure the single mode operation in windmill SCSF. The optimum parameters for a 50 μm diameter windmill SCSF at 0.532 μm are a=18 μm and b=5 μm, with the CL of FM at 0.27 dB/m and HOM at 17 dB/m. The optimum parameters for a 30 μm diameter windmill SCSF at 0.532 μm are a=11 μm and b=3 μm, with the CL of FM at 0.4dB/m and HOM at 97dB/m. A 1.18 meter long with 50μm diameter and a 0.2 meter long with 30 μm diameter windmill SCSF can strip off all the high order modes and ensure the single mode operation under the wavelength of 0.532 μm.

Electric field distribution of FM and HOM in the "windmill" sapphire fiber

The electric field contour plot of the optimized windmill SCSF, with studied diameters at an operating wavelength of 0.532 μm, are shown in Figure 57; the FM is on the top and the HOM on the bottom. As shown in the figure, the FM of the fibers are well confined in the core region while the great extension pattern in the cladding region of HOM indicate their leaky behavior. The large leakage losses of the HOM in the studied fibers are reflected by this electric field contour plots.

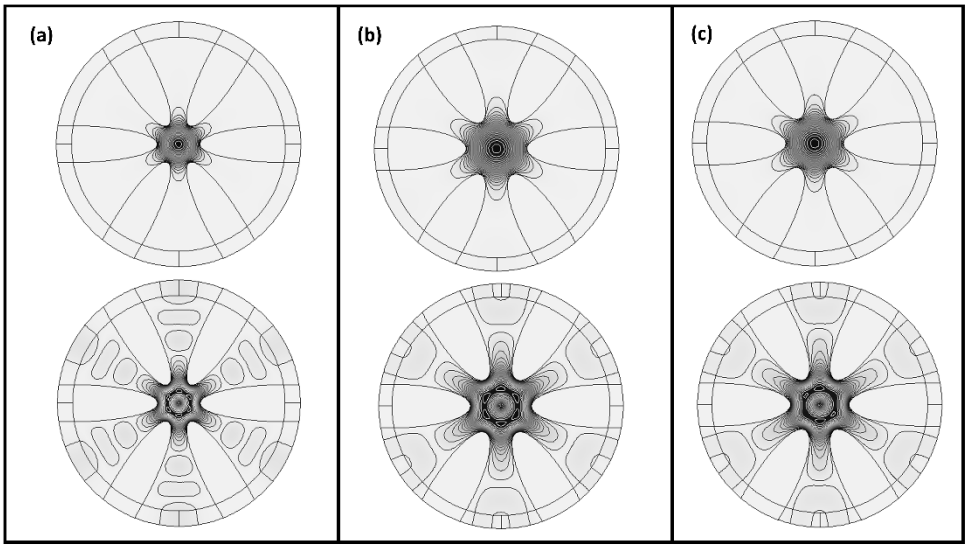

Figure 57. Electric field contour plot of the optimized windmill SCSF on FM (top) and HOM (bottom) with diameter of (a) 70 µm; (b) 50 µm; (c) 30µm.

Confinement loss as a function of wavelength

The spectral dependence of the confinement loss was simulated over a wavelength regime, extending from 0.4 µm to 2 µm. Electric field distributions of the studied windmill SCSF at 0.4 µm and 2 µm, with the optimized *a* and *b* parameters, are shown in Figure 58, Figure 59 and Figure 60. The black and white line contour plots are the electric field intensity distributions.

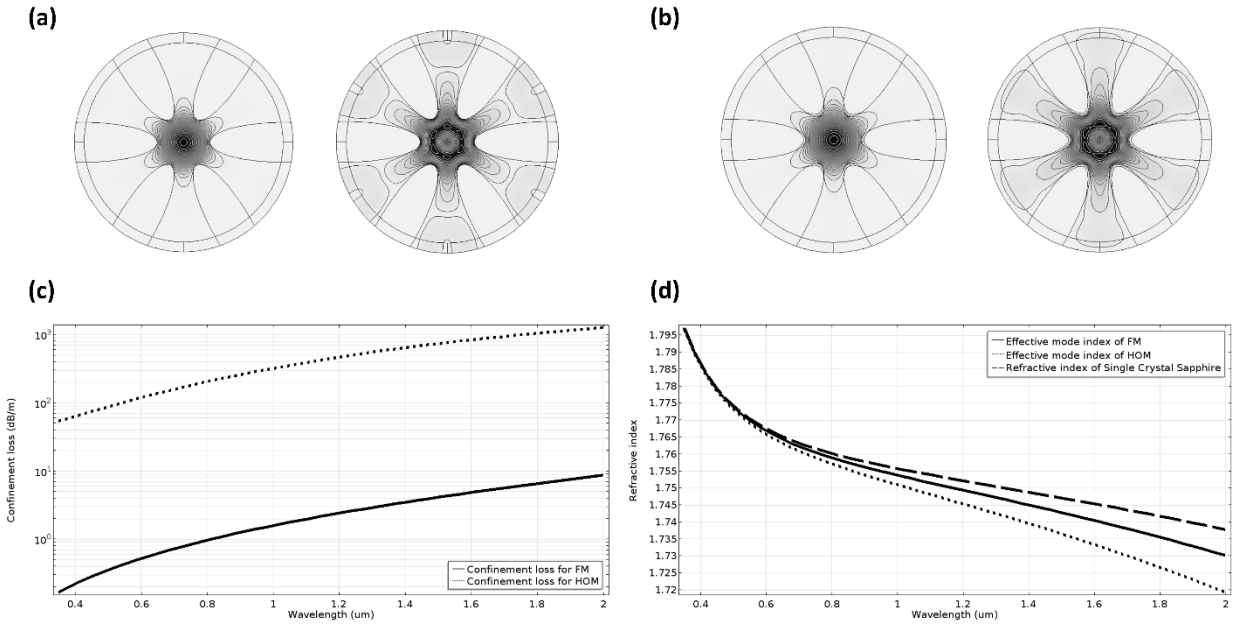

Figure 58. Windmill SCSF with 30 µm diameter (a) electric field distribution at a wavelength of 0.4 µm; (b) electric field distribution at a wavelength of 2 µm; (c) confinement loss as a function of wavelength; (d) refractive index as a function of wavelength.

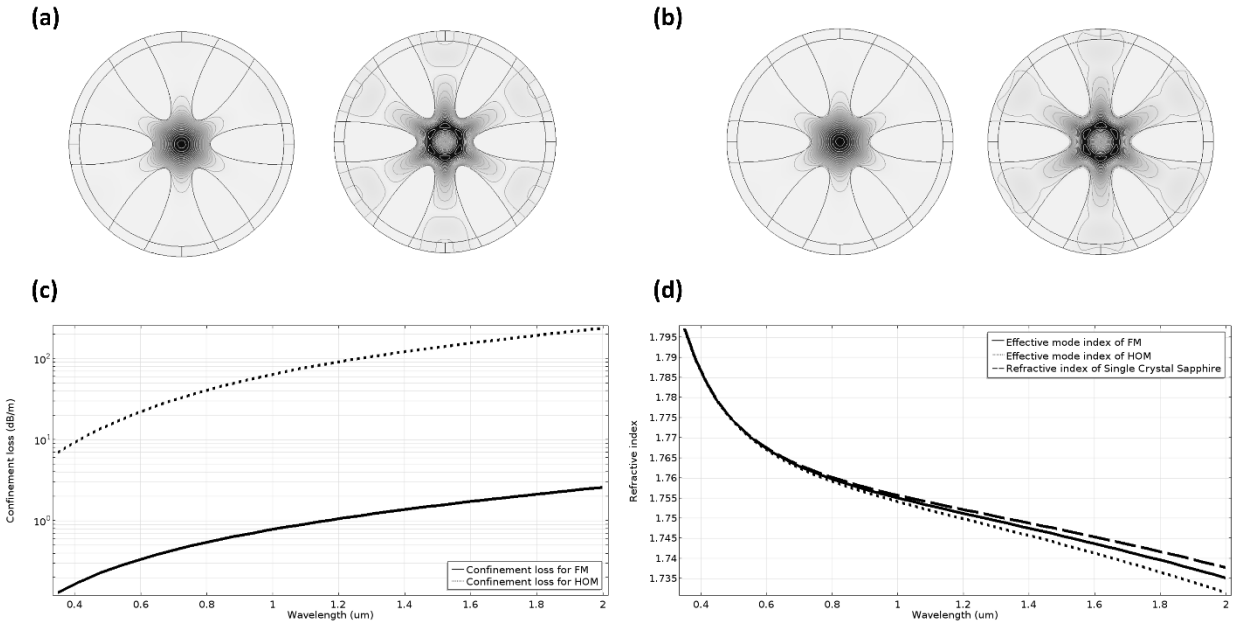

Figure 59. Windmill SCSF with 50 µm diameter (a) electric field distribution at a wavelength of 0.4 µm; (b) electric field distribution at a wavelength of 2 µm; (c) confinement loss as a function of wavelength; (d) refractive index as a function of wavelength.

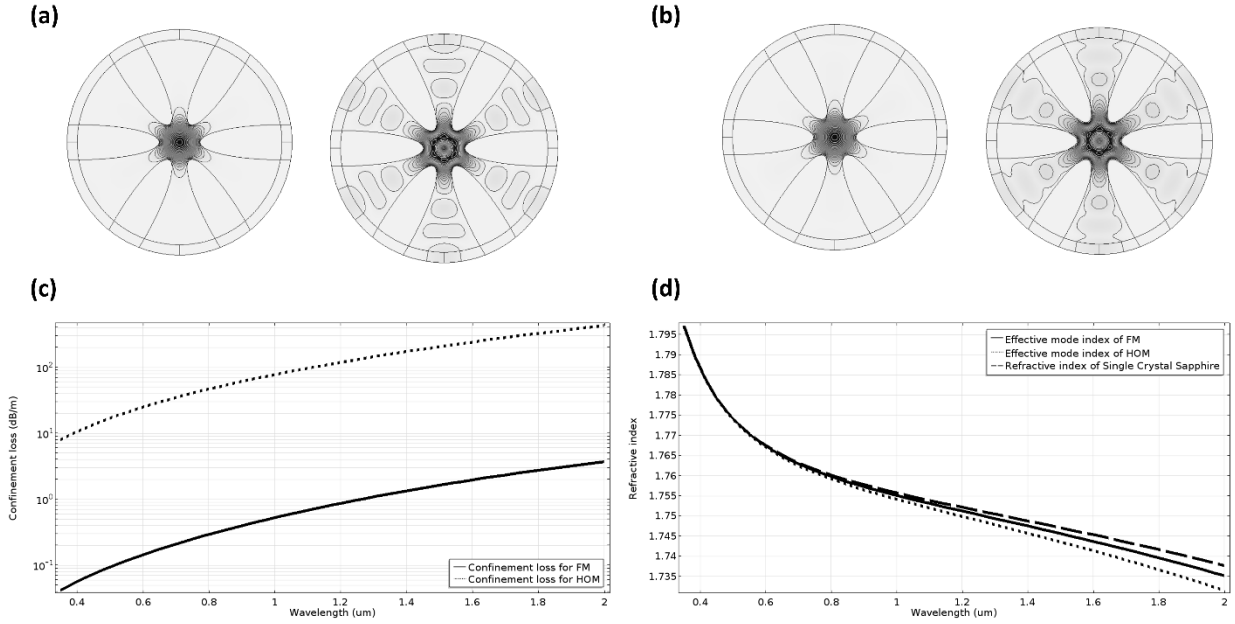

Figure 60. Windmill SCSF with 70 µm diameter (a) electric field distribution at a wavelength of 0.4 µm; (b) electric field distribution at a wavelength of 2 µm; (c) confinement loss as a function of wavelength; (d) refractive index as a function of wavelength.

The electric field of FM is mostly confined in the effective core region with a small portion that extends into the cladding region. On the other hand, the HOM has a much-dispersed pattern, and a large portion of the electric field is distributed into the cladding region. It is clearly demonstrated that at shorter wavelengths, the modal fields are more confined in the effective core region,

contrary to what occurs at the longer wavelengths. Simulations performed at the intermediate wavelengths confirm that for longer wavelengths, the modal field tends to extend into the cladding region.

Furthermore, as shown in the figures, the CL of FM (solid line) and HOM (dashed line) both increase with wavelength due to more spread of the modal fields in the windmill cladding. In addition, the profiles in Figure 58, Figure 59, and Figure 60 also indicate the CL of FM is more than two orders of magnitude lower than that of HOM. This large differential CL between the modes ensure the effective single-mode operation by leaking out the HOM quickly.

The design and analysis of a "windmill" shaped single crystal sapphire fiber with large-core and single-mode operation in the spectral range from 0.4 to 2 μm was first reported in this project. This design provides some unique advantages in terms of mode confinement compared to all other commercially available single crystal sapphire fibers. The fiber design analyzed by FEM simulations demonstrated a significant difference in the CL between the first two modes, which ensured single-mode operation. The high leakage losses of the HOM in the studied fibers were reflected in their distribution in the electric field contour plots. The large-core single-mode "windmill" SCSF is easy to handle and install compared with conventional single-mode SCSF, which has a core diameter of 500 nm. Since more light is transmitted within a large-core fiber, sapphire fiber with such a large-core would be useful in high power applications. These advantages render this class of single-mode and large-core SCSF of interest for future applications. This basic fiber design will improve the performance of many SCSF fiber sensors including Fabry–Perot single-point sensors and Raman scattering-based temperature sensing systems.

3.3.4 "Bundled-Windmill" Fiber Design

A variant of the "windmill" fiber structure, referred to as the bundle cladding "windmill" structure, was also proposed in attempt to address the considerable challenges related to the fabrication of the LMV fiber designs. A 2D image of a bundle cladding "windmill" fiber structure is shown in Figure 61. The six red dashed boxes indicate the equivalent elliptical holes in "windmill" structure; D is the bundle fiber diameter, D1 is the core diameter and D2 is stacking fiber's diameter

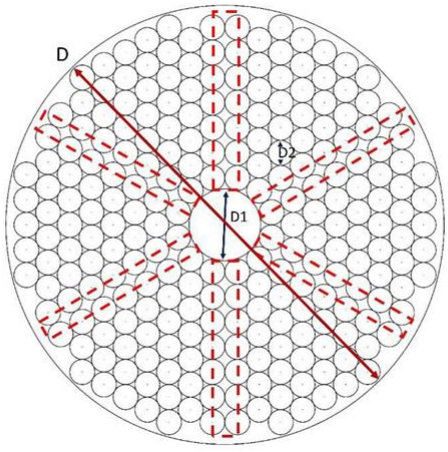

Figure 61. 2D structure of a bundle cladding "windmill" fiber structure

The design parameters were bound by the smallest sapphire fiber made to date. Waveguide simulations of the bundle cladding "windmill" sapphire were performed with COMSOL version 5.1. A bundle cladding "windmill" sapphire fiber structure with three cladding layers, as well as the associated parameters and COMSOL settings are shown in Figure 62. The areas shaded in blue and gray color are air and sapphire, respectively. The simulation was performed at a wavelength of 532

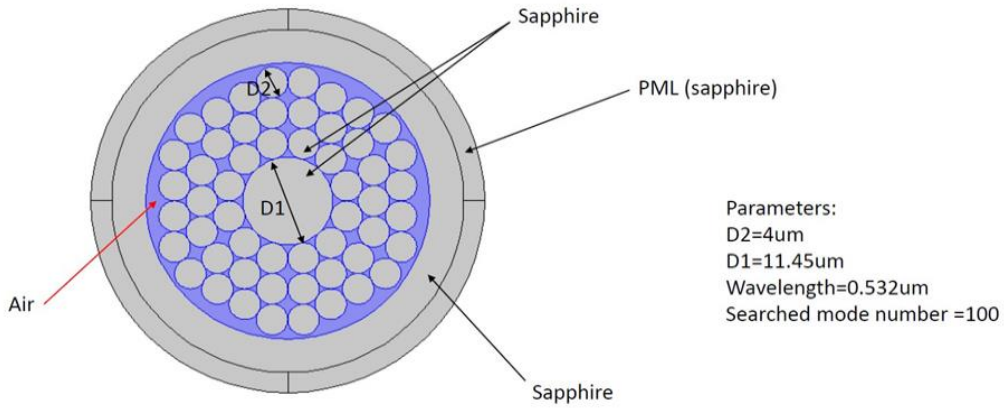

Figure 62. Three layers bundle "windmill" sapphire fiber in COMSOL.

nm, with D1=11.45μm and D2=4μm, with a search of 100 modes near refractive index of sapphire (1.7717). All the parameters are invariant, except the number of cladding layers. Electric field distributions of the fundamental mode of bundle cladding "windmill" sapphire fibers with different stacking layers are shown in Figure 63.

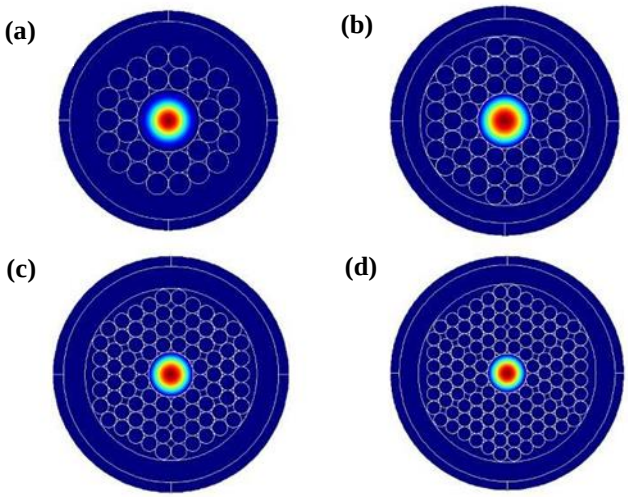

Figure 63. Electric filed distribution (fundamental mode) of bundle cladding "windmill" sapphire fiber with (a) two layers; (b) three layers; (c) four layers; (d) five layers

As shown in Figure 64, the first seven modes in the simulated structures can be divided into four categories: the fundamental mode, high order modes, cladding modes and loss modes. After searching for 100 modes in the simulation, only four high order modes propagate in the novel

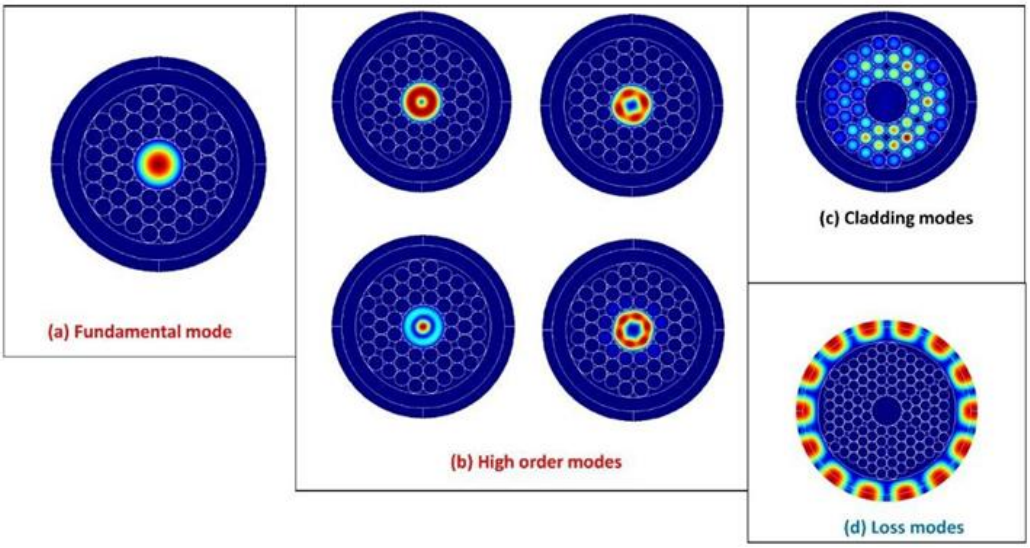

Figure 64. Electric field distribution of the three-layer bundle cladding "windmill" sapphire fiber on (a) fundamental mode; (b) high order modes; (c) cladding modes and (d) loss modes.

waveguide structure in addition to the fundamental mode. Therefore, the bundle cladding "windmill" sapphire fiber was shown to significantly reduce the number of guided modes. Furthermore, the fabrication of this simple fiber design does not require complicated masking and etching processes.

As shown in Figure 65, the confinement loss of the fundamental mode was predicted to be as low as 10-12 dB/m, which is indicative of a structure with good confinement capability. Based on these results, the new designed bundle cladding "windmill" sapphire fiber is a feasible alternative to the more traditional "windmill" sapphire, which is known to have several process challenges.

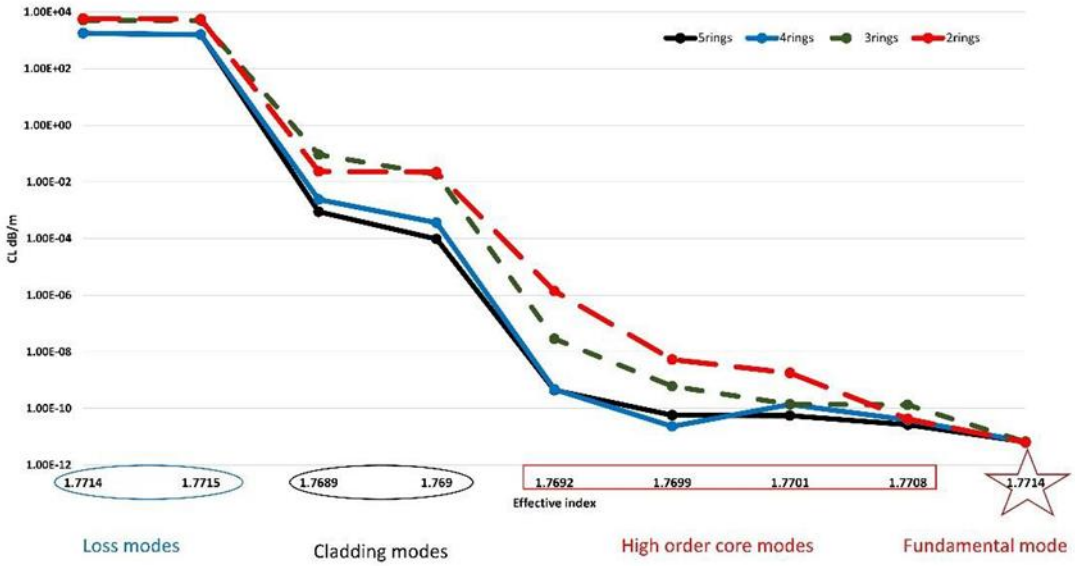

Figure 65. Confinement loss in bundle cladding "windmill" sapphire fiber with different stacking layers

4 DISTRIBUTED TEMPERATURE SENSING SYSTEM

4.1 Theoretical Analysis of Raman Scattering in Single Crystal Sapphire

4.1.1 Raman Scattering Phenomena in Sapphire

According to the system scheme, the acquired instantaneous intensity of the Raman signal will be related not only to the temperature, but also to the position of the measurement. The further the sensing fiber is from the light source, the higher the loss will be during the pump and signal propagation. In this calculation, the Raman Stokes and anti-Stokes light intensity from the section at the far end of a 1 m sapphire fiber was estimated.

The returned Raman scattering power from this section can be calculated as [58]:

$$P_{AS} = 0.5 \cdot P_0 \Delta t \cdot v \cdot \alpha_{AS}[T(x)] \cdot S \cdot 10^{-\{[\alpha(\lambda_0)+\alpha(\lambda_{AS})]\cdot X+\alpha(sys)\}/10} \quad (31)$$

where $P_0\Delta t$ is the pulse energy, v is the light speed in the fiber, α[T(x)] is the Raman scattering loss coefficient at position x with temperature T, and S is the capture fraction. $\alpha(\lambda_0)$, $\alpha(\lambda_{AS})$ and $\alpha(sys)$ are the attenuation of the pump laser, attenuation of the Raman signal and the system loss, respectively. All the losses are in units of dB.

The capture fraction S depends on the numerical aperture of the fiber, angular distribution of the scattered light, and the distribution of scattering cross-section across the fiber core. It is reported to be ~5×10^{-3} for a 0.2-NA fiber, and 10^{-2} for a 0.29-NA fiber [59, 60]. The anti-Stokes scattering loss coefficient α_{AS}[T(x)] depends on the temperature at local position, and is proportional to the differential cross section which is defined as,

$$\left.\frac{d\sigma_{AS}}{d\Omega}\right|_x \cong \frac{1}{\lambda_{AS}^{\,4}} \frac{1}{\exp\left[\dfrac{hc\Delta\upsilon}{K_B T(x)}\right]-1}, \quad (32)$$

where ω_{AS} is the Anti-Stoke's wavenumber, h is Planck's constant, c is the velocity of light in vacuum, k_B is Boltzman's constant, and Δv is Raman shift. Similarly, the differential cross section of the Stokes component is defined as,

$$\left.\frac{d\sigma_{S}}{d\Omega}\right|_x \cong \frac{1}{\lambda_{S}^{\,4}} \frac{1}{1-\exp\left[-\dfrac{hc\Delta\upsilon}{K_B T(x)}\right]}, \quad (33)$$

According to these definitions, the differential cross section increases as temperature rises. For example, the differential cross section of the anti-Stokes component increases by 11.9 times when the temperature rises from 25ºC to 1100ºC, and 15.1 times at 1400ºC. Comparatively, the differential cross section of the Stoke component increase 2.4 times at 1100ºC compared with 25ºC, and 2.8 times at 1400ºC. As a reference, a standard silica 50/125 μm graded index multimode fiber has a α_{AS} value of ~6 x 10^{-7}/m at room temperature [60,61].

α-Al_2O_3 sapphire crystals have a D_{3d}^6 symmetry, which means they have Raman-active phonon modes: $2A_{1g} + 5E_g$ [18], where A_{1g} corresponds to the Raman shifts at 418 and 646 cm^{-1}, and the E_g corresponds to shifts at 380, 432, 451, 578, and 751 cm^{-1}. According to the Raman spectrum reported by G.H. Watson, the strongest Raman peaks are at 418 cm^{-1}, 578 cm^{-1} and 751 cm^{-1} and 751 cm^{-1} [62]. As for the 355 nm and 532 nm lasers, which were candidate pump light wavelengths for the proposed sensing system, the corresponding Stokes and anti-Stokes components are summarized in Table 5. This data guided the selection of the corresponding Stokes and anti-Stokes filters for the sensing system.

Table 5. Strongest Raman Peak Positions for Sapphire Fiber

Raman shift (cm^{-1}) / Raman wavelength (nm)		418	578	751
Laser line 355 nm	***Stokes***	360.3	362.4	364.7
	Anti-Stokes	349.8	347.9	345.8
Laser line 532 nm	***Stokes***	544.1	548.9	554.1
	Anti-Stokes	520.4	516.1	511.5

4.1.2 Impact of Black Body Radiation on Raman Scattering Signal

One of the major technical challenges to overcome for the development a distributed Raman backscatter sensing system for operation at elevated temperatures (>1000°C) is the effect of high temperature blackbody radiation on the signal to noise ratio (SNR). To assure adequate performance, the thermal background intensity at high temperature was compared with the Stokes and anti-Stokes scattering light intensity through calculation as a rough estimation of the signal to background ratio.

Blackbody radiation is a special emission that is independent to all physical material properties and is intrinsic to all materials. According to Planck's law the radiation can be calculated per the following

$$B(T) = \frac{2hc^2}{\lambda^5} \frac{1}{e^{\frac{hc}{\lambda k_B T}} - 1} \tag{34}$$

where k_B is the Boltzmann constant, λ is the wavelength, h is the Planck constant and c is the speed of light in vacuum.

The calculated blackbody radiation power spectra in UV and visible range according to (34) is shown in Figure 66. The intensity of the thermal emission at 532 nm is ~26 dB higher than at 355 nm at a temperature of 1400°C, and the difference increases to ~34 dB with a decrease in temperature to 1100°C. As a result, using 355nm as the Raman pump light could greatly suppress the background signal from blackbody radiation comparing to 532 nm pump at high temperatures.

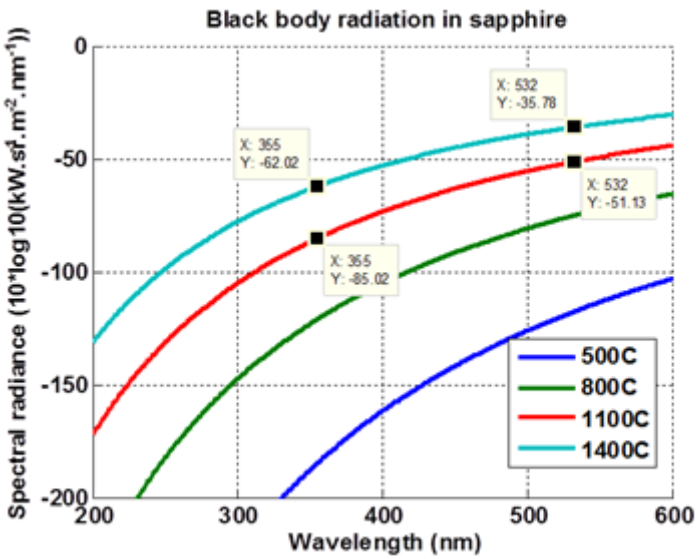

Figure 66. Blackbody radiation intensity in UV-VIS range.

However, there are some drawbacks that will reduce the system SNR when using 355 nm laser. First, the loss of the sapphire fiber is higher for UV light comparing to visible light (as described previously), which will reduce the signal level for sensing sections further from the light source. Second, high speed photodetectors have much lower quantum efficiency in the UV region than in the visible. As a result, in order to acquire the best signal quality, the wavelength of the light source was chosen carefully by considering and balancing all the these factors.

A simple model was developed to roughly estimate the intensity level of blackbody radiation in a heated sapphire fiber. As shown in Figure 67, the fiber was divided into finite segments, and part of the emission from each segment was coupled in to the fiber. The coupling ratio was estimated by calculating the covered solid angle through the numerical aperture of the fiber (Figure 68). The total output intensity was calculated by integrating the contribution of all these segments.

Figure 67. Thermal emission in sapphire fiber.

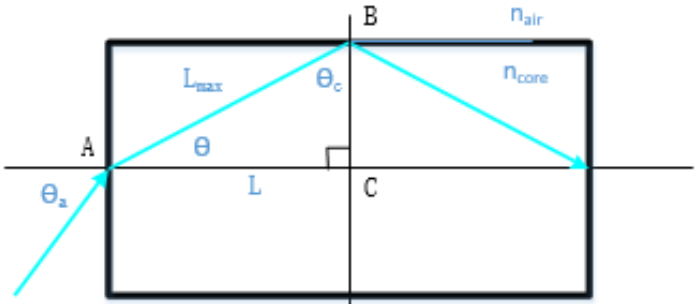

Figure 68. Total reflection in sapphire fiber.

With this model, a simplified estimation of the radiated intensity from one fiber end can be written as:

$$P = B \cdot \Omega \cdot S \cdot \Delta\lambda \cdot n \quad , \tag{36}$$

where *P* is the total radiated power from one fiber end, *B* is the blackbody spectral radiance, *Ω* is the solid angle accepted by the fiber, *S* is the area of the fiber cross section, *Δλ* is the wavelength range, and n is the number of segments.

From the definition of solid angle and Snell's law, we can obtain

$$\Omega = \frac{\pi r^2}{L^2} = \frac{\pi r^2}{\left({}^{r}/_{\tan\theta}\right)^2} = \pi \tan^2\theta \tag{37}$$

$$n_{core} \sin\theta = n_{air} \sin\theta = NA \tag{38}$$

where r is the radius of the fiber core, θα is accept angle, and θ is diffractive angle.

Taking the attenuation of the sapphire fiber into consideration, the received thermal radiation power is defined as,

$$P = B \cdot \left[\pi r \cdot \tan\left[\arcsin\frac{NA}{n_{core}}\right]\right]^2 \cdot \Delta\lambda \cdot \int_{1/n}^{1} 10^{-x\cdot\alpha(\lambda_{AS})/10}\, dx \tag{39}$$

Considering the 8 dB system loss calculated in Equation 16 the calculated transmitted power of the blackbody radiation is 2.4×10^{-8} W at 1100°C, and 2.4×10^{-7} W at 1400°C when using a 10nm band pass filter at 532nm. The background can be further suppressed by using narrower filters.

The following parameters are used in the numerical calculation: 110 μJ laser pulse energy, 532nm laser wavelength, and a refractive index of 1.774 for sapphire fibers. The calculated results of the signal power of blackbody radiation and Raman scattering are shown in Table 6.

Table 6. Calculated Blackbody Radiation and Raman Signal Power

Wavelength (nm):	**532**			**355**		
Temperature (°C)	*25*	*1100*	*1400*	*25*	*1100*	*1400*
Blackbody radiation (10^{-7} W)	-	0.24	0.82	-	0.00009	0.018
Anti-Stokes Power (10^{-7} W)	1.1	13.0	17.0	0.8	9.4	12.0
Stokes Power (10^{-7} W)	6.6	16.0	19.0	4.8	12.0	14.0

It is known that the Raman scattering is weaker in sapphire fibers than in silica fibers [63]. However, given the estimation result, both Stokes and anti-Stokes signals are relatively strong compared to the blackbody radiation background. Thus, the values in sapphire fiber must be determine experimentally.

4.2 Characterization of Sapphire Fiber for Distributed Temperature Sensing

4.2.1 Temperature Dependence of Raman Scattering in Sapphire Fiber

Raman scattering has long been recognized as a method of distributed temperature sensing with the use of fused silica graded-index multimode fibers. Although the use of single crystal sapphire fibers in sensing systems have become increasingly more prevalent in the most-harsh environment applications, distributed Raman backscatter-based sensing capabilities have been allusive. The temperature dependence of frequency, width and pressure dependence of Raman active modes in bulk sapphire have been reported, but not in optical fibers. When the sapphire fiber is contaminated, the temperature sensing technique which relies only on Raman Stokes peaks makes it difficult to extract the intensity change due to fiber loss and, more significantly, the Stokes peaks are less sensitive than the Anti-Stokes peaks. Few have reported the Raman Anti-Stokes peaks because of the requirement for a very high laser power to observe and such power energy is very close to the damage threshold of the sapphire fiber. The Anti-Stokes component of a sapphire fiber was observed in this project for the first time, as well as its temperature dependence on Raman scattering intensity, frequency and width.

The setup for the experiment is depicted in Figure 69. The light source is a Nd:YAG laser (Continuum, SLIII-10) at 532 nm. The laser pulse repetition rate was 10Hz with a pulse energy of about 500 μJ and a pulse width (FWHM) of 24 ns. It is well known that 1 in 10^8 photons is

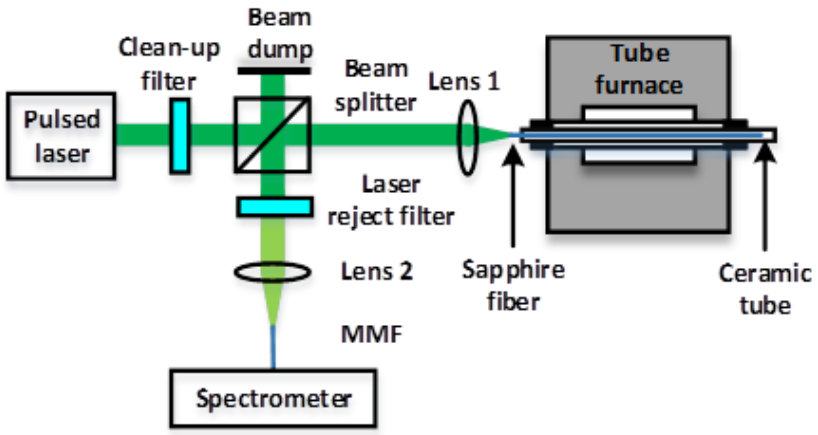

Figure 69. Schematic of the experimental setup for Raman scattering detection.

scattered by the Raman scattering; such weak scattering will be easily masked by blackbody radiation background. A shorter wavelength laser could efficiently avoid the blackbody radiation background, which is inversely proportional to the fifth power of the wavelength. Strong fluorescence absorption at 694.3 nm in sapphire fiber was also found due to the impurity of Cr^{3+} iron with a broad background when the laser light is intense. Laser wavelength at 532 nm avoided the strong background from thermal radiation as well as most of the fluorescence. The beam first passed through a laser clean-up filter centered at 532 nm. The beam was then coupled into the sapphire fiber using a concave lens. The sapphire fiber was protected in a ceramic tube (with ID 1.6 mm and OD 6.75 mm) which went through a furnace. A thermocouple was located beside the ceramic tube to monitor the temperature distribution along the fiber. The backward scattering light was reflected by the beam splitter, passed through a laser reject filter at the center

wavelength (532 nm), and was last coupled into a 105 μm core multi-mode fiber and detected with a spectrometer (Ocean Optics, USB4000). The sapphire fiber is 0.72 m long, 75 μm in diameter and was grown by the laser heated pedestal growth method. A dark spectrum was immediately measured before the Raman spectrum by blocking the light into the spectrometer, which was later subtracted from the Raman spectrum measurement.

The sapphire fiber's temperature distribution is shown in Figure 70. The sapphire fiber was heated at a rate of 10 ºC/min, and the temperature was kept constant during the measurements

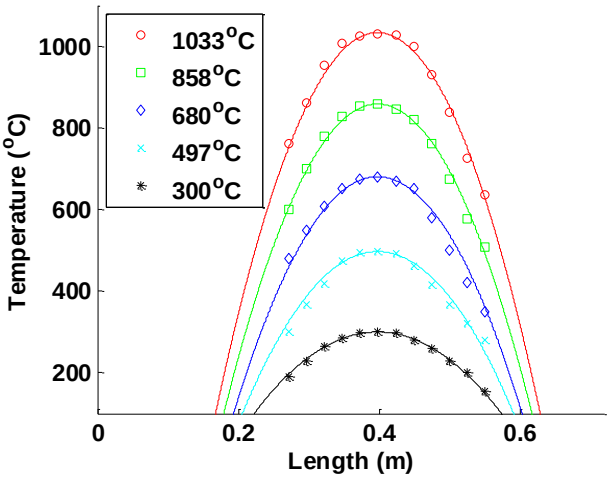

Figure 70. Measurement result of temperature distribution along the fiber.

within ±1ºC. Each measurement was taken after a given temperature was maintained for 30 min. The temperature profile showed a 10 cm long plateau corresponding to the center of the furnace and dropped quickly from its center. When the fiber's segment was at the outside the furnace, the temperature dropped rapidly to room temperature.

Sapphire crystal belongs to space group D_{3d}^6 and has irreducible representation for the optical modes of $\Gamma = 2A_{1g} + 2A_{1u} + 3A_{2g} + 2A_{2u} + 5E_g + 4E_u$ [62, 63]. Only two A_{1g} and five E_g modes are Raman active and therefore seven phonon modes are expected in Raman spectrum of sapphire with peaks located at 379, 418, 431, 450, 578, 645 and 750cm^{-1}.

We detected 418, 578 and 750 cm^{-1} peaks, as shown in Figure 71. Thirty accumulations, each with an integration time 10 seconds were averaged in each plot and high frequency noise was filtered. At room temperature, only one Anti-Stokes peak (418 cm^{-1}) was visible. When the temperature increased to 300ºC, two Anti-Stokes peaks (418 and 750 cm^{-1}) were identified. At temperature higher than 500ºC, the intensity of the third peak at 578 cm^{-1} became comparable with the other two peaks. As expected, the Anti-Stokes peak position and Stokes peak position were symmetric..

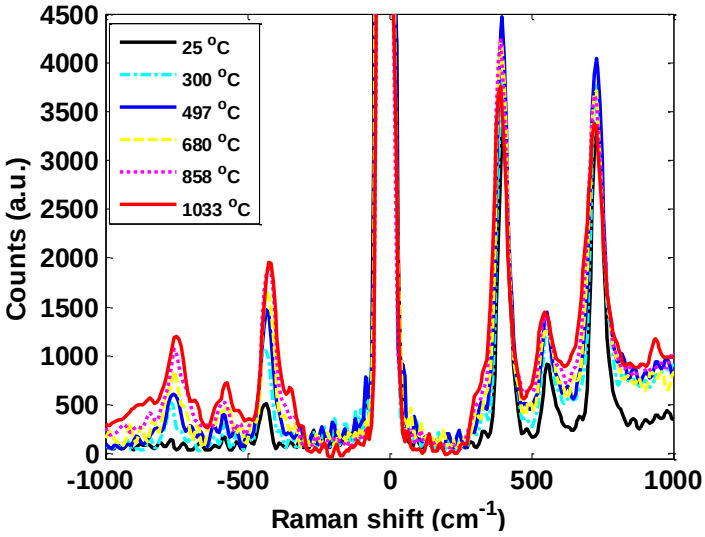

Figure 71. Raman spectrum of sapphire fiber at different temperature.

To better predict the peak amplitude, position and width on each spectrum, a Lorentz fitting technique was applied to each peak to represent the original peak. The thermal radiation background was recorded by simply turning off the laser. The thermal radiation background was later subtracted in the following figures. Figure 72 shows the temperature dependence of Raman

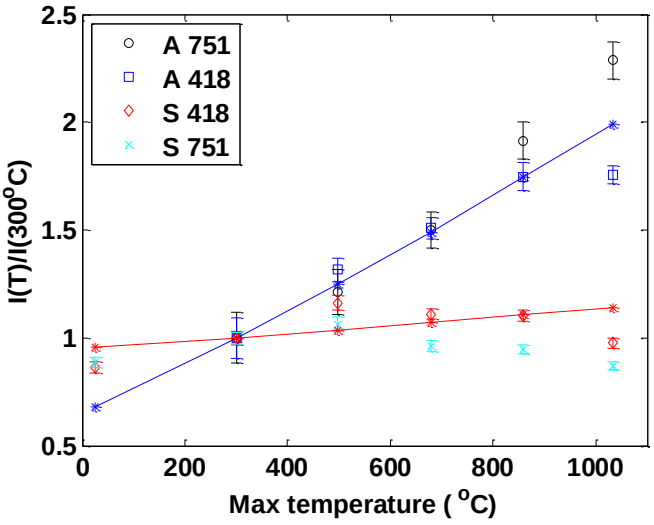

Figure 72. Temperature dependence of sapphire Raman intensity. Solid curve shows the theoretical predictions on Anti-Stokes 418cm^{-1} (blue) and Stokes 418 cm^{-1} (red) indicated by Eq. 4.

components intensity after removing the thermal background. The intensity of Anti-Stokes peak 751 cm^{-1} at room temperature was set as zero because this peak was not visible yet. With increasing temperature, the intensity of Anti-Stokes peaks increased almost linearly.

Taking into account the fiber loss and laser power depletion, the Raman power received by the spectrometer is proportional to integration differential cross section along the fiber as,

$$P_{AS} = \int_0^L \left. \frac{d\sigma_{AS}}{d\Omega} \right|_x \exp\left[-2\int_0^x \alpha(\mathrm{x})\,\mathrm{dx} \right] dx, \tag{40}$$

$$P_S = \int_0^L \left. \frac{d\sigma_S}{d\Omega} \right|_x \exp\left[-2\int_0^x \alpha(\mathrm{x})\,\mathrm{dx} \right] dx, \tag{41}$$

where L is the sapphire fiber's length, and α is the attenuation of the fiber at locale position x. It was noted that the Stokes peaks were the combination of Raman scattering and a small fluorescence background. Because a strong fluorescence background is observed at center 694.3 nm with the broad side lobe extended to the Stokes peak region and reached its maximum at 500 ºC. At higher temperature, the intensity of the fluorescence peak and its side lobe became weaker. Since the Anti-Stokes peaks were at shorter wavelength compared with the Stokes peaks wavelength, the Anti-Stokes were less affected by the fluorescence background.

The temperature dependence of Raman shift of both the Anti-Stokes and the Stokes peaks were observed for the first time, as shown in Figure 73(a). The Stokes peaks had less standard deviation because the peaks are stronger than Anti-Stokes and had a higher signal to noise ratio. The shift of the Stokes and Anti-Stokes peaks tended to be symmetric which was predicted by the phase matching condition of Raman scattering. The frequency change was normalized to the frequency shift at room temperature.

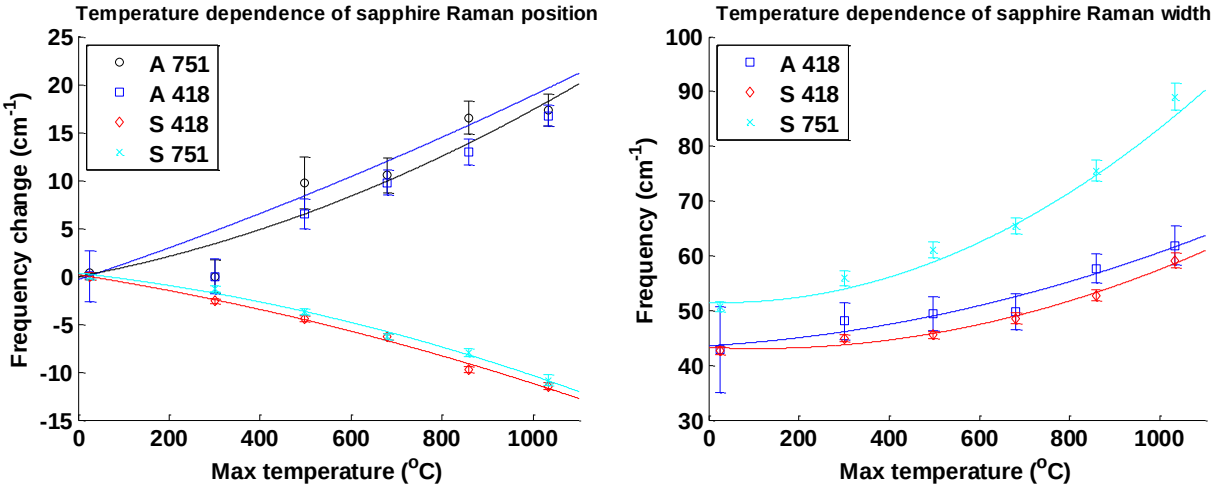

Figure 73. Temperature dependence of (a) the sapphire Raman frequency and (b) peak width.

It is noted that since the spectrometer has a lower bandwidth, the Raman peak width is broadened compared with other's measurement results [64]. Raman linewidth expansion was also observed in this experiment. Klemens and M. Ashkin tried to explain this by the perturbation theory [64]. Although our results were similar, as shown in Figure 73 (b), an additional explanation takes all of the fiber's temperature profile into consideration. Since part of the sapphire fiber was at low temperature and part was at high temperature, one side of peak remained un-shifted while the other side shifted; it is likely that part of Raman linewidth

expansion is due to the combination of all Raman line shifts along the sapphire fiber at different temperatures.

The observation of the Anti-Stokes peaks in sapphire fiber for the first time laid the foundation for the development of the distributed temperature sensing system. Temperature dependence of the sapphire Raman line intensity, frequency shift and linewidth were experimentally measured. These experiments demonstrated that the Anti-Stokes components of sapphire fiber was more sensitive to temperature compared with Stokes components and the intensity becomes comparable to the Stokes components at higher temperature. The feasibility of the approach to utilize the combination of Stokes and Anti-Stokes measurements for temperature measurements was demonstrated.

4.2.2 Spectral Dependence of Background Thermal Radiation

To characterize the background thermal radiation as a function of temperature, a 28.6 cm long segment of sapphire fiber was heated in a box furnace. Compared to the tube furnace, the thermal profile along the fiber segment inside the chamber is much more uniform, and the temperature drops sharply to room temperature at the outlet on the furnace wall. The Raman spectra and thermal backgrounds at different temperatures, as shown in Figure 74, were measured with the same optical setup shown in Figure 69. The spectra were smoothed via five point moving averaging.

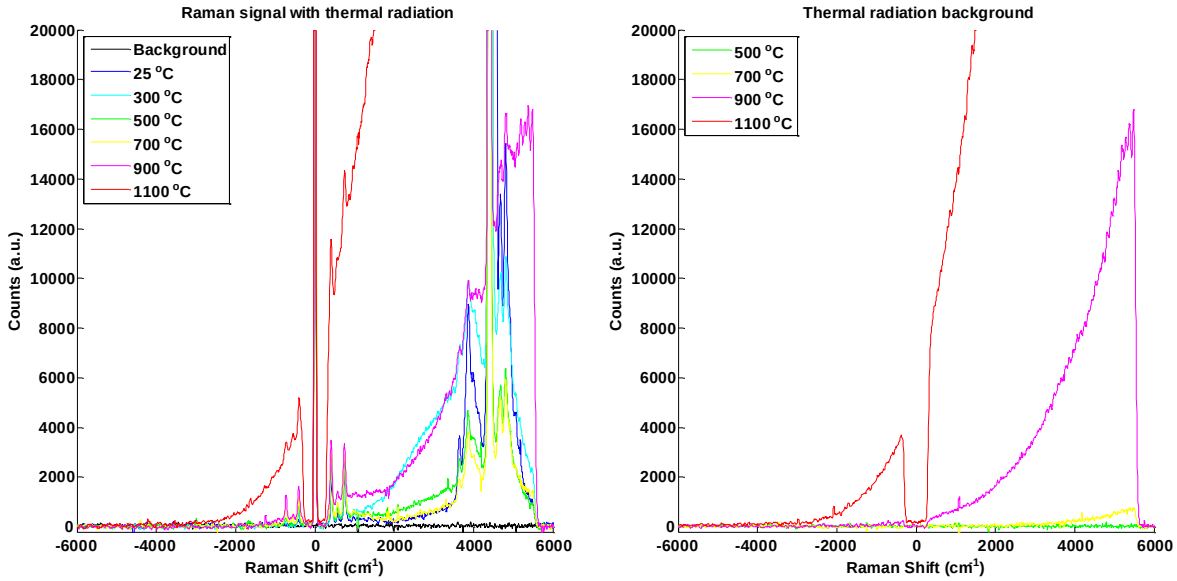

(a) **(b)**

Figure 74. Temperature dependence test of sapphire fiber Raman spectra using a box furnace. (a) Measrued raman spectra with thermal background. (b) Measured thermal background.

The characterization of the influence of the background thermal radiation on the Raman signal will guide the selection of the appropriate filters and sensor algorithm development. In addition, the results of this test indicated that the influence of the chromium fluorescence on the measurement must be addressed in the development of the temperature demodulation algorithms.

4.2.3 Observation of Fluorescence from Chromium Impurities

A fluorescence peak was clearly observed in the Raman response of the single crystal sapphire fiber via interrogation with a 532 nm laser, as shown in Figure 75. The spectral component presenting in both spectra corresponds to the light source background, and the differential component is the signal generated by the laser in the sapphire fiber, including the fluorescence and the Raman scatting light.

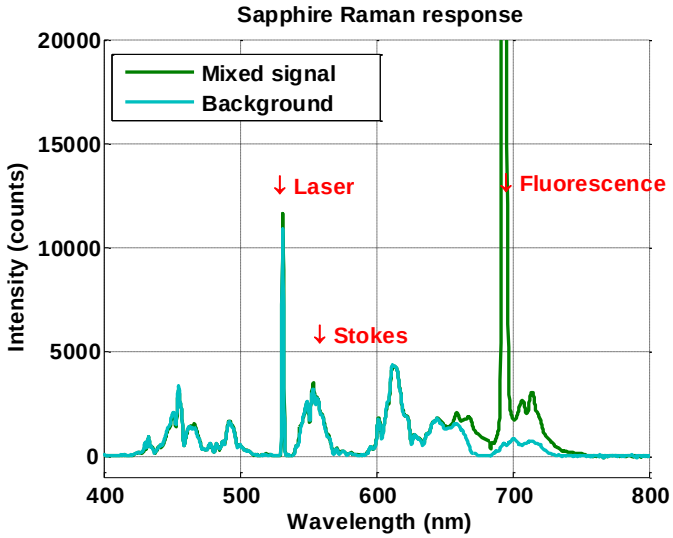

Figure 75. Spectra recorded in the background identification experiment: the cyan curve (Background) was acquired with the laser rejecting filter at laser output port, and the green curve (Mixed signal) was acquired with the laser rejecting filter placed before spectrometer

By subtracting the two spectra, the background introduced by the laser source was removed, as shown by the differential spectrum in Figure 76. A fluorescence spectrum is observed that peaks at 694.3 nm and spreads to both lower and higher wavelength (Figure 76 (a)). At the same time, two Stokes peaks can be clearly seen on a flat background at 544 nm and 554 nm corresponding to the Raman mode of 418 cm^{-1} and 751 cm^{-1} respectively (Figure 76 (b))

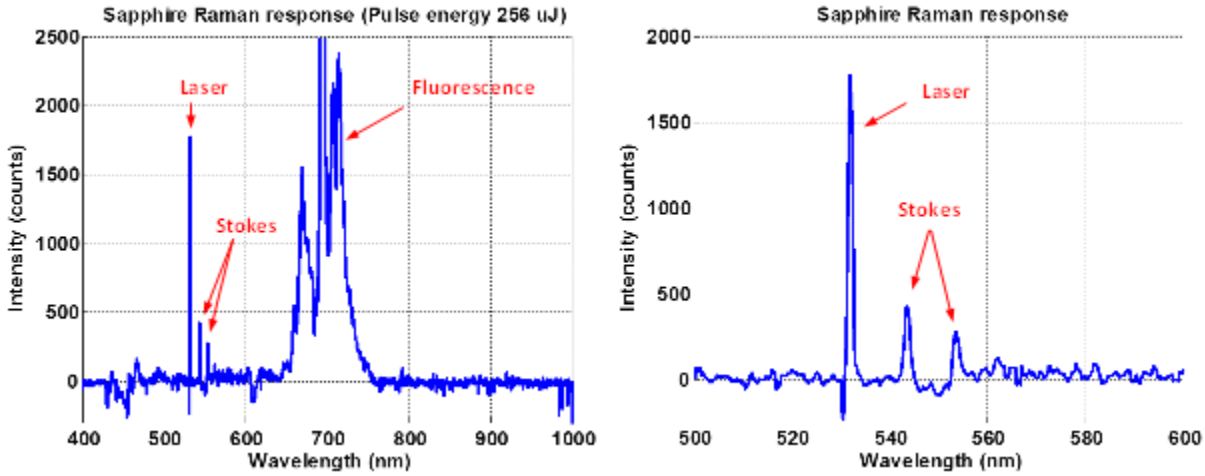

(a) **(b)**

Figure 76. (a) Differential spectrum showing the Raman signal and the fluorescence from the sapphire fiber; (b) zoomed in view at the wavelength of laser line and Stokes peaks

To eliminate the spectral background introduced by the laser source, a laser line clean-up filter with a width of 2 nm will need to be applied at the laser output port. While transmitting 90% light power at 532 nm, the band-pass filter had a minimum OD of 4 over rest of the wavelength range from 446.5 nm to 669.4 nm. With the aid of this filter, the laser-induced background can be removed without background measurements and subtractions.

4.3 Raman Distributed Temperature Sensing System

4.3.1 Comparison to Fused Silica Raman Backscatter Fiber Optic Sensing

To guide the development of the single crystal sapphire Raman backscatter sensing system, the anticipated performance was compared to fused silica-based systems, as shown in Table 7. The four primary system parameters (or components) that are compared are the laser, fiber, photodetector and "others". These key parameters will determine the final performance of the system to include the temperature resolution, spatial resolution, maximum sensing temperature and maximum sensing span.

Quantitatively, the ratio of the SNR between the two types of the systems is written as the product of the four factors listed in the table:

$$G_{total} = G_{fiber} G_{PD} G_{other} G_{laser} \tag{42}$$

where G_{laser}, G_{fiber}, G_{PD} and G_{other} are the SNR ratios between the two systems caused by the laser, the fiber, the photodetector and other factors respectively. A higher G_{total} correlates to a better SNR of the sapphire RDTS system compared to a silica RDTS system. The four components will be discussed individually as follows.

Table 7. Comparison of Silica and Sapphire Fiber RDTS Systems

Components	Parameters	Symbol	Traditional RDTS system	Sapphire fiber RDTS system*
Laser	Wavelength	λ	1550 nm	532 nm
	Repetition rate	f	412 KHz	100 KHz
	Peak power	P	80 mW	3.3 KW
	Pulse width	Δt	>10 ns	0.9 ns
	Beam quality	Q	-	1.2
	Life time	-	10,000 hour	10,000 hour
	Size	-	Small	Small
Fiber	Fiber type	-	SMF	Sapphire
	Fiber length	L	17 km	1 m
	Attenuation	α	0.22 dB/Km	0.46 dB/m
	Pulse broadening	-	No	Yes
	SBS threshold & damage threshold	P_{cr}	Low	High
	Refractive index	n	1.56	1.77
	Raman gain	G	High	Low
	Numerical aperture	NA	0.22	0.29
	Scattering coefficient	-	High	Low
APD + TIA	Quantum efficiency	-	>0.8 (1550 nm)	<0.7 (532 nm)
	Bandwidth	B	3 MHz	1 GHz

	Gain	A	9e5 V/W	1e5 V/W
	NEP	-	1.1e-13 W/Hz$^{1/2}$	4e-13 W/Hz$^{1/2}$
	Noise level	N	171 μV	1265 μV
Others	System loss	β	~0 dB	>6 dB
	Fluorescence	-	No	Yes
	Thermal background	-	Low	High
* Calculated results by using the parameters of a WEDGE XF 532nm laser from RMPC, and APD210 detector from Thorlabs. Results only for comparison and reference.				

Laser Source

Combining the all aforementioned factors, the SNR of the sapphire fiber RDTS system is 7.5×10^{-6} compared to a silica fiber RDTS system. To obtain a reasonable system SNR, G_{laser} must be high enough to compensate for all the other disadvantages combined. Fortunately, diode pumped solid state (DPSS) Nd:YAG lasers can offer very high pulse energy at 532 nm. Given the peak power and repetition rate of the laser, G_{laser} can be calculated as,

$$G_{laser} = G_{sample} G_{\lambda} G_{p} = \sqrt{\frac{f_{sa}}{f_0}} \left(\frac{\lambda_0}{\lambda_{sa}} \right)^4 \frac{P_{sa}}{P_0} \tag{43}$$

where G_{sample} is the improvement ratio related to the laser repetition rate, G_{λ} is the ratio of differential cross section depending on the working wavelength, G_p is the ratio of peak power, f is the effective repetition rate, λ is the laser wavelength, and P is the laser's peak power. The subscript '*sa*' and '0' denote the parameters for sapphire fiber RDTS system and silica fiber RDTS system, respectively.

By using the parameters of the WEDGE-XF-532 laser from RMPC, G_{laser} was calculated to be 1.46×10^{6}, which adequately compensates for the SNR disadvantage introduced by the other factors. The overall SNR ratio G_{total} is calculated to be 11, which offers a sufficient margin for all other factors not considered here including filter efficiency and thermal radiation.

Since the sapphire fiber loss is about 5 dB/m, a 3 m sapphire fiber system means 30 dB back and forth loss. Such high loss can be still compensated by a more powerful laser such as laser WEDGE-HF-532 from RMPC. The estimated temperature resolution of the far end of sapphire fiber is about 1000 times bigger than the front end due to the sapphire fiber loss. The theoretical G_{total} at the far end of a 3 m sapphire fiber RDTS system is 5.4 compared with traditional RDTS system, which means that the theoretical SNR at far end of a 3 m sapphire fiber RDTS system's is 5 times better with traditional one.

Fiber

The intensity of Raman scattering depends on a host of material properties, including the type of the material, the crystal orientation and the dopant concentration. Although Raman scattering is well characterized in silica fibers, there is limited information available for single crystal sapphire fibers. The Raman scattering intensity in a sapphire fiber was estimated by comparing it to different types of silica fibers with the same length using the Nd:YAG laser and spectrometer setup.

A 75 µm diameter sapphire fiber, a 50µm core step-index (SI) MMF and a 50 µm core graded-index (GI) MMF was tested. The acquired Raman spectra are shown in Figure 77.

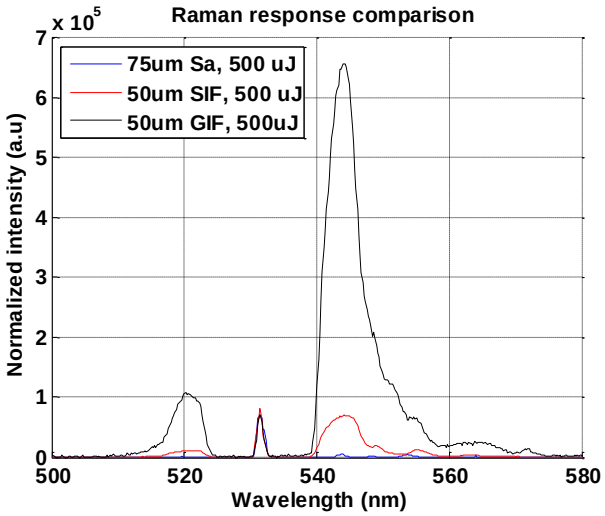

Figure 77. Raman scattering intensity of a 75µm diameter sapphire fiber, a 50µm core step-index multi-mode fiber and a 50µm core graded-index multi-mode fiber.

The narrow peak in the center is the filtered pump laser line, and the peaks on both sides of it correspond to the Stokes and anti-Stokes peaks.

According to the results, the Raman peak height of the GI-MMF is about 8.5 times that of the SI-MMF, and about 60 times compared to the sapphire fiber. The intensity difference between the GI-MMF and SI-MMF silica fibers was due to the variations in the light energy distributions and dopant concentrations in the fibers. In fact, the major source of Raman scattering in silica-based fibers is the germanium dopant in the core area. In a GI-MMF, most light power is confined near the center of the core region, where the dopant concentration is the highest. It has been experimentally confirmed that the Raman intensity in a 50 µm GI-MMF is on the same level with an SMF [65]. On the other hand, the comparison between the silica fiber and the sapphire fiber is a bit more complicated. Given the notably different Raman spectral widths, the total intensity ratio of the Raman signal in sapphire and silica fibers needs to be calculated by evaluating the areas of the peaks. The result predicts that the Raman signal of a 1m long, 75 µm diameter sapphire fiber is about 500 times weaker than a 50 µm diameter GI-MMF with the same length, which means $G_{fiber} \approx 0.002$.

Photodetectors

To detect the Raman signal in the visible range, silicon based APDs need to be used in the sapphire RDTS system instead of the InGaAs detectors used in silica fiber based RDTS systems. Compared to InGaAs detectors, silicon detectors have a lower intrinsic noise level, which is an advantage of working with visible light. However, the high spatial resolution requirement of the sapphire RDTS system greatly increases the bandwidth requirement on the silicon detectors, which nullifies their advantage because higher bandwidth comes with higher noise level.

In the updated system design, high-gain silicon based APDs are used with TIAs in pairs. The SNR ratio of such a detection system versus an InGaAs detector can be calculated by,

$$G_{PD} = \left(\frac{G_{amp}}{G_{noise}} \right) = \left(\frac{A_{sa}}{A_0} \right) \left(\frac{N_0}{N_{sa}} \right) \tag{44}$$

where G_{amp} is the ratio of the amplification coefficient of APD and TIA combined, G_{noise} is the ratio of noise level, A is the gain which converts and amplifies the light power into voltage, and N is the noise level. The subscript '*sa*' and '0' denote the parameters for sapphire fiber RDTS system and silica fiber RDTS system respectively. Using the parameters of APD210 from Thorlabs, the calculated G_{PD} is approximately 0.015.

System loss

Unlike the all-fiber based system design of the silica fiber based RDTS systems, the sapphire fiber RDTS system partially employs free space optics. The rational is based on the following:

- The peak power of the excitation laser pulses is beyond the damage threshold of silica fibers.
- Silica fibers, if used in the system, will generate very strong Raman signal which will overlap with the sapphire Raman signal.
- No MMF circulator or couplers are commercially available in visible range.
- The multiple filters used in the system are only available as free space optical components.

In the current system design, a 50-50 beam splitter is used to reflect the signal light into the detection arm. The two passes through the element will lead to an additional system loss of 75%, corresponding to $G_{other} = 0.25$.

Stimulated Raman Scattering threshold

Since laser pulses with very high peak power need to be used as the excitation light, the unwanted nonlinear effects such as stimulated Raman scattering (SRS) need to be taken into consideration. The generation of SRS will "confuse" the signal demodulation algorithm and result in measurement errors. For a Raman scattering peak with Lorentzian shape, the laser power threshold for generating stimulated Raman scattering in silica fibers was derived as,

$$\frac{g_R P_0^{cr} L_{eff}}{A_{eff}} \approx a \tag{45}$$

where $g_R \approx 1 \times 10^{-13}$ m/W at the wavelength of 1 μm, P_0^{cr} is the threshold power, A_{eff} is effective area, a is a constant depending on the scattering direction and light polarization, and L_{eff} is the effective length of the fiber defined by

$$L_{eff} = \left[1 - \exp(-\alpha_p \mathrm{L}) \right] / \alpha_p \tag{46}$$

where α_p is the fiber loss at the pump wavelength [66].

The calculated SRS thresholds for typical silica fibers with different mode field diameters are shown in Table 8.

Table 8. Comparison of Silica and Sapphire Fiber RTDS Systems

Wavelength (nm)	Length (m)	Loss (dB/km)	Mode diameter (μm)	Forward threshold, polarized (W)	Backward threshold, polarized (W)	Backward threshold, non-polarized (W)
1550	10,000	0.22	10.2	3.2	4	8
1550	10,000	0.22	50	78	97	194
532	1	200	50	346,000	430,000	866,000

As a reference, the 866 kW peak power threshold in a 50 μm diameter SI-MMF is already higher than the damage threshold of sapphire fibers in the current optical setup. With a lower Raman scattering intensity and higher loss, it is believed that SRS generation will not occur in the sapphire RDTS system.

Spatial resolution of sapphire fiber RDTS system

Taking modal dispersion into consideration, the spatial resolution of the RTDS system can be calculated as follows,

$$\Delta L = \frac{ct}{2n} + 2L\left(\frac{1}{\sqrt{1-\left(\frac{NA}{n}\right)^2}} - 1\right) \tag{47}$$

where ΔL is the spatial resolution, c is light speed in vacuum, t is the laser pulse width, n is the fiber's refractive index, L is the corresponding position on the fiber, and NA is the numerical aperture. It is clear that the spatial resolution of the system is composed of two components. The first term is related to the pulse width of the excitation laser, which is a constant at all positions on the fiber. The second term reflects the pulse broadening effect introduced by modal dispersion, which gradually increases along the fiber. The relationship between the laser pulse width, fiber length and spatial resolution is shown in Figure 78. For a 1 meter long sapphire fiber with 75μm diameter, the spatial resolution obtained using 1 ns pump pulses is 8.5 cm at the beginning section and increases to 11.2 cm at the end of the fiber.

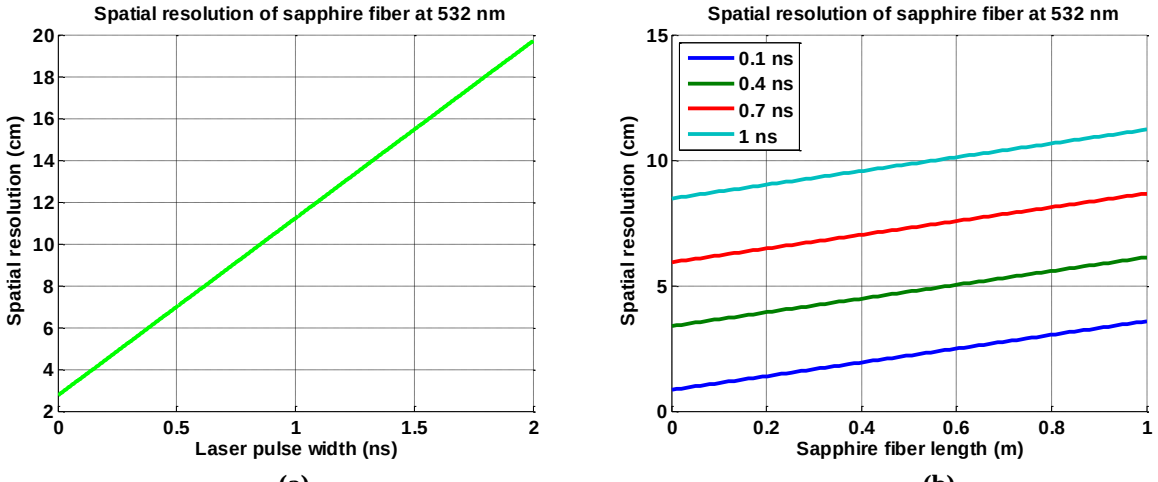

(a) **(b)**

Figure 78. Spatial resolution of a sapphire RDTS system using a 1m long, 75μm diameter sapphire fiber. (a) Spatial resolutions at the end of the fiber under different pump pulse widths. (b) Spatial resolution distribution along the fiber.

By using LMV sapphire fibers, the second term in Eq. 47 is expected to be greatly suppressed. In that case, the spatial resolution of the system will be nearly constant and determined only by the pulse width of the pump laser.

4.3.2 System Design and Performance

The schematic of the sapphire fiber Raman Distributed Temperature Sensing (RTDS) system is shown in Figure 79. The light source is a Q-switched Nd:YAG laser at 532 nm with a repetition rate of 10 Hz. The pulse energy in this experiment is about 5 μJ and the pulse width is about 700 ps. The calculated peak power is still far below the stimulated Raman threshold, thus higher pulse energy can be used to improve the signal to noise ratio (SNR) and temperature resolution. The pulse width for sapphire RDTS should be shorter than 1 ns because a longer pulse duration time may result in longer spatial resolution. Use of a shorter wavelength laser efficiently avoids

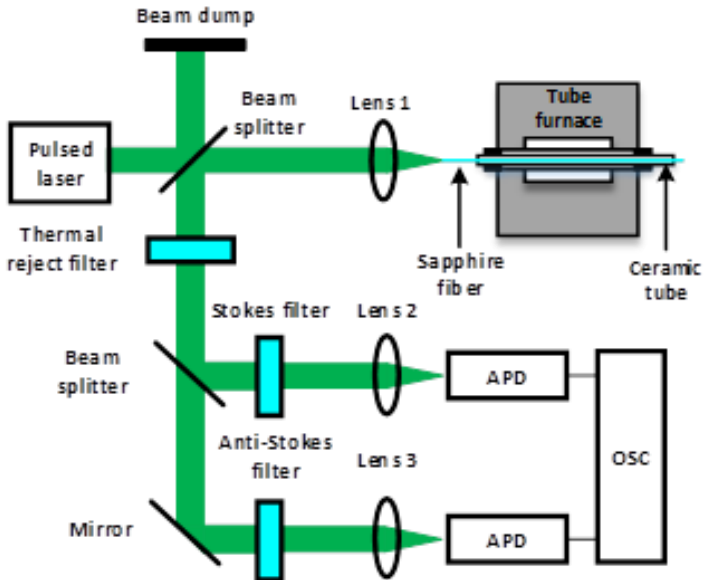

Figure 79. Schematic of the experimental setup for Raman DTS system.

the strong blackbody radiation background and increases the Raman intensity. The selected wavelength also avoids the fluorescence background at 694.3 nm which is due to Cr^{3+} ion impurities [26]. The laser beam was launched into a 1 meter long, 125 μm diameter sapphire fiber. As the laser pulse propagates in the sapphire fiber, part of the light was scattered. The scattered light can be categorized into three classes, namely, Rayleigh, Brillouin and Raman scattering. Both Rayleigh and Brillouin scattering are temperature and strain dependent. Raman scattering is not sensitive to parameters other than temperature in most applications. Such a characteristic makes it intrinsically more stable in harsh environment measurements. The Rayleigh and Brillouin scattered light and the reflected laser light are filtered before they enter the high-speed avalanche photodetector (APD). The Anti-Stokes and Stokes signals were measured simultaneously with the two identical APDs. Both band-pass filters must be carefully chosen to avoid the strong blackbody radiation and the fluorescence of the sapphire fiber, while not impeding the dominant Raman peak transmission.

The sapphire fiber was protected in an open-end ceramic tube, with an inner diameter 1.6 mm and outer diameter 6.75 mm and inserted into the furnace. The testing environment is ambient air. Since the Raman intensity is independent of refractive index of the cladding, the sapphire fiber Raman DTS are expected to work well in any gas environment. The temperature at the heating center was monitored by a K-type thermocouple, as shown in Figure 80. The temperature

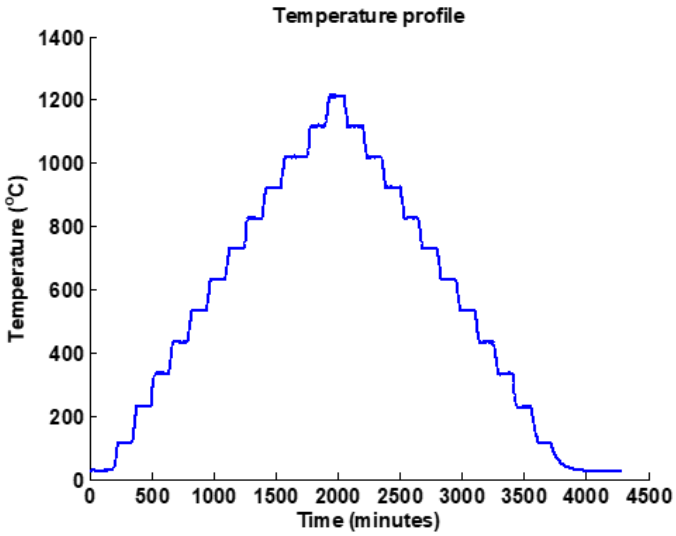

Figure 80. The temperature monitored by the K-type thermal couple shows clear steps from room temperature to 1200°C and back to room temperature.

was increased at a rate of 200°C/hour from room temperature up to 1200 °C and then decreased at the same rate down to room temperature. The temperature was kept constant for 120 minutes at each 100°C interval for measurements. The heating center was located at approximately 0.6 m from the coupling end face. The length of the heating section was about 60 cm (equal to the length of the protected ceramic tube).

The time-resolved Raman Stokes and Anti-Stokes scattering signals as a function of temperature are shown in Fig. 81. Each measurement was averaged for 180 seconds with 10 traces per

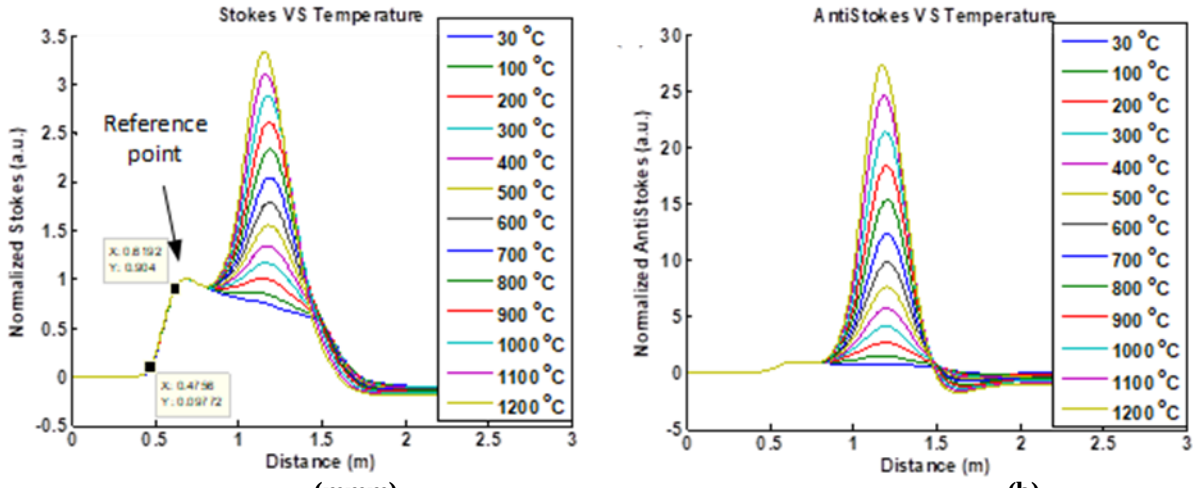

(mmm) **(b)**

Figure 81. (a) Raman Stokes signal of the sapphire fiber shows clear response within the heated area. (b) Raman Anti-Stokes signal of the sapphire fiber is more sensitive to the temperature variation.

second. All the Raman Stokes and Anti-Stokes signals were normalized by dividing by their reference point, which is at the beginning section of the fiber, to cancel out the laser power fluctuation. The Raman signals in the heated section vary with temperature, while the non-heated section remains unchanged. The mismatch at the end section was due to the dead time effect of the APD, which can be alleviated by proper calibration [67]. As predicted by theory, the Anti-Stokes response is more sensitive than the Stokes to the temperature variation.

Although signal degradation due to scattering and absorption losses is of concern for applications with an unclad sapphire fiber, the signal can be well resolved using the ratio of Anti-Stokes signal over Stokes signal. The Stokes signal undergoes almost the same waveguide attenuation as Anti-Stokes signal. Therefore, the Stokes signal response can be used to calibrate the intensity variation that is caused by changes of optical coupling efficiency, laser intensity fluctuation, waveguide attenuation and contamination resulting in long-term stability. Figure 81(a) also shows a spatial resolution of ~ 14 cm which derives from the 10%-90% response distance to a temperature step [68]. It is noted that the heating profile along the sapphire fiber is not a perfect step between the heated section and non-heated section. The heated section maintains a parabolic temperature profile. Due to such a heating profile, the spatial resolution is derived from the beginning section of the fiber. Since the spatial resolution of the current RDTS system is determined by the bandwidth of the oscilloscope, the performance can be further improved by using a high speed OSC.

There are over 200 valid points along the sapphire fiber. Theoretically, each point represents parts of the distributed temperature information. If we only track one point at the heating center, we were able to show the relationship of the normalized intensities of the Raman Anti-Stokes/Stokes signals versus the thermal couple measurement result. The results are plotted in Figure 82(a). The temperature response of the Stokes component is near linear, and the Anti-Stokes component increases much faster than the Stokes, which agrees with the theoretical prediction. The intensity variation is due to the instability of the photodetector and the laser

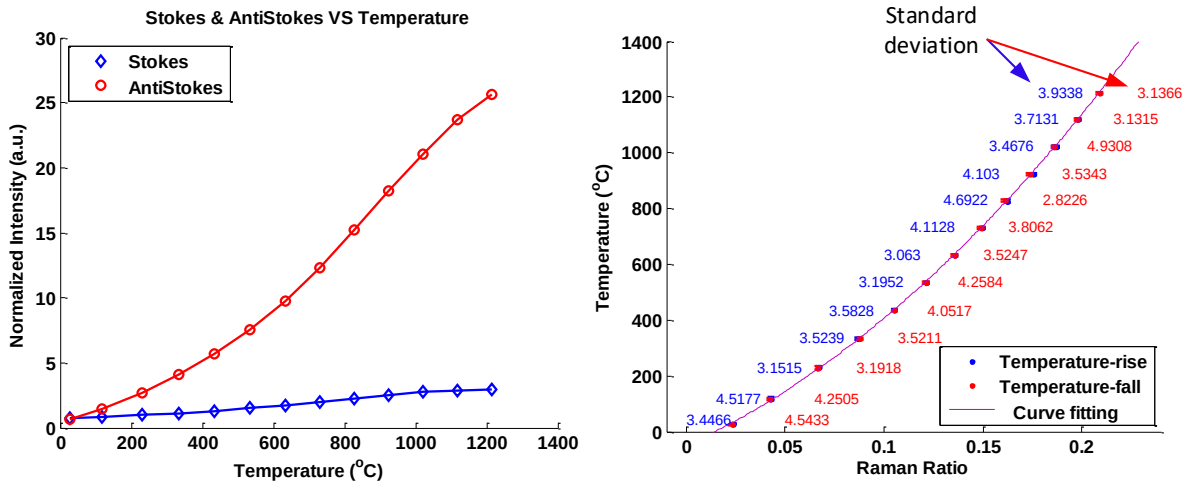

(yyyyy) (b)

Figure 82. (a) Both Stokes and Anti-Stokes signal at the heating center shows strong temperature dependences. (b) The Raman ratio of the sapphire fiber at heating center increases greatly with temperature up to 1200°C with an averaged standard deviation of 3.7°C. The blue numbers correspond to standard deviation of temperature-rise period and the red ones correspond to that of temperature-fall period.

intensity. Since the ratio of the Anti-Stokes signal over the Stokes signal is usually used in temperature demodulation for self-calibration purposes, the result of the same point is calculated and shown in Figure 82(b)

The Raman ratio curve of the temperature-rise and temperature-fall period shows good repeatability. The standard deviation does not degrade at higher temperature. The averaged standard deviation of all temperatures is 3.7°C. This performance can be further improved, in the future, by using temperature compensated APDs and higher pulse energy. A distributed temperature curve can be derived from the Raman ratio of all valid points along the sapphire fiber. Subsequent research will carry on making full use of the hundreds of valid points along the sapphire fiber. Since the fiber is within 1 or 2 meters range and in most practical applications, the temperature distribution in this short range does not change dramatically, the sapphire RDTS may provide more detailed temperature information compared with a multiplexed array of thermocouples and save on costs.

In summary, the RDTS system in sapphire fiber was demonstrate experimentally from room temperature to 1200°C with a spatial resolution of 14 cm. The averaged standard deviation of the demodulated signals is 3.7°C over 180 second averaging time. The demodulated results showed good repeatability between the temperature-rise curve and the temperature-fall curve. Use of the Raman ratio for temperature deduction and self-calibration capability allows for long-term stability by minimizing the intensity variation due to the change of optical coupling efficiency, laser intensity fluctuation, waveguide attenuation and contamination. The absence of additional materials (i.e. bonding materials) greatly reduces the risk of external contaminations and ensures the minimum diameter on the order of the micro-scale. Furthermore, the technique is insensitive to pressure and strain which prevents any cross talk in the temperature measurements.

4.3.3 Sensing Span and Spatial Resolution

The RDTS system was demonstrated for a 2 meter length sapphire fiber with a 122 μm in diameter. The experiment schematic is consistent with that shown previously in Figure 68. As shown in Figure 83, the time-resolved Raman Stokes signal and Anti-Stokes signals were

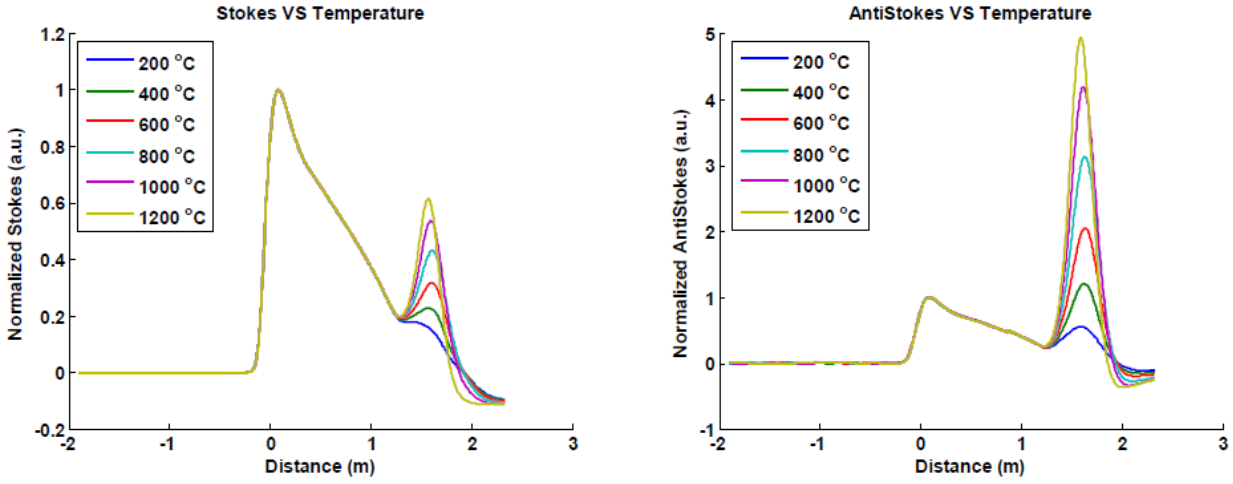

(a) **(b)**

Figure 83. The Raman Stokes and Anti-Stokes signals in a 2 meters long sapphire fiber show clear temperature response.

successfully recorded for the sapphire fiber was heated from room temperature to 1200ºC at intervals of 200ºC; and the average time for each measurement was 3 minutes. The demodulated signal at the heating center over the temperature rising and temperature falling period is shown in Figure 84. The observed slight variation in the temperature-rising and temperature-falling was suspected to arise from the instability of the furnace and the APD.

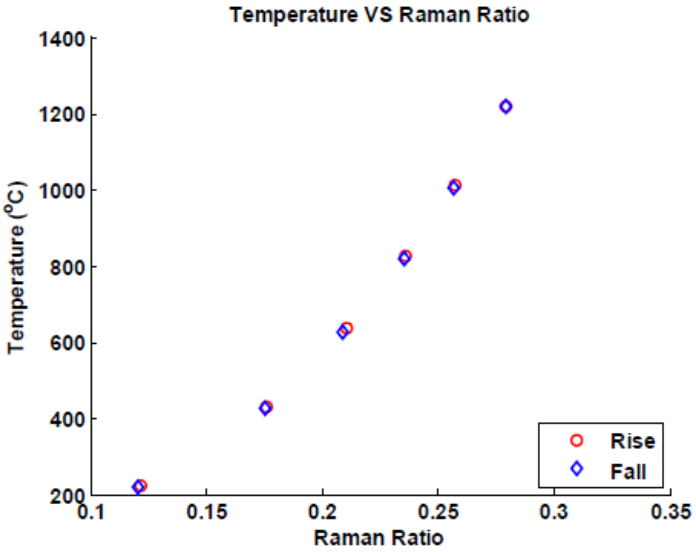

Figure 84. The demodulated signals at temperature rising period are almost the same as the temperature falling period in sapphire fiber RDTS.

Ultimately, the Raman DTS was tested with a 3 m sapphire fiber. Since the maximum length of the customized sapphire fiber was 2 meters, a 1 meter long sapphire fiber (125 µm diameter) was connected to a 2 meters sapphire fiber (122 µm diameter). All fiber ends were made into 140 µm APC pigtails. The heating position was located at the end of the 3 meter sapphire fiber. A B-type thermocouple was used to monitor the temperature at the furnace center. The laser repetition rate was 10 Hz and the average time for each measurement was increased to 30 minutes. The Raman signals of this 3 meter sapphire fiber from 224ºC to 1216ºC, are shown in Figure 85. An

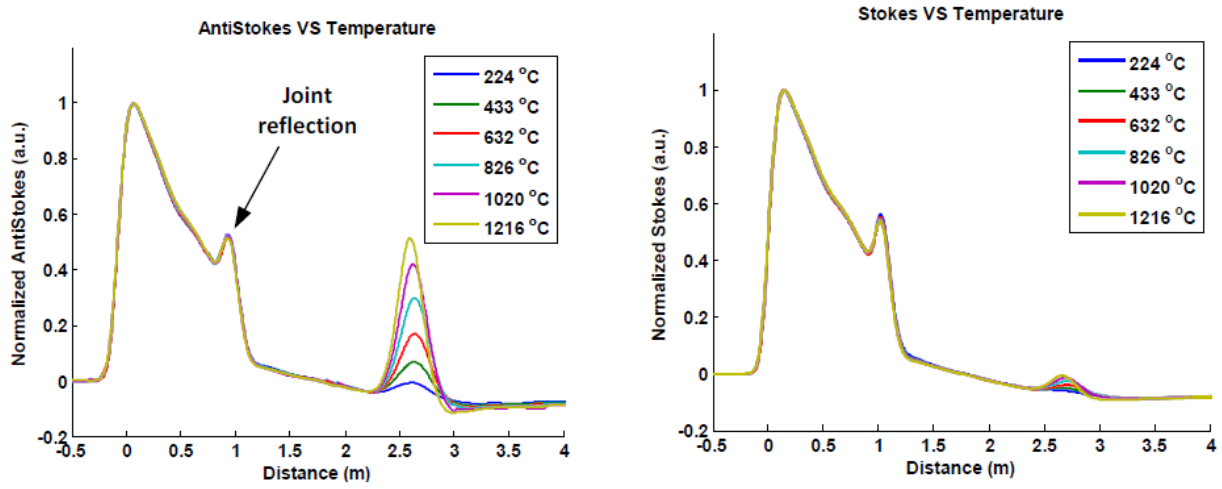

(a) **(b)**

Figure 85. The Raman signals at different temperatures in a 3 meters sapphire fiber.

additional loss at the joint was observed, which was due to the mismatch of the fiber diameters. Due to the dead-time effect of the APD, the corresponding voltage dropped below zero, and will require additional calibration in subsequent project quarters. As shown in Figure 86, the anticipated relationship between the Raman intensities as function of temperature was observed.

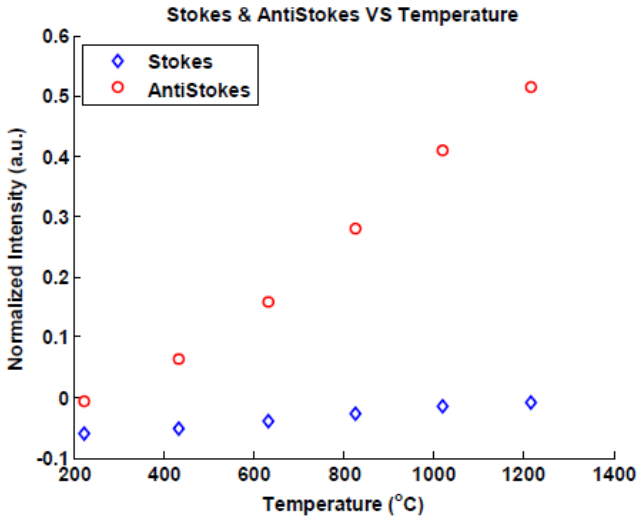

Figure 86. The normalized Raman signals vary at different temperatures.

To evaluate the spatial resolution of the system, the sapphire fiber was heated to 1400ºC at the same location, very close to the end of the sapphire fiber. The Raman Anti-Stokes signal is shown in Figure 87. The corresponding spatial resolution is 16.4 cm, which was derived from the 10%-90% response distance to a temperature step. Furthermore, it is anticipated that the achievable spatial resolution will ultimately be less than 16.4 cm, because a precise temperature step could not be obtained at a temperature of 1400ºC for the furnace.

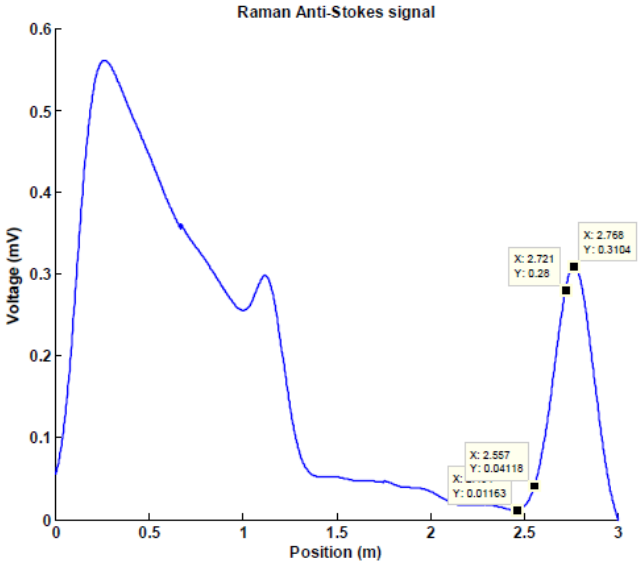

Figure 87. The spatial resolution is about 16.4 cm which derived from the 10% -90% intensity.

5 QUASI-DISTRIBUTED TEMPERATURE SENSING SYSTEM

5.1 Single Crystal Sapphire Fiber Bragg Gratings

5.1.1 Point-By-Point Fabrication of FBGs

FBGs fabricated in sapphire fiber by femtosecond laser have been demonstrated for sensing applications up to 1745°C [69] An advantage of utilizing the femtosecond laser for the FBG fabrication is that it provides high peak intensity, which enables a multi-photon process with sufficient efficiency for permanent change of refractive index., as shown in Figure 88. Phase mask exposure and point-by-point inscription are the most common techniques to fabricate an

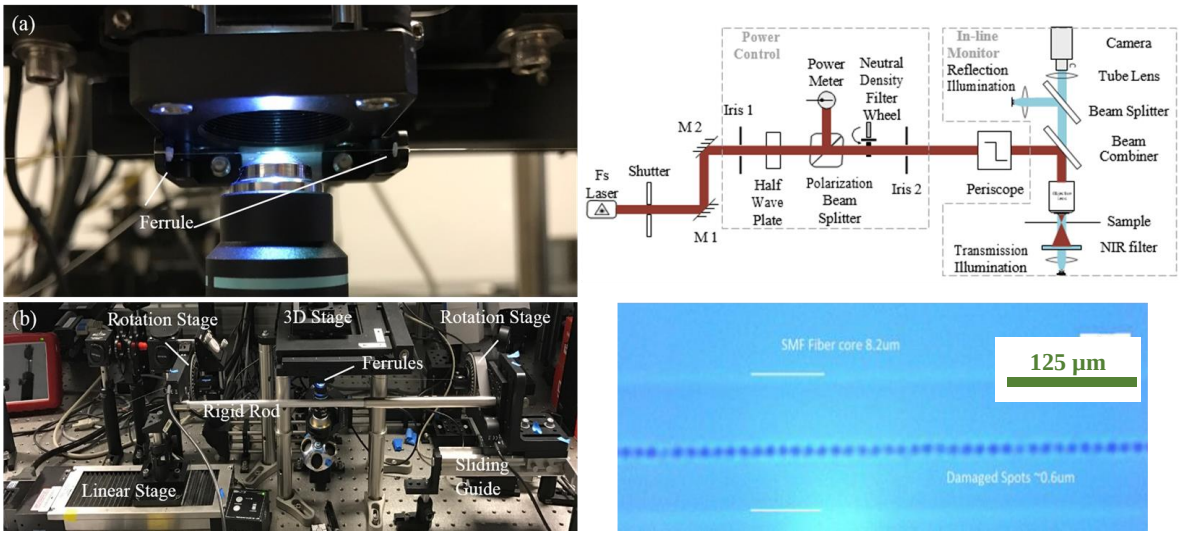

Figure 88. (a,b) FBG fabrication setup with femtosecond laser at VT. (c) Schematic for the automated femtosecond laser micromachining system at VT. (d) Point-by-point FBG writing on fused silica single mode fiber.

FBG [70]. The phase mask technique either uses the interference pattern directly located behind a phase mask or an additional interferometer is with a phase mask functioning as a beam splitting element to form an interference pattern; the entire grating structure is formed at the same time with this method. Conversely, for the point-by-point approach, the laser is focused into the core of a fiber to induce a localized refractive index change point and then the grating is created by scanning the fiber so that the points are periodically distributed along the fiber. The advantage of using the point-by-point inscription over the phase mask method is the inherent flexibility. A range of grating structures fabricated via this method have been reported and it is quite easy implement wavelength division multiplexing (WDM) [71, 72].

To the best of our knowledge, only the phase mask method has been successfully applied to the fabrication of FBGs in single-crystal sapphire fibers, including both direct phase mask exposure and phase mask-based Talbot interferometer [73]. The direct phase mask exposure can be used only to inscribe FBGs in a sapphire fiber with a single Bragg wavelength per fabrication due to the fixed pitch of the phase mask. Although the use a Talbot interferometer provides better geometrical flexibility, the extremely short pulse width requires the path difference between the two arms of the interferometer to be tuned within a few micrometers to achieve good

overlapping of the laser pulses, and thus, requires a fabrication setup with high stability and accuracy.

The sapphire fiber FBGs were inscribed by a point-by-point method with a 780 nm femtosecond (IR-fs) laser. The phase matching condition for a fiber Bragg grating is given by [70]

$$m\lambda_{Bragg} = 2n_{eff}\Lambda \tag{48}$$

where m is the order of the grating, λ_{Bragg} is the Bragg wavelength, n_{eff} is the effective refractive index of the reflected mode, and Λ is the pitch of the grating. Since the refractive index of sapphire fiber is about 1.745 at 1550 nm, the pitch of the first few-orders grating with Bragg wavelength lying in the C-band is smaller than 2 μm. Thus, a sufficiently small laser focal area is necessary, which requires the use of high magnification lens.

The femtosecond laser used in the fabrication was a Ti: Sapphire IR-fs laser (Coherent Libra series) with a 780 nm emission wavelength and 3 mm-beam-waist Gaussian beam. The required focal length can be estimated via $w = \lambda f / \pi w_0$, where λ is the wavelength of the laser in the medium, f is the focal length of the lens, and w_0 is the input beam waist. Thus, a Nikon objective (100X, NA=1.25) was selected for the setup.

A single-crystal sapphire fiber (Micromaterial Inc.) with c-axis as the axial direction was used and one of its flat faces was tuned to be normal to the incident beam in the fabrication setup, as shown in Figure 89(a). As opposed to fused silica, sapphire is a birefringence material and the subsequent distortion must be taken into account in the design of the fabrication setup [74-76].

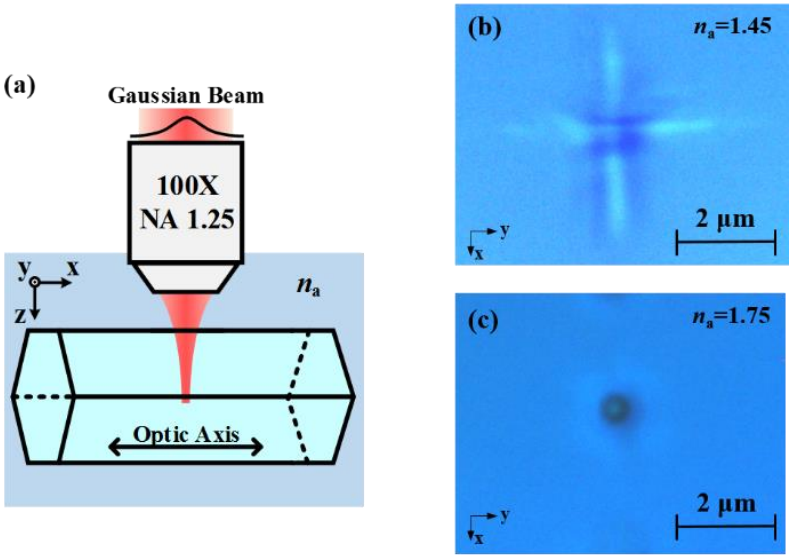

Figure 89. (a) Scheme for laser focusing in the fabrication. Microscopic image of the top view of single-pulse damage geometry with different ambient refractive indices (b) n_a = 1.45 and (c) n_a = 1.75. (Laser pulse energy = 1.6 μJ)

The plane waves become superimposed with different incident angles for a linearly polarized input beam, and inevitably contain both extraordinary and ordinary components respect to the crystal and behave differently inside the crystal. The subsequent distortion of the beam arises from a combination of boundary and bulk effects. The boundary effect represents the different

refraction at the ambient/crystal interface for extraordinary and ordinary components, and the bulk effect represents the anisotropic propagation constant inside the crystal [74-76]. Given a specific birefringence, the boundary effect is dependent on the refractive index mismatch at the interface and the NA of the focusing system, while the bulk effect is dictated by the focal depth inside the crystal.

To evaluate the influence of birefringence in the FBG fabrication, the damage point geometry was investigated under two scenarios; an ambient refractive index that matches that of the sapphire fiber and the ambient refractive index that does not match the sapphire fiber. The energy of the laser pulse was tuned sufficiently high to generate a stable damage geometry and ensure that the induced damage revealed the entire focal point geometry. Prior to focusing, the polarization was tuned to be perpendicular to the optical axis to reduce the extraordinary components. The microscopic image of the geometry of the induced damage point in a 125 µm sapphire fiber with different ambient refractive indices is shown in Figure 89(b, c). It is evident that the geometry of the focal point is distorted as a "cross" shape when the ambient refractive index differs from that of sapphire. The "cross" shape damage geometry is the result of birefringence-induced focal point split and can be understood as a Gaussian beam focused by two cylindrical lenses with orthogonal orientations and different focal lengths [75, 76]. Conversely, a very clean damage point with a round shape is created when the ambient refractive index closely matches the sapphire. Thus, the boundary effect is dominant in our fabrication setup, while the bulk effect can be neglected since no observable focal point distortion upon refractive index matching. Thus, by using an oil that closely matches the sapphire's index as the ambient environment, the focal distortion induced by the birefringence can be minimized.

The point-by-point FBG inscription method is shown in Figure 90(a). The fiber is mounted on a 5-axis translation stage and moves along the axial direction at a constant speed (v_s) while the

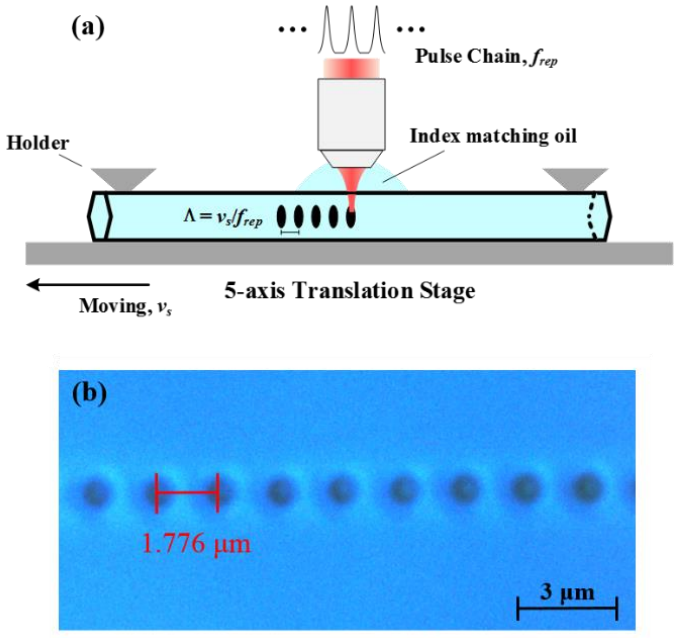

Figure 90. (a) Scheme for the procedure of FBG inscription in sapphire fiber via point-by-point method. (b) microscopic image of the inscribed 4th-order FBG in 125 µm diameter sapphire fiber with Bragg wavelength 1550 nm. (Laser pulse energy = 1.6 µJ)

laser pulses with a constant repetition rate (f_{rep}) to induce localized refractive index change at the focal point. The pitch of the inscribed FBG can be easily controlled by tuning the relation between the moving speed and the repetition rate, and the FBG length can be adjusted by controlling the total number of the laser pulses. A microscopic image of an inscribed FBG in the center of a single-crystal sapphire fiber with a 125 µm diameter is shown in Figure 90(b). A pitch of 1.776 µm was obtained with a moving speed of 0.88 mm/s and a laser repetition rate of 500 Hz. This FBG corresponds to a 4th order grating for the lowest guided mode at wavelength of 1550 nm and a total grating length of 2 mm only required ~ 2.5 seconds of inscription time.

Characterization of the inscribed FBG was conducted with the setup shown in Fig. 91(a). A superluminescent light emitting diode (SLED) with a center wavelength of 1565 nm and bandwidth of 80 nm (Thorlabs S5FC1005P) was used as the light source. A step-index 105/125

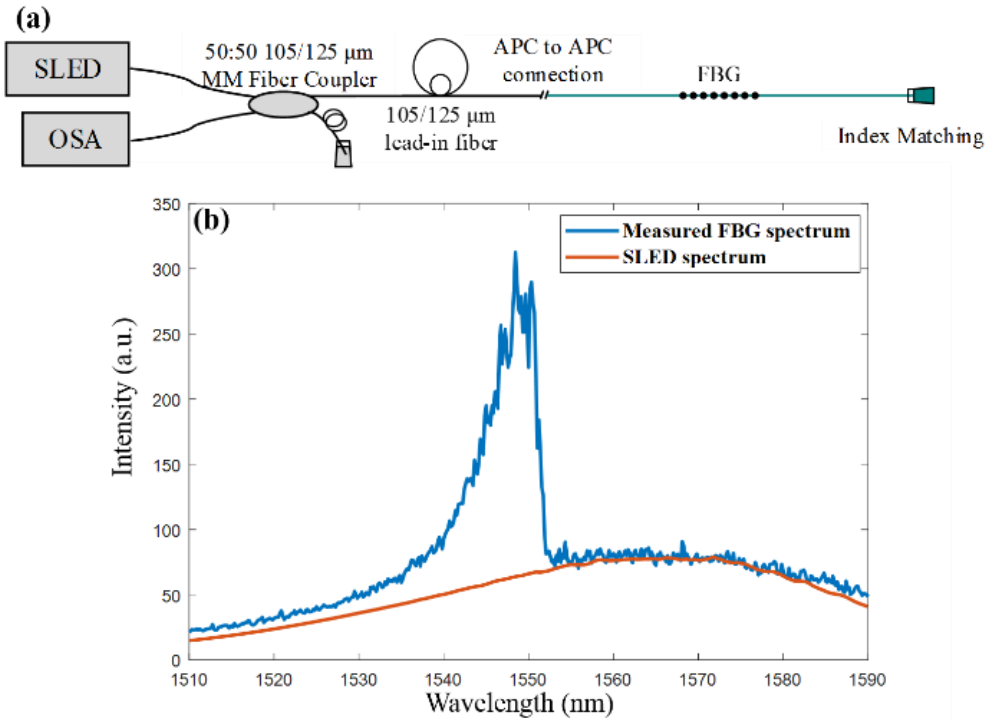

Figure 91. (a) Scheme for the setup of measuring the reflection spectrum of the inscribed FBG in sapphire fiber. (b) Measured reflection spectrum of the inscribed FBG.

µm multimode silica fiber was chosen as the lead-in fiber because it will excite a sufficient number of modes into the sapphire fiber, and thereby yielding a full characterization of the FBG reflection spectrum; a customized 2x2 3 dB 105/125 µm multimode fiber coupler was also used. The idle port of the coupler was tied into a small knot and dipped into a refractive index matching gel to prevent end reflections. In addition, the sapphire fiber was connected to the lead-in fiber with a FC/APC connection and the other end was polished to 7 degrees and dipped into a refractive index matching gel to further minimize the background reflection. The reflection spectrum of the inscribed FBG was recorded with an optical spectrum analyzer (OSA) (ANDO AQ-6315A), as shown in Figure 91(b). The large number of modes propagating in the sapphire fiber, the reflective spectrum produce a broad peak with ripples on the top.

The point-by-point method was also employed to fabricate FBGs with different lengths and center wavelengths, as shown in Figure 92(a), and can be utilized in WDM applications. In addition to the inscription, the traverse speed of the fiber is varied as a function of fiber position, while the pulse rate of the laser is held constant. By using this method, multiple FBGs with different Bragg wavelengths can be inscribed in a sapphire fiber with only one scan. The length of each FBG and the separation can also be easily tuned without changing the physical configuration. Three cascaded FBGs in a sapphire fiber were fabricated with fundamental mode Bragg wavelength at 1549.8 nm, 1566.5 nm, and 1584.3 nm, respectively as shown in Figure 92(b).

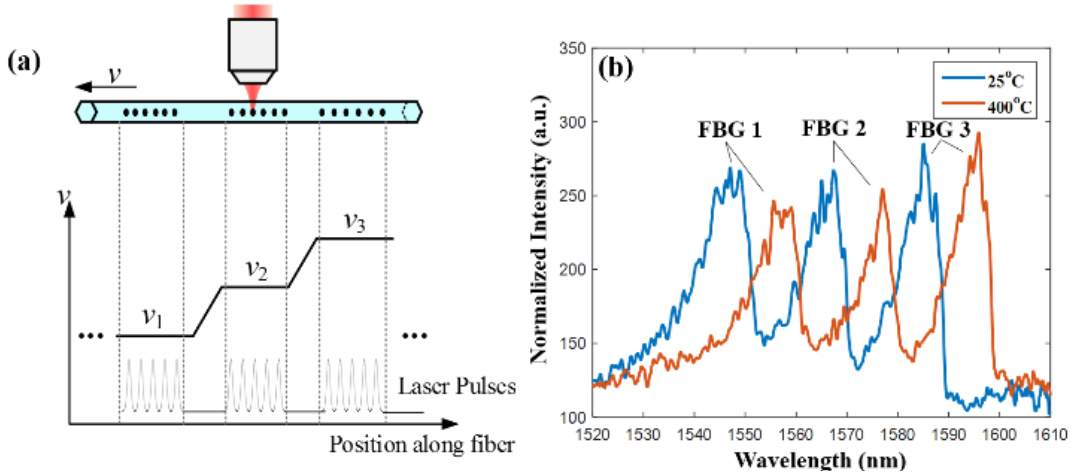

Figure 92. Procedure of fabricating wavelength multiplexed FBG array with one scan. (b) Measured reflection spectrum (normalized to the SLED spectrum) of the three FBGs multiplexed array under different temperatures.

5.1.2 Thermal Annealing of FBGs

The FBG temperature response was evaluate by placing the three serial FBGs array inside a tube furnace and monitoring their reflection spectrum. The temperature of the furnace was varied from room temperature to 1400ºC and a B-type thermocouple is placed at the same location of the FBGs to record the temperature. As shown in Figure 93(a), the Bragg wavelength and reflectivity of FBG1 varied with temperature and the increase in reflectivity is permanent. Upon enhancement of the FBG spectrum after heating, variation of the background signal is due to the blackbody radiation, as shown in the lower plot in Figure 93(a).

The FBG peak position and reflectivity is shown in Figure 93(b) and the evolution of the FBG reflectivity enhancement factor becomes evident with time and temperature. The reflectivity is evaluated by applying two-Gaussian fitting to the spectrum (the inset in Fig. 93(b)) and the enhancement factor is obtained by normalizing the reflectivity to the one at room temperature. The reflectivity begins to increase at 600ºC and tends to be stable above 1200ºC. Several additional temperature cycling tests were also performed with the heat-treated FBGs and no further reflectivity change was observed. Thus, these experimental results show that by applying heat treatment of temperature ramping from 600ºC to 1200ºC, the reflectivity of the original FBG in a sapphire fiber can be permanently enhanced by about 5.5 times

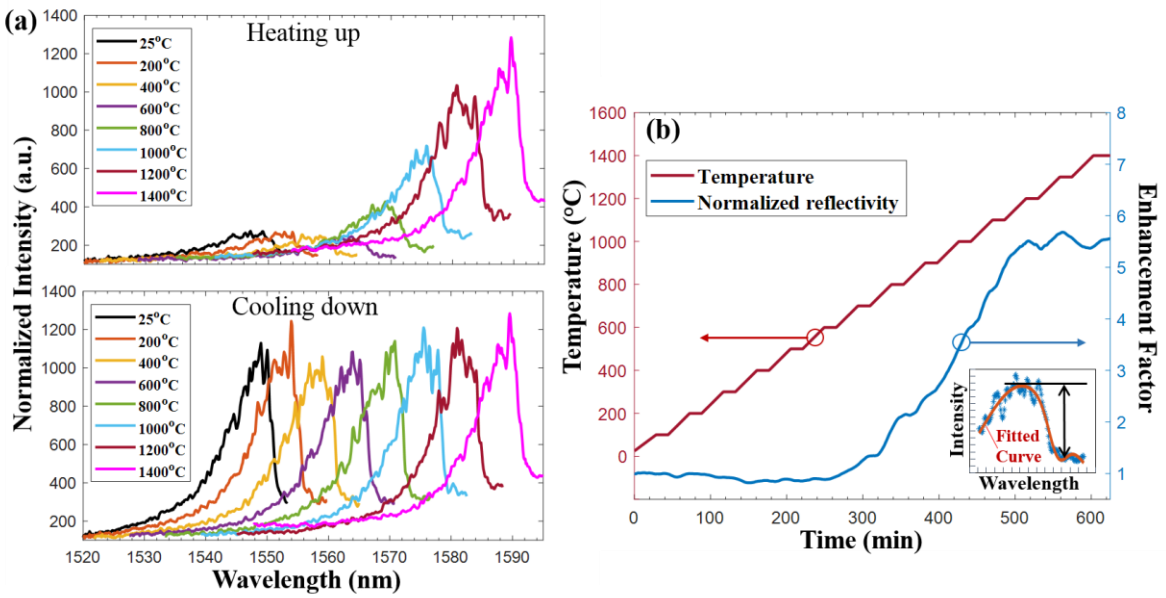

Figure 93. (a) Normalized reflection spectrum of FBG 1 under different temperature during heating up and the followed cooling down, (b) the enhancement factor of reflectivity of the same FBG with the increasing of temperature. Inset: reflectivity evaluation by the two-Gaussian fitting of the spectrum.

5.1.3 Temperature Response of FBGs

The linear temperature dependence of the Bragg wavelength is shown in Figure 94. A polynomial fit of this line yielded a slope of ~25.8 pm/ºC from room temperature to 1000ºC which is consistent with the theoretical and measured values reported in the literature [77-79]. Above a temperature of 1000ºC, the slope of the line increases, which is also consistent with observations reported in the literature [77-79]. Thus, the FBG technology developed in this quarter of the project can be leveraged for distributed temperature measurements and is anticipated to improve with the use of the LMV sapphire.

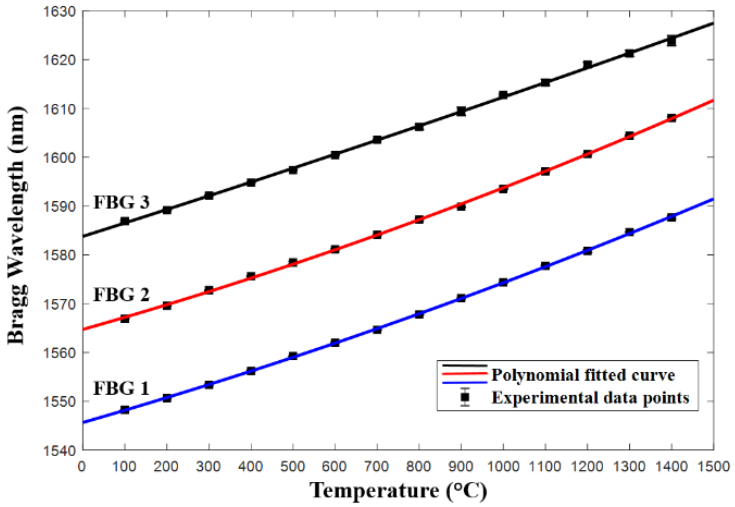

Figure 94. Temperature dependence of the Bragg wavelengths of the FBG array. Data with error bar is shown.

5.2 Low Modal Volume Single Crystal Sapphire Fiber Bragg Gratings

5.2.1 Fabrication of LMV Single Crystal Sapphire FBGs

All the reported SFBGs were fabricated in a fiber with a diameter over tens of micrometers. Due to the strong field confinement caused by the large diameter and significant core-clad refractive index difference (1.76 and 1), the inherent reflection spectrum of the reported air-clad SFBGs has a broad peak and is highly insensitive to ambient environmental changes, limiting their measurement accuracy and sensing applications. An FBG fabricated in the LMV sapphire fiber can overcome the mentioned difficulties because of the narrow bandwidth and substantial evanescent field propagating in the surrounding medium. Furthermore, the small size of the microfiber provides excellent mechanical flexibility and enables convenient configurations.

The fabrication method is illustrated in Figure 95(a). The procedure begins with fabricating an FBG in a large diameter single-crystal sapphire fiber first, and then wet-etching the fiber down to microfiber size in a hot sulfuric-phosphoric acid solution. The beginning sapphire fiber was 125

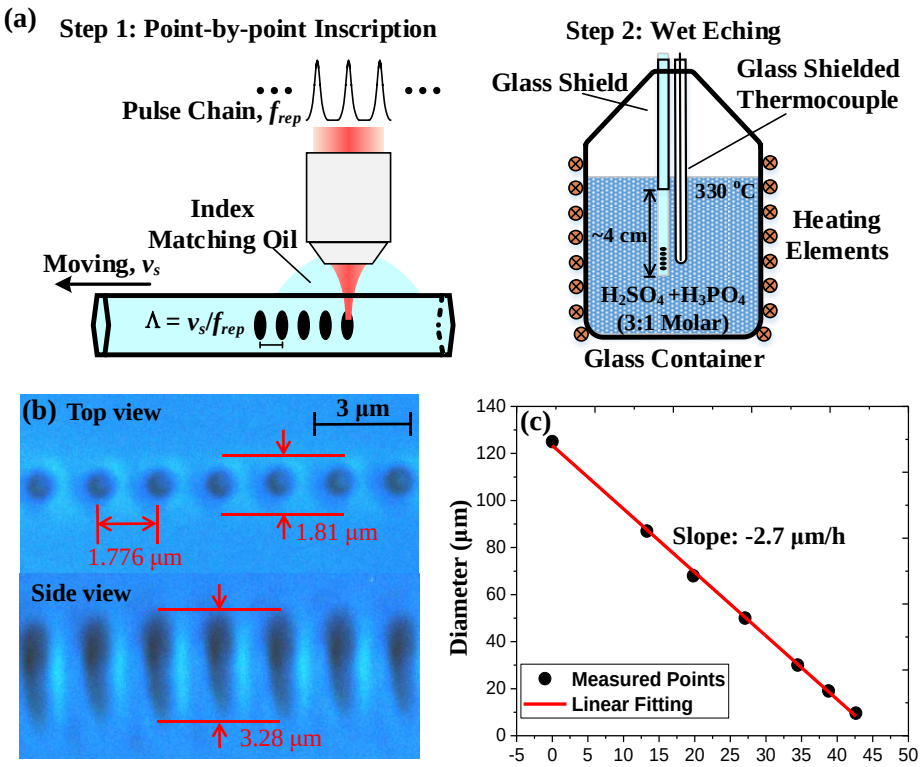

Figure 95. (a) Fabrication method of micro-SFBG, (b) optical microscopic image of inscribed FBG (top and side view), (c) relation between the diameter of the sapphire fiber and the etching time.

μm diameter (MicroMaterial Inc.). There are two common methods to inscribe an FBG in a sapphire fiber, point-by-point inscription and phase-mask exposure [69, 80]. The point-by-point inscription method was selected here due to the small damage cross-section it can induce, preventing different etching performance between damaged and undamaged regions, as shown in Figure 96. A Q-switched pulsed Ti: Sapphire IR- femtosecond laser (Coherent Libra series) with

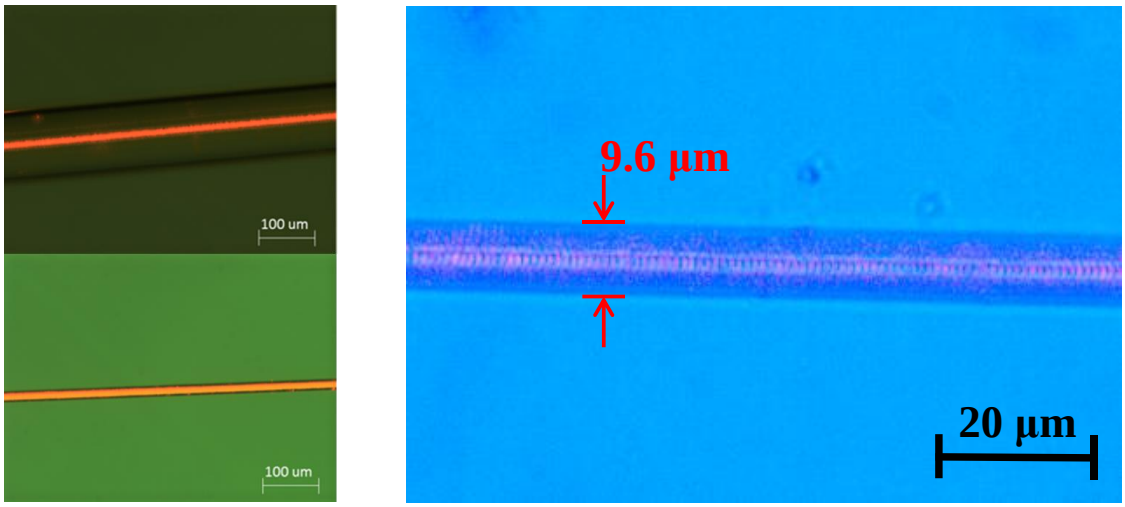

(a) **(b)**

Figure 96. Optical microscopic image of the fabricated 9.6 µm LMV-SFBG. The FBG is illuminated by a 638 nm red light injected into the fiber.

780 nm emission wavelength, ~100 fs pulse width, and 3 mm (beam-waist) linear polarized Gaussian beam was used. The laser beam was focused through a 100X Nikon objective into the center of a sapphire fiber through a refractive index matching oil to reduce the aberration at the interface. The fiber was mounted on an assembled 5-axis translation stage (Aerotech ABL10050L-LN and Newport 562 Series) and traversed along the axial direction at a constant speed (v_s). The speed accuracy of the stage was within 10 nm, assuring the uniformity of the pitch. In the meantime, laser pulses with a constant repetition rate (f_{rep}) are focused into the fiber to induce localized refractive index changes. The desired pitch of the inscribed FBG was achieved by tuning the relation between the translation speed and the repetition rate. The length of the FBG was adjusted by controlling the total number of the laser pulses. The transverse speed was 0.88 mm/s and the repetition rate of the laser was 500 Hz, which induced an FBG with 1.776 µm pitch, corresponding to the 4th order grating for the lowest guided mode at wavelength of 1550 nm for 125 µm diameter fiber. A 2 mm long grating was fabricated near the end of the sapphire fiber. Figure 95(b) shows the microscopic image of the inscribed FBG in the center of a single-crystal sapphire fiber with 125 µm diameter. The cross-sectional area of the damage is about 1.81 µm width and 3.28 µm depth. The resulting grating was then placed in a furnace and annealed at 1400 ℃ for 6 hours to increase and stabilize the reflection spectrum as reported in [5].

As the second step, the annealed grating was then wet-etched by the method described in [7, 8]. The etching solution was a 3:1 molar ratio of sulfuric acid (98%, Fisher Scientific) and phosphoric acid (85%, Acros Organic). The mixed solution was then heated by resistance wire and carefully maintained at 330℃ for stable etching performance. The FBG fiber section (~4 cm) was subsequently immersed in the solution and removed every few hours to monitor the change of diameter and reflection spectrum. A glass-shielded thermocouple was placed at the same position as the SFBG to monitor the solution temperature. Another glass shield was used to mask the fiber section outside the solution to prevent sulfate deposition from the vapor [8]. As indicated in Figure 95(c), the diameter of the immersed sapphire fiber was reduced at the rate ~2.7 µm/h. After approximately 42.5 hours, the immersed part was reduced to a 9.6 µm diameter.

There was a short taper-like region (~0.5 cm) around the bottom exit of the glass shield and the diameter of all the other shielded fiber section was intact.

5.2.2 Performance of LMV Single Crystal Sapphire FBGs

The reflection spectrum is characterized by illuminating the SFBG with a broadband source. The source used here was a superluminescent light emitting diode (SLED) with a center wavelength of 1565 nm and bandwidth of 80 nm (Thorlabs S5FC1005P). Step-index 105/125 μm multimode silica fiber was chosen as the lead-in fiber because it can excite a sufficient number of modes into the sapphire fiber, which gives us a full characterization of the reflection spectrum of the SFBG. FC/APC butt coupling is used between the lead-in fiber and the sapphire fiber to reduce the background reflection. The reflection spectrum was recorded by an optical spectrum analyzer (OSA) (ANDO AQ-6315A) with 0.02 nm accuracy. The air-clad SFBG reflection spectra at different fiber diameters is shown in Figure 97. There was only a small variation of the overall

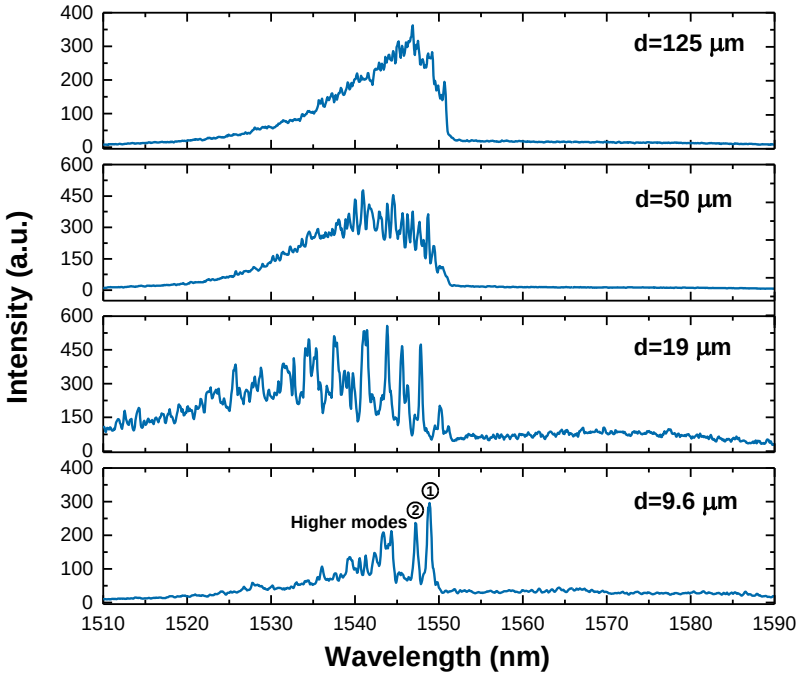

Figure 97. Reflection spectra of the air-clad SFBG under different diameters, d. All the spectra are normalized to the one of the SLED.

reflectivity with the reduction of fiber diameter. Though the power coupling efficiency from the 125 μm diameter sapphire fiber to the reduced-diameter fiber decreases approximately proportionally to the square of the reduced diameter, the relative cross section of the FBG to the fiber increases proportionally. Thus, the compensation between the weaker power coupling and stronger light-grating interaction maintains the overall reflectivity. The reflectivity variation of a certain mode was due to different modal excitation between each measurement. Besides the reflectivity, it can also be seen that the center wavelength of different modes is blue shifted with the decrease of the fiber diameter and the higher the mode order the more blue shift it will have. This is because when the fiber diameter reduces, more propagating mode energy enters the cladding region, which causes the reduction of the effective refractive index and higher modes

will have more energy outside the core. There are only a few observable peaks remaining within the SLED spectrum range when the fiber diameter is reduced to 9.6 μm, as the higher order modes have less propagating energy inside the core to interact with the grating or are no longer a guided mode. Each peak in the spectrums represents a group of degenerate modes. The rightmost two peaks are labeled as modes 1 and 2 as indicated in Figure 97. In comparison to the spectrum of the 19 μm diameter fiber, there is a strong spectrum overlap for the higher modes, which is caused by the fact that the modes in these mode groups no longer degenerate. The changes in the FBG spectra with fiber diameter are consistent with theoretical predictions and the results of the far field measurements performed in previous quarterly reports, further confirming the reduction in modal volume in the LMV fiber design.

The relative intensity between these modes was extremely sensitive to the setup configuration and/or environment variation, which causes the overall spectrum shape of these mode groups to vary easily with changes in the setup or the measurement environment and hence makes it difficult to determine the accurate peak position. Thus, for practical considerations, modes 1 and 2 were selected to demonstrate the viability of the LMV-FBGs for sensing applications. A refractive index sensor and temperature sensor were demonstrated in the past quarter.

The refractive index measurement was carried out by monitoring the reflection spectrum of the micro-SFBG immersed in air and different liquids with refractive index ranging from 1.33 to 1.75, as shown in Figure 98. After each measurement, the SFBG was cleaned in acetone by

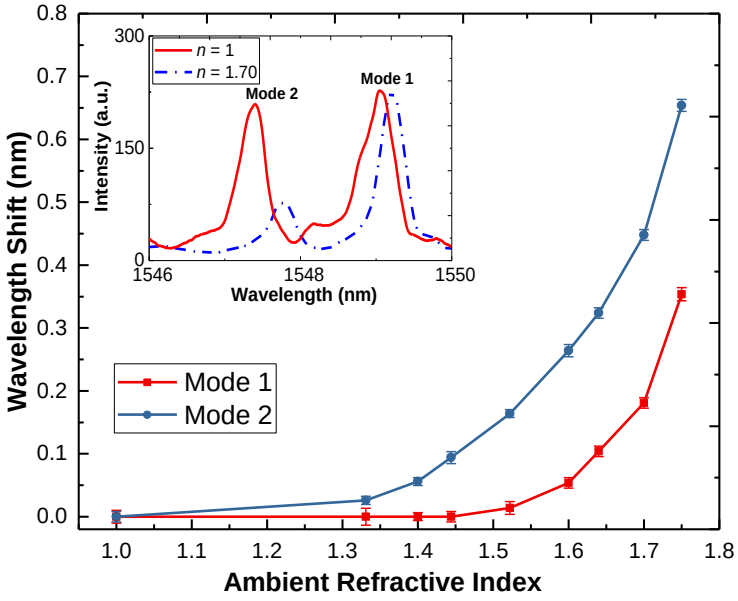

Figure 98. The shift of Bragg wavelength of the mode 1 and 2 in a 9.6 μm diameter LMV-SFBG under different ambient refractive index (plotted with error bar). The insert indicates the spectra of the two modes at ambient refractive index of 1 and 1.70.

ultrasound to remove the residual liquid. The measurement results indicate that the spectrum red shifts with the increase of ambient refractive index. It also shows the decrease of intensity of the mode 2, as less propagation energy confined in the fiber interacts with the grating. The wavelength shift for both modes are highly nonlinear and the sensitivity gets higher at larger

ambient refractive index. Since the higher-order mode has more energy in the cladding region, mode 2 has greater sensitivity to the ambient refractive index as expected. The sensitivity is evaluated by differentiating the curve in Figure 84. It approximately varies from 0.42 nm/RIU to 4.2 nm/RIU for mode 2 in the range of 1.33 to 1.75 and from 0.25 nm/RIU to 3.6 nm/RIU for mode 1 in the range of 1.44 to 1.75. The measurement range is limited by the fiber material. Owing to the inherently high refractive index of sapphire (n~1.76), the LMV-SFBG has a wider measurement range than the one fabricated in silica glass fiber (n~1.46).

5.2.3 Temperature Response of LMV Single Crystal Sapphire FBGs

The temperature dependence of the Bragg wavelength for the lowest two mode groups was investigated by placing the LMV-SFBG in a high temperature tube furnace. A B-type thermocouple was placed at the same location to monitor the temperature. The temperature was varied from room temperature to 1400°C and maintained for at least 20 minutes at each measurement step to assure the stability of the spectrum. In contrast to the refractive index measurement, the temperature dependence of the Bragg wavelength of the two mode groups are the same and nearly linear, as shown in Figure 99. The reason why the two modes share the same temperature dependence is because the temperature mainly affects the fiber itself, and even

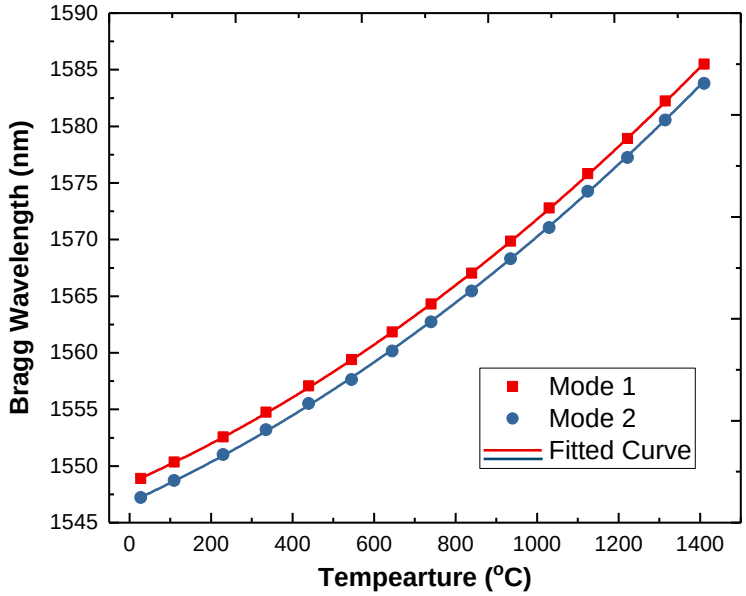

Figure 99. Temperature dependence of the Bragg wavelength of mode 1 and 2 in a 9.6 µm diameter LMV-SFBG.

though the higher order mode has a greater portion of energy outside the fiber, most of the energy is still confined in the fiber. Therefore, the modes behave the same under different temperature. The slope was determined by the therm-optic coefficient and thermal-expansion coefficient of a sapphire fiber. By applying polynomial fitting to the curves, the linear coefficient was evaluated ~26.5 pm/°C and agrees with the value reported in other references [77-79]. It is over two times larger than the one of silica glass based FBG (~10 pm/°C) near 1550 nm wavelength [2]. The result also indicates that the LMV-SFBG can operate up to at least 1400 °C.

6 FIELD DEPLOYABLE PROTOTYPE SENSING SYSTEM

6.1 Harsh Environment Sensor Packaging

The sensor packaging approach followed the design philosophies employed for single crystal sapphire fiber sensors deployed successfully in prior DOE funded projects and the commercial "tube-in-tube" fiber optic cable design for downhole fiber optic sensors. As shown in Figure 100, the sensor package consists of tube concentric high purity alumina tubes with the sensing

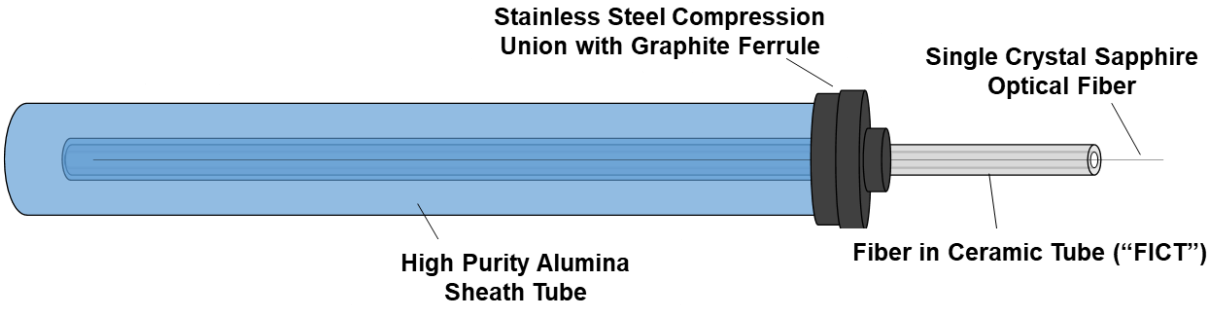

Figure 100. Schematic of Harsh Environment Sensor Packaging Design.

fiber contained in the inner tube ("fiber in ceramic tube" or "FICT") that is sheathed by a heavy walled alumina tube with a sealed end. The "tube-in-tube" sensor packaging allows for the design flexibility required for applications which must adhere to different operating requirements and geometries. As for example, the alumina inner tube can be replaced with a single crystal sapphire fiber tube for the most harsh and high temperature environments. In this sensor package design, the FICT is centralized in the outer alumina tube with a stainless steel "bore-through" compression adapter fitting. The graphite ferrule that replaces the stainless steel ferrule is soft and compliant, which is ideal for ceramic to metal connections. Although not required for every deployment, the graphite ferrule-compression fitting assembly can be utilized for requirements that require a pressure seal. The "tube-in-tube" design can also allow for additional internal tubes or filler materials in the annulus between tubes to provide additional functionality and/or reliability. The simple, robust, and flexible harsh environment sensor packaging design meets all the requirements for deployment in a wide array of harsh environments and has the design flexibility necessary for the varied deployment requirements.

6.2 Qualification of Fully Assembled Prototype Sensor

Three fiber Bragg gratings were inscribed in a 125μm-diameter air-clad single-crystal sapphire fiber (MicroMaterial Inc.) via point-by-point method with a femtosecond pulsed laser. The details of fabrication procedure are described previously and the grating configuration is shown in Figure 101. The center wavelength of the fundamental mode in the gratings are 1549.8, 1566.6, and 1584.3 nm, respectively. Each grating is ~2 mm long. Since the reflectivity of the gratings are weak, the input and the far end of the sapphire fiber was polished to 7 degree (FC/APC) and 30 degree respectively to minimize the influence from the interface Fresnel reflection. The inscribed FBGs were then annealed at 1200 °C for 10 hours to enhance and stabilize their reflectivity[5].

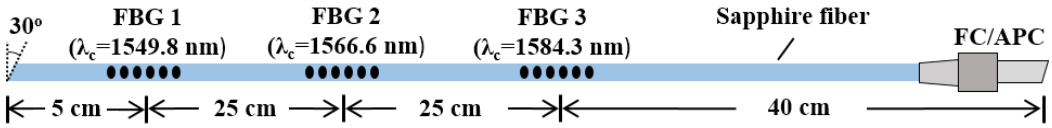

Figure 101. Configuration of the sapphire fiber Bragg grating sensors.

The sensing fiber was then packaged in a fully assembled "tube-in-tube" design as illustrated in Figure 102. The sapphire fiber was inserted in an alumina ceramic tube (ID: 1.57 mm, OD: 4.75 mm, ~950 mm long) and one end of the tube was bonded to the FC/APC connecter with epoxy (rating: 3960 psi, 300°C). This assembly was then inserted into another alumina ceramic tube (ID: 6 mm, OD: 13 mm, ~750 mm long) with one sealed end. A hole was drilled through the stainless steel compression tubing adapter to allow for the inner tube to pass through. Given the rigidity of alumina, graphite ferrules instead of stainless ones were used to centralize and "lock" the tubes in place. The details of the components are listed in Table 9.

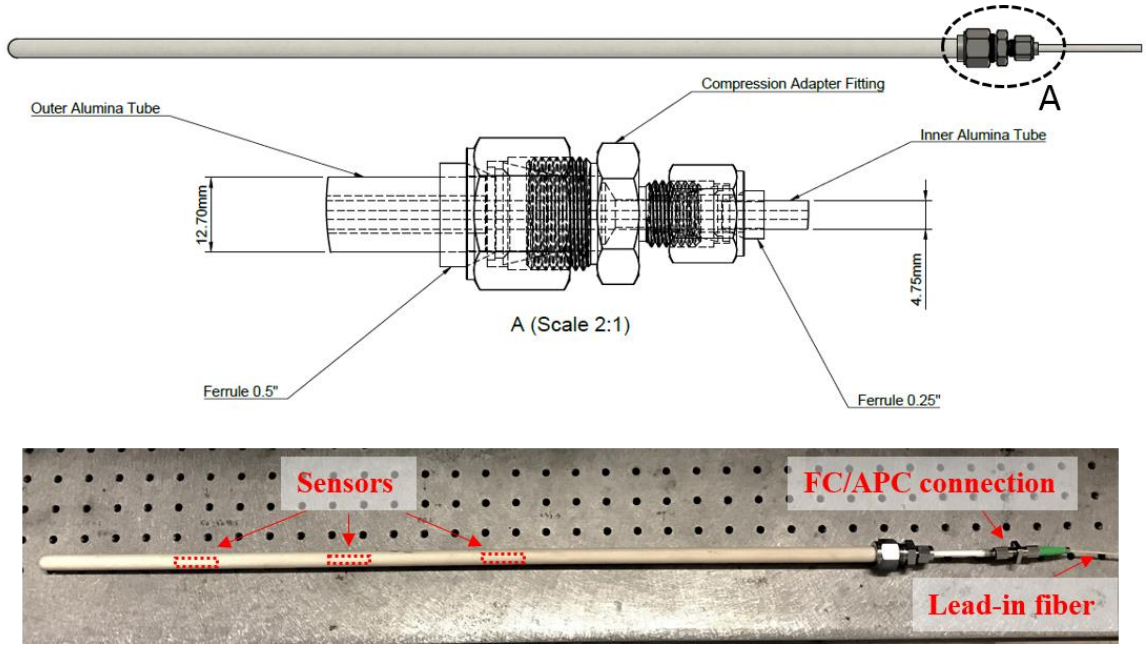

Figure 102. Mechanical drawing and picture of "tube-in-tube" design for sensors packaging.

Table 9. Description of Packaging Components

Component	Material	Dimensions	Supplier	Part#
Inner tube ("FICT")	High Purity Alumina (99.8%)	ID =1.57 mm, OD=4.75 mm	McDanel Advanced Ceramic	AXS073830
Outer tube ("Sheath")	High Purity Alumina (99.8%)	ID: 6.35 mm, OD: 12.7 mm	CoorsTek	66444
Ferrule	Graphite	1/4"	Ohio Valley Specialty	GF-03
Ferrule	Graphite	1/2"	Ohio Valley Specialty	GF-13
Compression Adapter Fitting	Stainless Steel	1/2" x 1/4"	McMaster Carr	5182K367

The packaged sensors are then calibrated and tested in the lab with the setup illustrated in Figure 103. A superluminescent light emitting diode (SLED) with a center wavelength of 1565 nm and bandwidth of 80 nm (Thorlabs S5FC1005P) was used as the illumination. Commercial step-index 105/125 μm multimode silica fiber was chosen as the lead-in fiber because it can excite sufficient number of modes into the sapphire fiber as well as has high coupling efficiency of the

reflected light. An optical spectrum analyzer (OSA) (Thorlab OSA 203) was used to record the grating signals. The sensors were inserted into a tube furnace (Sentro Tech Corp., STT-1600C-3.5-12) for calibration and the results are shown in Figure 103. Due to the multimode nature of the sapphire fiber, curve fitting with Gaussian model was used to deduce the position of the broad reflection peaks as shown in the insert of Figure 103. The sensors show great linearity in the range from room temperature to 1200°C with a fitted linear coefficient of ~25 pm/°C.

After the calibration, the durability of the packaged sensors was tested by being exposed to a temperature of 1000 °C for 110 hours and its performance was evaluated every 15 minutes. All the spectra are normalized to the SLED and the ripples in the reflection peaks varied during the

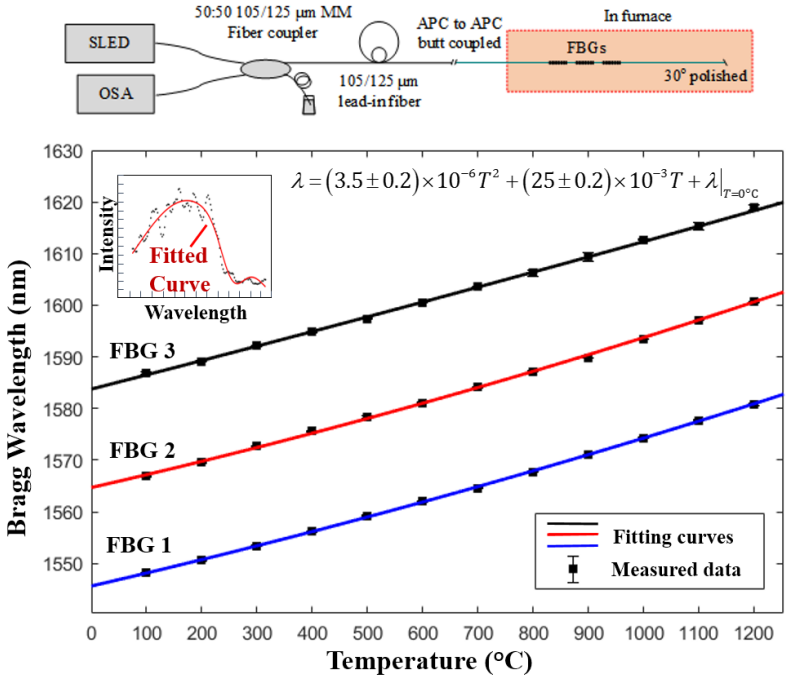

Figure 103. Schematic of sensor calibration test set-up and temperature response of the FBGs.

test due to different modal excitation, which is highly sensitive to the environment, as shown in Figure 104. The instabilities in the overall spectrum shape arose from variation of modal excitation are most evident upon heating at the beginning of the test (<10 hours). The temperature measurements were relatively stable over the duration of the test, as shown in Figure 105. The mean and standard deviation of the measured temperature after the first 10 hours were: FBG 1: T_{mean} =989.6°C, σ = 8.43 °C, FBG 2: T_{mean} =890.7°C, σ = 5.99°C, FBG 3: T_{mean} =715.9°C, σ = 4.91°C. The difference between the maximum furnace temperature (1000°C) and the FBG 1 (989.6°C) arises because there is a temperature offset between the position of the thermocouple and FBG sensor. The distributed measurement capability of the FBG sensor array was also verified by the characterization of the known thermal gradient in the furnace.

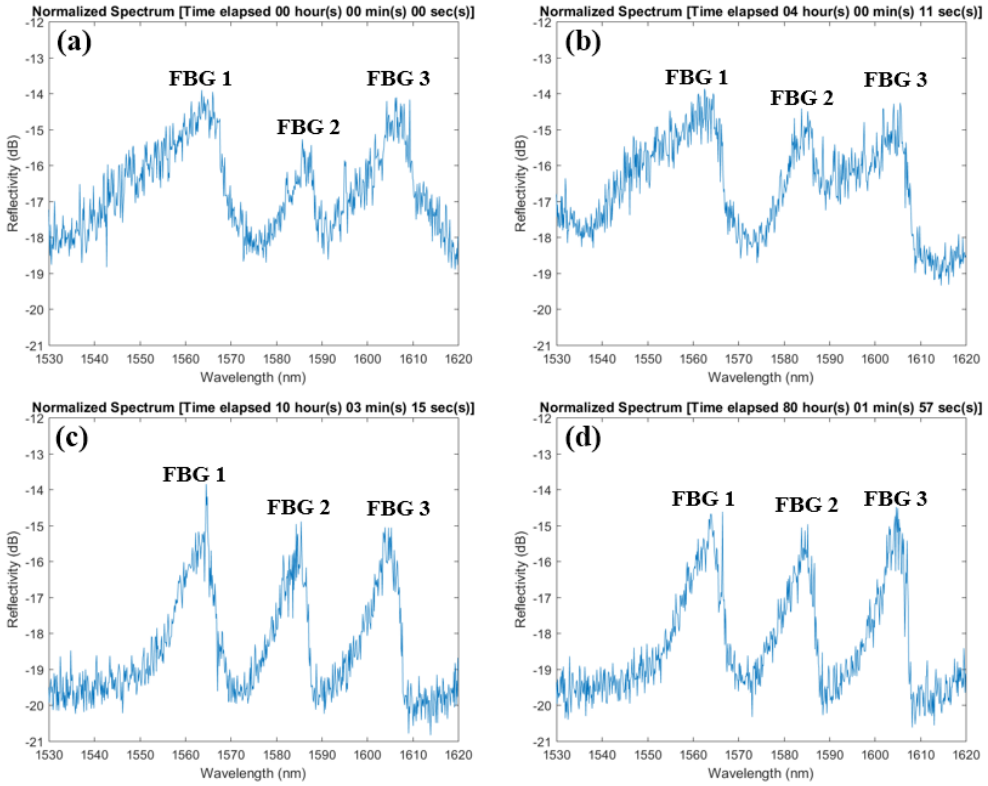

Figure 104. Evolution of normalized FBG spectra at different time: (a) beginning (b) 4 hours (c) 10 hours (d) 80 hours.

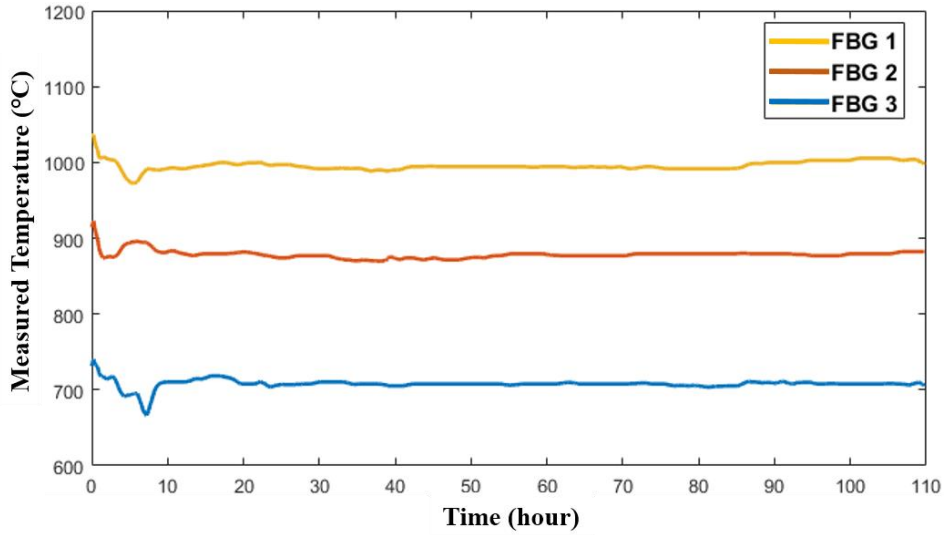

Figure 105. Time evolution of the measured temperature from the FBG sensors during the 110 hour isothermal test.

7 FIELD TRIAL TESTING OF PROTOTYPE SENSING SYSTEM

7.1 Field Trial Test Site: Virginia Tech Power Plant

Field trial testing of prototype sensing systems were conducted in a coal-fired boiler and gas-fired boiler at the Central Steam Plant at Virginia Tech. The power plant, as shown in Figure 106, generates an annual steam output greater than 943 billion BTUs. The 6,250-kilowatt,

(a) **(b)**

Figure 106. (a) Central Steam Plant at Virginia Tech. (b) Gas-fired boiler at the VT Power Plant.

12,470-volt steam-turbine-powered generator produces nearly 27 million kilowatt-hours of electricity annually. To meet these demands, the plant operates five boilers, each outfitted with superheaters rated at 80,000 or 100,000 pounds of steam per hour. In addition, the plant's efficiency is tracked using a Continuous Emissions Monitoring System, and the coal-burning boilers are equipped with scrubber and bag-house systems that control particulate and acid-gas emissions. The Virginia Tech Power Plant ("Virginia Tech Electric Services") also sells electricity at retail prices to 6,000 residential customers in Blacksburg, VA. The close proximity of the research team to the power plant facilities on the main campus of Virginia Tech was a unique opportunity to streamline and accelerate the field testing of the prototype sensing system. The research team at CPT collaborated with operations team at the VT Power Plant to retrofit access points on the boilers for the flawless installation of the sensors into the operating boilers.

7.2 First Field Trial: Coal-Fired Boiler

The packaged sensors and interrogation system was installed in a commercial coal-fired boiler in Virginia Tech Central Steam Plant. A commerically available K-type thermocouple housed in an alumina tube was installed near the location of FBG 1 at the same time to provide a temperature reference. Installation of the sensor and thermocouple did not require a shutdown of the boiler and/or special accomodations. Sensor deployment was performed seamlessly in a period of approximately 2 hours. As shown in Figure 107, the sensor was installed and position nearest to the boiler hot zone for maximum temperature exposure. An inlet hole cap on the boiler was modified to include two ports with welded stainless steel compression fittings for the fiber optic sensor and a thermocouple as shown in the insert of Figure 107, FBG 1 is closer to the flame and FBG 3 is located near the boiler wall. The onsite sensing intorrogation system, illustrated in Fig. 3, was packaged in a dust-proof enclosure. The measurement results were monitored remotely in real time through wireless internet connection.

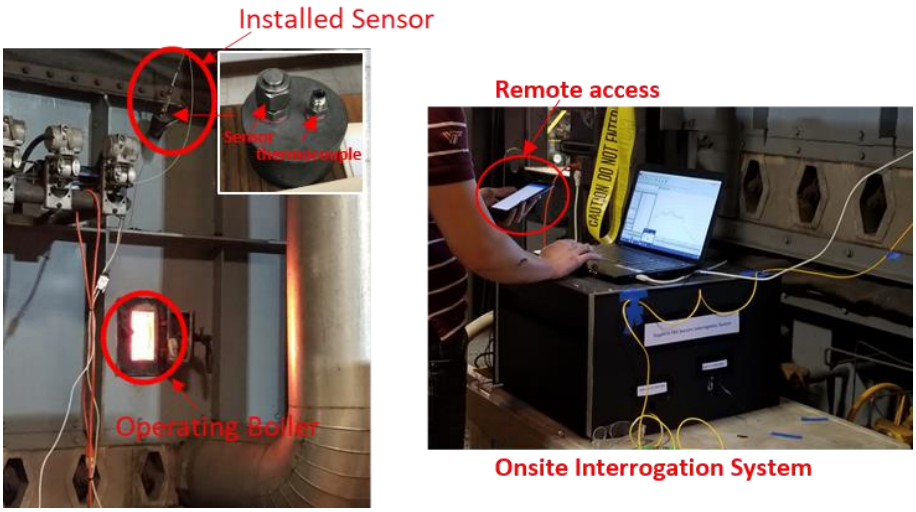

Figure 107. Sensor deployment and the onsite interrogation system.

The sensing system has been operating for over 42 days and experienced a peak temperature of ~ 700°C. A desired peak temperature of 1000°C was not reach due to the limited demand on boiler because of the unseasonably mild climate that coincided with the field trial. The temperature gradient within the boiler can be readily seen by the temperature measurements provided by the three FBGs, as shown in Figure 108. Furthermore, the prototype sensor measurements were consistent with those provided by the thermocouple co-located with FBG 1. The drop in the temperature readings at approximately 120 hours until 180 hours was due to loss of power to the light source and was easily remedied by returning power to the unit. The drop in the temperature readings for ~14 days was due to damage to the interrogation system and components that appeared to be due to the local environment and unexpected handling by the operational team.

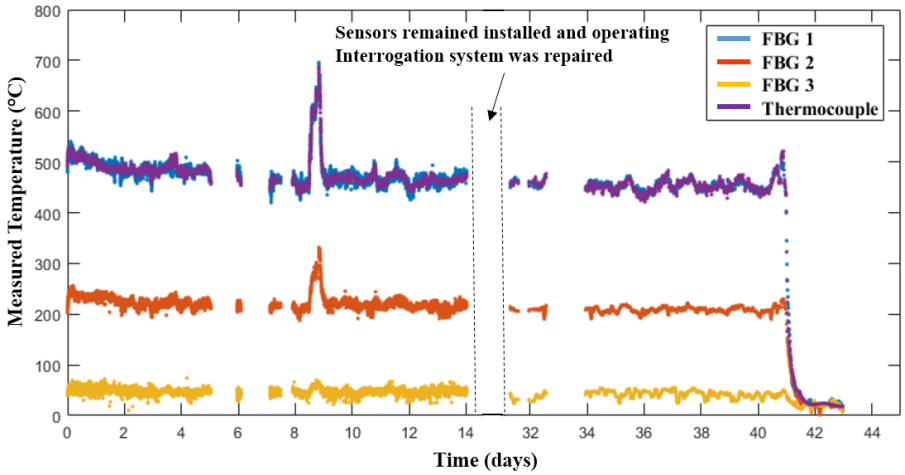

Figure 108. Temperature response of the FBG sensors over 42 days

Upon completion of the successful field trial, "The Lessons Learned" and associated "Action Plans" were developed, as shown in Table 10. The system improvements and the ruggedization of identified components were integrated for the deployment of a prototype sensing system in a gas-fired boiler in a second field trial**.**

Table 10. Field Trial #1: Lessons Learned and Action Plan

#	Lesson Learned	Action
1	Sporadic shutdown of the optical interrogator due to accumulation of particulates	Design and construct sealed enclosure
2	Several attempts were required to insert sensor through fitting	Conduct a thorough review of all structures in the immediate deployment area
3	Relatively fragile optical components	Ruggedize all components external to the installed sensor
4	Breakage of lead-in fiber due unwarranted contact by members of the operations team	Utilize tight buffered fiber optic cables Implement proper protection of the deployed system and appropriate signage
6	Damage of sensor assembly upon boiler shutdown and cleaning	Remove sensor immediately upon completion of field test and prior to boiler cleaning operations

7.3 Second Field Trial: Gas-Fired Boiler

7.3.1 System Ruggedization and Upgrades

Several system upgrades, based upon the lessons learned from the first field trial, were integrated into the sensing system to improve reliability and performance. As shown in Figure 109(a), the "transition end" of the probe was constructed with off-the-shelf stainless-steel tubes and compression fittings. The male FO connector fitting on this end of the probe, as shown in Figure 109(b), will eliminate the need for on-site splices and simplifies the installation process for the sensor probe. The sensor lead-in fiber and transmission fiber were encapsulated with corrugated stainless steel tubing to improve handleability upon deployment and reliability during operation in a fossil fuel energy generation facility, as shown in Figure 109(c) and Figure 109(d),

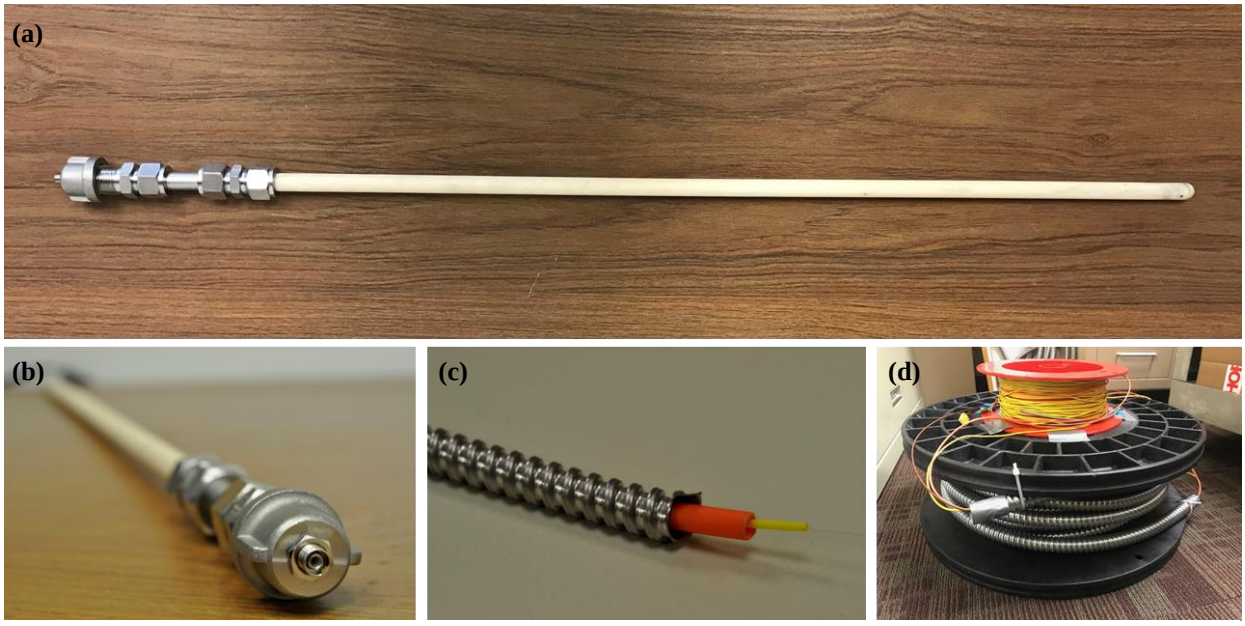

Figure 109. (a) Prototype temperature sensing probe with harsh environment packaging with stainless steel transition assembly; (b) Female fiber optic connector on the inlet end off the sensing probe; (c) Corrugated stainless steel buffer tube; (d) 20 meter connecting fiber encapsulated in corrugated stainless steel tubing and spool of extension fiber for the optical interrogator.

respectively. The transmission cable included 20 meters of standard single mode fiber (SMF28), a pure silica core step index multimode fiber, and thermocouple extension wire. Specifically, the communication link between the prototype sensor probe and interrogator was custom patch cable, FG105LCA, acquired from Thorlabs connectorized with FC/APC on both ends.

"User-friendly" interfaces were developed, via LabView, for use by sensor engineers and end-users (operators). As shown in Figure 110(a), real-time diagnostics can be performed for the temperature probe. Relevant information such as the raw and filtered sensor spectral response and peak fitting parameters are readily accessible for tuning and trouble-shooting. An additional interface was developed to provide temperature measurements for monitoring the operation of the boiler. As show in Figure 110(b), a schematic of the temperature probe along with position of each sensor provides the user with spatial data that can be utilized for temperature mapping.

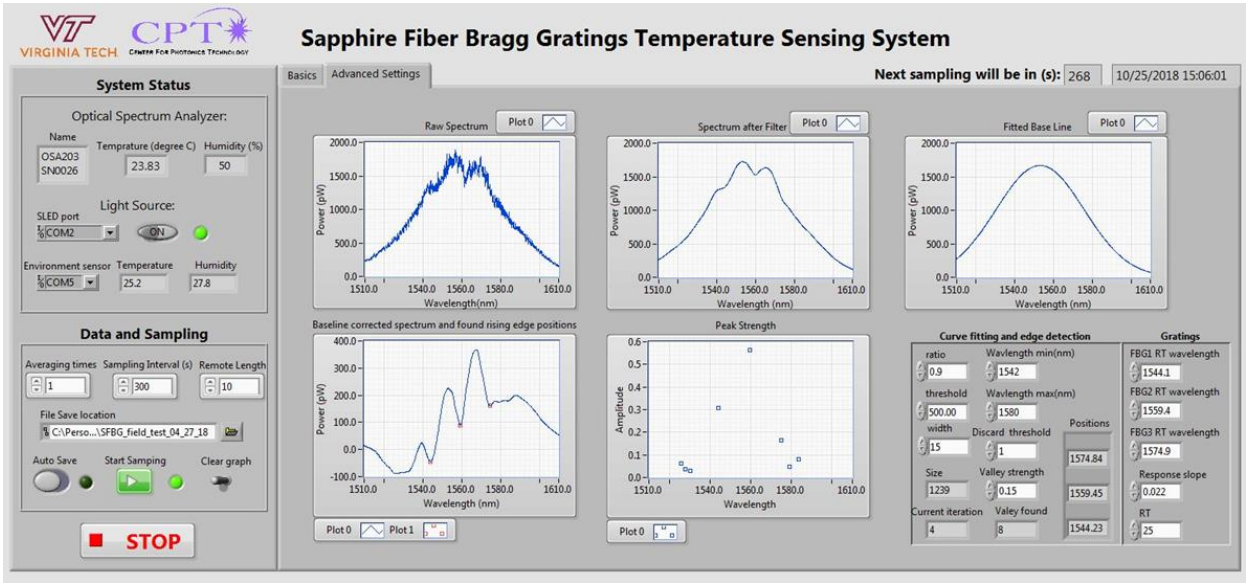

(a)

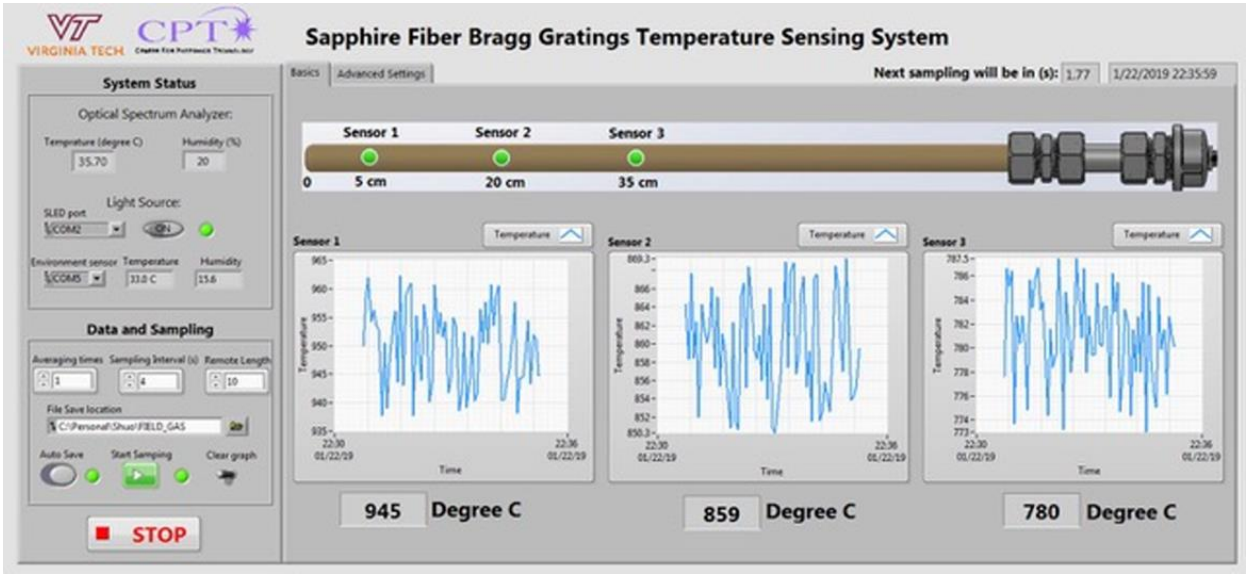

(b)

Figure 110. "User-friendly" interface for (a) sensor diagnostics and (b) temperature monitoring.

7.3.2 Sensing System Deployment and Operation

The sensing system was successfully installed in a gas fiber boiler with relative ease with assistance from the VT Power Plant team. As shown in Figure 111(a, b), the ruggedized transmission cable was routed on a cable tray extending from the interrogator to the installed temperature probe. The interrogator was housed located in a pre-existing cabinet at a distance of ~15 meters from the temperature probe, as shown in Figure 112(a) and 112(b), respectively. The installation was completed successfully in less than 2 hours.

(a) (b)

Figure 111. (a) Deployed sensor transmission cable and (b) installed sensor probe.

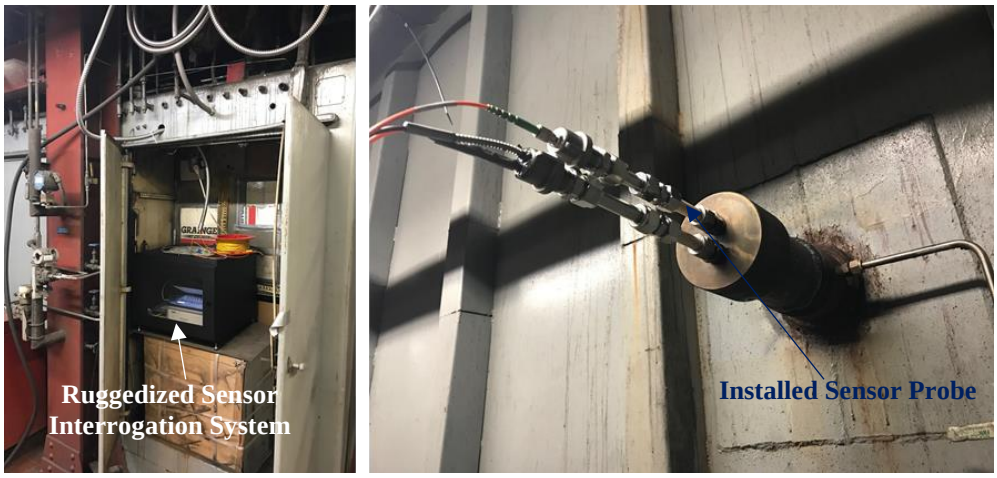

(a) (b)

Figure 112. (a) Interrogation system components in the enclosure and (b) inlet connection for the installed temperature probe.

Upon installation, the temperature probe operated successfully for a period of approximately 2 months, as shown in Figure 5(a). The average temperature response for FBG1, FBG2, and FBG3, were ~795ºC, ~749ºC, and ~671°C, respectively. The thermocouple, positioned near FBG1, measured an average temperature of ~795°C. The response of FBG1 and FBG2 were

maintained at temperatures in excess of 900°C for several different durations during operation and excursions above 1000°C were observed for FBG2. In addition, applications were developed for mobile devices, such as i-Pads, to monitor the temperature response of each FBG in the temperature probe, as shown in Figure 113(b).

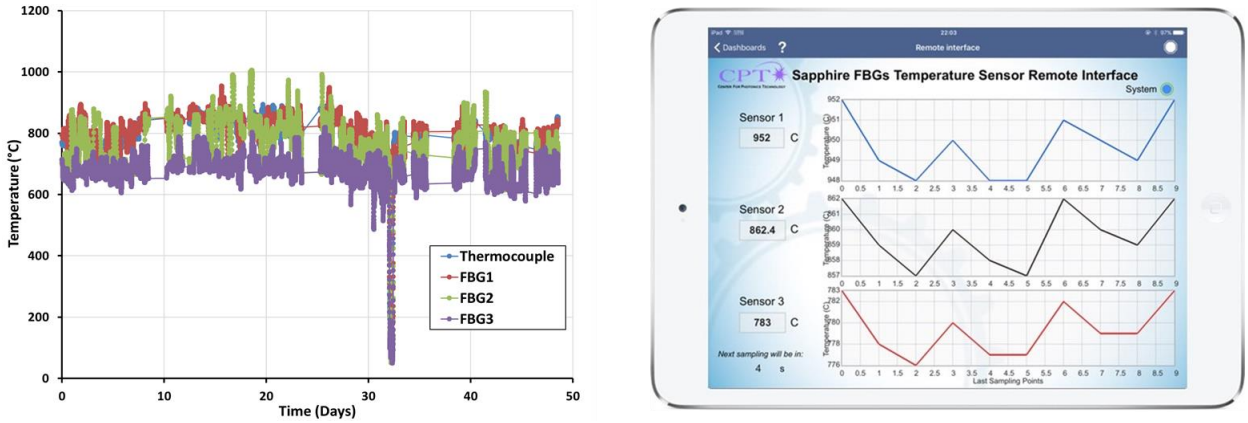

(a) **(b)**

Figure 113. (a) Temperature response of prototype temperature probe and (b) temperature monitoring app.

The prototype sensor and sensing system were retrieved on January 23, 2019 with assistance from the Power Plant team. "Break-down" of the equipment and components was completed in less than 2 hours without incident. Upon removal from the cabinet, it was evident that the enclosure protected the interrogation equipment from the surrounding environment, as shown in Figure 114(a). In addition, the temperature probe remained intact upon removal from the gas-fired boiler, as shown in Figure 114(b). Discoloration of the alumina sleeve tube was evident on the end of the probe, as shown in the insert. A red color was evident on the end of the probe which was exposed to the highest temperatures in the boiler, but no mechanical degradation was observed.

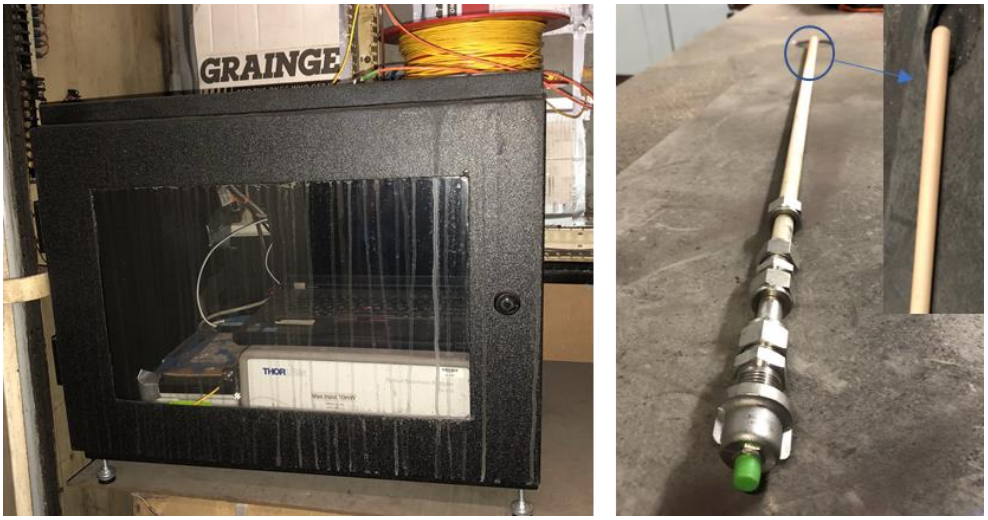

(a) **(b)**

Figure 114. (a) Observed debris on interrogator enclosure and (b) retrieved temperature probe with discoloration observed on the high temperature end.

8 CONCLUSIONS AND FUTURE WORK

In this program, we developed a waveguide structure and the associated processing techniques for the fabrication of a low modal volume single crystal sapphire optical fiber. A fully distributed Raman backscatter temperature sensing system was demonstrated for the first time with single crystal sapphire fibers. A quasi-distributed temperature sensing system was developed with the use of fiber Bragg gratings (FBGs) fabricated in single crystal sapphire fibers via the point-by-point method. A novel fiber-in-ceramic tube (FICT) harsh environment sensor package was developed for successful deployment and operation of prototype sensing systems installed in a coal-fired boiler and gas-fired boiler in a commercial power plant at Virginia Tech. The harsh environment quasi-distributed temperature sensing technology was advanced from a (Technology Readiness Level) TRL=1 to a TRL=7 by demonstrating the full validation of the sensing system prototype in a relevant industrial environment.

A significant number of technical achievements were accomplished upon completion of the project. Several technologies and techniques were demonstrated for the first time to include (1) the fabrication of sub-micron single crystal sapphire fiber, (2) observation of Raman Stokes and Anti-Stokes peaks in single crystal sapphire optical fiber, (3) fabrication of FBGs in sapphire fiber via the point-by-point method, (4) measurement of fiber attenuation in the time domain in sapphire, (5) distributed Raman temperature measurements in sapphire fiber and (6) demonstration of few to single mode operating in a single crystal sapphire optical fiber. The applicability of the technologies was demonstrated via the full integration and ruggedization of a prototype sensing system for the successful installation in operating commercial coal-fired and gas-fired boiler systems.

The research products generated from this five-year project lay a strong foundation for the integration of the technologies into larger scale commercial boiler systems to advance to a TRL=8. The core fiber optic sensing technologies and packaging schemes provide an opportunity for application in other energy generation systems and harsh environments. Future work dedicated toward advancing the TRL and identifying additional applications of the technology is anticipated to provide great benefit to the scientific and industrial community.

The original goal of the project was project was to develop the next generation of harsh environment sensing systems. After successfully completing the original scope, the project was expanded and extended to allow for the successful development of harsh environment packaging and testing field testing of prototype sensing systems. The real-time, accurate and reliable monitoring of temperatures at distributed locations is expected to lower operating costs by allowing more accurate measurement of the harsh conditions inside a boiler system to better control its operation. The technologies developed by Virginia Tech's Center for Photonics Technology will support the mission of the National Energy Technology Laboratory (NETL) to advance energy options to fuel our economy, strengthen our security, and improve the environment.

9 REFERENCES

1. Hill, Cary, Daniel Homa, Bo Liu, Zhihao Yu, Anbo Wang, and Gary Pickrell. "Submicron diameter single crystal sapphire optical fiber." Materials Letters 138 (2015): 71-73.

2. Liu, Bo, Zhihao Yu, Cary Hill, Yujie Cheng, Daniel Homa, Gary Pickrell, and Anbo Wang. "Sapphire-fiber-based distributed high-temperature sensing system." Optics letters 41, no. 18 (2016): 4405-4408.

3. Liu, Bo, Zhihao Yu, Zhipeng Tian, Daniel Homa, Cary Hill, Anbo Wang, and Gary Pickrell. "Temperature dependence of sapphire fiber Raman scattering." *Optics letters* 40, no. 9 (2015): 2041-2044.

4. Cheng, Yujie, Cary Hill, Bo Liu, Zhihao Yu, Haifeng Xuan, Daniel Homa, Anbo Wang, and Gary Pickrell. "Modal reduction in single crystal sapphire optical fiber." Optical Engineering 54, no. 10 (2015): 107103.

5. Yang, Shuo, Daniel Homa, Gary Pickrell, and Anbo Wang. "Fiber Bragg grating fabricated in micro-single-crystal sapphire fiber." Optics letters 43, no. 1 (2018): 62-65.

6. Hill, Cary, Dan Homa, Zhihao Yu, Yujie Cheng, Bo Liu, Anbo Wang, and Gary Pickrell. "Single Mode Air-Clad Single Crystal Sapphire Optical Fiber." *Applied Sciences* 7, no. 5 (2017): 473.

7. Cheng, Yujie, Cary Hill, Bo Liu, Zhihao Yu, Haifeng Xuan, Daniel Homa, Anbo Wang, and Gary Pickrell. "Design and analysis of large-core single-mode windmill single crystal sapphire optical fiber." *Optical Engineering* 55, no. 6 (2016): 066101.

8. Yang, Shuo, Di Hu, and Anbo Wang. "Point-by-point fabrication and characterization of sapphire fiber Bragg gratings." Optics letters 42, no. 20 (2017): 4219-4222.

9. Liu, Bo, Michael P. Buric, Benjamin T. Chorpening, Zhihao Yu, Daniel S. Homa, Gary R. Pickrell, and Anbo Wang. "Design and Implementation of Distributed Ultra-High Temperature Sensing System With a Single Crystal Fiber." *Journal of Lightwave Technology* 36, no. 23 (2018): 5511-5520.

10. Liu, B., M. Buric, B. Chorpening, A. Wang, Z. Yu, D. Homa, Y. Cheng, C. Hill, and G. Pickrell. "Attenuation measurements in single-crystal sapphire fiber via Raman scattering intensity." In *Optical Components and Materials XV*, vol. 10528, p. 105280U. International Society for Optics and Photonics, 2018.

11. Shuo Yang, Daniel Homa, Hanna Heyl, Logan Theis, John Beach, Billy Dudding, Glen Acord, Dwyn Taylor, Gary Pickrell, Anbo Wang. "Commercial Boiler Test for Distributed Temperature Sensor Based on Wavelength-Multiplexed Sapphire Fiber Bragg Gratings", SPIE Defense and Commercial Sensing 2019.

12. Lockwood, T. "Advanced sensors and smart controls for coal-fired power plant controls for coal-fired power plant." Report No. 251 (2015).

13. Richardson, Aileen, Dale Keairns, and Briggs White. "The role of sensors and controls in transforming the energy landscape." In Micro-and Nanotechnology Sensors, Systems, and Applications X, vol. 10639, p. 106390Y. International Society for Optics and Photonics, 2018.

14. Zhang, Yibing, Gary R. Pickrell, Bing Qi, Ahmad Safaai-Jazi, and Anbo Wang. "Single-crystal sapphire-based optical high-temperature sensor for harsh environments." Optical Engineering 43, no. 1 (2004): 157-165.

15. Mihailov, Stephen J., Dan Grobnic, and Christopher W. Smelser. "High-temperature multiparameter sensor based on sapphire fiber Bragg gratings." *Optics letters* 35, no. 16 (2010): 2810-2812.

16. Chen, Hui, Michael Buric, Paul R. Ohodnicki, Jinichiro Nakano, Bo Liu, and Benjamin T. Chorpening. "Review and perspective: Sapphire optical fiber cladding development for harsh environment sensing." Applied Physics Reviews 5, no. 1 (2018): 011102.

17. US Energy Information Administration, Monthly Review Monthly Energy Review, Table 6.2, May 2018.

18. Act, Energy Policy. "Energy policy act of 2005." In US Congress. 2005.

19. Nubling RK, Kozodoy RL, Harrington JA. Optical properties of clad and unclad sapphire fiber. OE/LASE'94: International Society for Optics and Photonics; 1994. p. 56-61.

20. Jiang H, Cao Z, Yang R, Yuan L, Xiao H, Dong J. Synthesis and characterization of spinel MgAl2O4 thin film as sapphire optical fiber cladding for high temperature applications. Thin Solid Films. 2013;539:81-

21. Janney MA, May RG, Nunn SD. Cladding for high temperature optical component and method of making same. US Patent 20,040,208,470; 2004.

22. Desu SB, Claus RO, Raheem R, Murphy KA. High-temperature sapphire optical sensor fiber coatings. Orlando'90, 16-20 April: International Society for Optics and Photonics; 1990. p. 2-9.

23. Pfeiffenberger NT, Pickrell GR. Modal reduction in 6-rod bundled single-crystal sapphire photonic crystal fibers. SPIE Defense, Security, and Sensing: International Society for Optics and Photonics; 2012. p. 837004--8.

24. Shen Y, Tong L, Chen S. Performance stability of the sapphire fiber and cladding under high temperature. Photonics East'99: International Society for Optics and Photonics; 1999. p. 134-42.

25. Byer, Robert L., and Martin M. Fejer. "Apparatus for growing crystal fibers." U.S. Patent 4,421,721, issued December 20, 1983.

26. Phomsakha, Vongvilay, Robert SF Chang, and Nicholas I. Djeu. "Growing crystalline sapphire fibers by laser heated pedestal techiques." U.S. Patent 5,607,506, issued March 4, 1997.

27. Reisman, A., M. Berkenblit, J. Cuomo, and S. A. Chan. "The chemical polishing of sapphire and MgAl spinel." Journal of The Electrochemical Society 118, no. 10 (1971): 1653-1657.

28. Ridley, Moira K., David J. Wesolowski, Donald A. Palmer, Pascale Bénézeth, and Richard M. Kettler. "Effect of sulfate on the release rate of Al3+ from gibbsite in low-temperature acidic waters." Environmental science & technology 31, no. 7 (1997): 1922-1925.

29. Stachel, Doerte, Ingrid Svoboda, and Hartmut Fuess. "Phosphorus pentoxide at 233 K." Acta Crystallographica Section C: Crystal Structure Communications 51, no. 6 (1995): 1049-1050.

30. Dwikusuma, F., D. Saulys, and T. F. Kuech. "Study on sapphire surface preparation for III-nitride heteroepitaxial growth by chemical treatments." Journal of The Electrochemical Society 149, no. 11 (2002): G603-G608.

31. Lee, Ya-Ju, Hao-Chung Kuo, Tien-Chang Lu, Shing-Chung Wang, Kar Wai Ng, Kei May Lau, Zu-Po Yang, Allan Shih-Ping Chang, and Shawn-Yu Lin. "Study of GaN-based light-emitting diodes grown on chemical wet-etching-patterned sapphire substrate with V-shaped pits roughening surfaces." Journal of lightwave Technology 26, no. 11 (2008): 1455-1463.

32. Marasina, L. A., V. V. Malinovsky, I. G. Pichugin, and P. Prentky. "Chemical etching of sapphire." Crystal Research And Technology 17, no. 3 (1982): 365-371.

33. Aota, Natsuko, Hideo Aida, Yutaka Kimura, Yuki Kawamata, and Michio Uneda. "Fabrication Mechanism for Patterned Sapphire Substrates by Wet Etching." ECS Journal of Solid State Science and Technology 3, no. 5 (2014): N69-N74.

34. Vardiman, R. G. "The chemical polishing and etch pitting of sapphire." Journal of The Electrochemical Society 118, no. 11 (1971): 1804-1809.

35. Dobrovinskaya, Elena R., Leonid A. Lytvynov, and Valerian Pishchik. Sapphire: material, manufacturing, applications. Springer Science & Business Media, 2009.

36. Wang, Jing, L. W. Guo, H. Q. Jia, Y. Wang, Z. G. Xing, W. Li, H. Chen, and J. M. Zhou. "Fabrication of patterned sapphire substrate by wet chemical etching for maskless lateral overgrowth of GaN." Journal of the Electrochemical Society 153, no. 3 (2006): C182-C185.

37. Hecht, J., Understanding Fiber Optics. 1999: Prentice Hall.

38. CORNING, Numerical Aperture Measurement Method. 2001.

39. Yeung, Anson Chi-Ming. "Polymer Segmented Cladding Fibres: Cross Fibre Modelling, Design, Fabrication and Experiment." The University of New South Wales, 2009.

40. Chen, Ming-Yang, Yong-Kang Zhang, Xiao-Xia Fu, Bing Sun, and Jun Zhou. "Proposal and Design of Sectorial Cladding Optical Fibre for Large-Mode-Area, Single-Mode Operation." Journal of Optics 12, no. 5 (2010): 055403.

41. Rastogi, V., and K. S. Chiang. "Leaky Optical Fibre for Large Mode Area Singlemode Operation." Electronics Letters 39, no. 15 (2003): 1110.

42. Sotsky, A. B., O. A. Bel'skaya, and L. I. Sotskaya. "Higher-Order Modes of Photonic-Crystal Fibers." Optics and Spectroscopy 110, no. 3 (2011): 432-37.

43. Rastogi, Vipul, and Kin Seng Chiang. "Propagation Characteristics of a Segmented Cladding Fiber." Optics letters 26, no. 8 (2001): 491-93.

44. Yeung, A, K S Chiang, V Rastogi, P L Chu, and G D Peng. "Experimental Demonstration of Single-Mode Operation of Large-Core Segmented Cladding Fiber." Paper presented at the Optical Fiber Communication Conference, 2004.

45. Kumar, Ajeet, and Vipul Rastogi. "Design and Analysis of a Multilayer Cladding Large-Mode-Area Optical Fibre." Journal of Optics A: Pure and Applied Optics 10, no. 1 (2008): 015303.

46. Chiang, Kin S, and Vipul Rastogi. "Ultra-Large-Core Single-Mode Fiber for Optical Communications: The Segmented Cladding Fiber." Paper presented at the Optical Fiber Communication Conference and Exhibit, 2002. OFC 2002, 2002.

47. Silvestre, E, P St J Russell, TA Birks, and JC Knight. "Analysis and Design of an Endlessly Single-Mode Finned Dielectric Waveguide." JOSA A 15, no. 12 (1998): 3067-75.

48. Chiang, Kin S. "Radial Effective-Index Method for the Analysis of Optical Fibers." Applied optics 26, no. 15 (1987): 2969-73.

49. J.-M.Jin, The Finite Element Method in Electromagnetic, 3rd ed., Wiley-IEEE Press (2014).

50. R. E.Setchell, "Refractive index of sapphire at 532 nm under shock compression and release," J. Appl. Phys.91(5), 2833–2841 (2002).

51. K.Saitohet al., "Chromatic dispersion control in photonic crystal fibers: application to ultra-flattened dispersion," Opt. Express11, 843–852 (2003).

52. K.Saitoh and M.Koshiba, "Leakage loss and group velocity dispersion in air-core photonic bandgap fibers," Opt. Express11, 3100–3109 (2003).

53. T. P.Whiteet al., "Confinement losses in microstructured optical fibers," Opt. Lett.26, 1660–1662 (2001).

54. D.Ferrariniet al., "Leakage properties of photonic crystal fibers," Opt. Express10, 1314–1319 (2002).

55. S.Guoet al., "Loss and dispersion analysis of microstructured fibers by finite-difference method," Opt. Express12, 3341–3352 (2004).

56. P.Berenger, "A perfectly matched layer for the absorption of electromagnetic waves," J. Comput. Phys.114, 185–200 (1994)

57. K.Saitohet al., "Chromatic dispersion control in photonic crystal fibers: application to ultra-flattened dispersion," Opt. Express11, 843–852 (2003)

58. M. Hobel, J. Ricka, "High-resolution distributed temperature sensing with the multiphoton-timing technique", Applied optics, Vol. 34, No. 16, (1995).

59. B. L. Danielson, "Optical fiber characterization," Natl. Bur. Stand. (U.S.) Spec. Publ.637 (1982)

60. B. Culshaw and J. Dakin, Optical Fiber Sensors Vol. 2: Systems and Applications (Artech House, Norwood, Mass, 1989)

61. J. P. Dakin, D. J. Pratt, G. W. Bibby, and J. N. Ross, "Temperature distribution measurement using Raman ratio thermometry," in Fiber Optic and Laser Sensors III, E.L. Moore and O. G. Ramer, eds., Proc. Soc. Photo-Opt, Instrum. Eng. 566, 249-256, (1985).

62. G. H. Watson, Jr. and W. B. Daniels, "Measurements of Raman Intensities and pressure dependence of phonon frequencies in sapphire", J. Appl. Phys. 52(2), (1981).

63. Cody Raml, Xiangnan He, Ming Han, Dennis R. Alexander, and Yongfeng Lu, “Raman spectroscopy based on a single-crystal sapphire fiber”, Optics Letters, Vol. 36, Issue 7, pp. 1287-1289 (2011).

64. Ashkin, M., J. H. Parker Jr, and D. W. Feldman. "Temperature dependence of the Raman lines of α-Al2O3." Solid state communications 6, no. 6 (1968): 343-346.

65. A. Polley and S. E. Ralph, "Raman amplification in multimode fiber," Photonics Technology Letters, IEEE 19, 218-220 (2007).

66. G. Agrawal, Nonlinear fiber optics, 5th ed. (2013).

67. Höbel, M., J. Ricka, M. Wüthrich, and Th Binkert. "High-resolution distributed temperature sensing with the multiphoton-timing technique." Applied optics 34, no. 16 (1995): 2955-2967.

68. Soto, Marcelo A., Tiziano Nannipieri, Alessandro Signorini, Andrea Lazzeri, Federico Baronti, Roberto Roncella, Gabriele Bolognini, and Fabrizio Di Pasquale. "Raman-based distributed temperature sensor with 1 m spatial resolution over 26 km SMF using low-repetition-rate cyclic pulse coding." *Optics letters* 36, no. 13 (2011): 2557-2559.

69. Liao, C. R., and D. N. Wang. "Review of femtosecond laser fabricated fiber Bragg gratings for high temperature sensing." Photonic Sensors 3, no. 2 (2013): 97-101.

70. Kashyap, Raman. Fiber bragg gratings. Academic press, 2009.

71. Canning, John, Michael Stevenson, Somnath Bandyopadhyay, and Kevin Cook. "Extreme silica optical fibre gratings." Sensors 8, no. 10 (2008): 6448-6452.

72. Grobnic, Dan, Christopher W. Smelser, Stephen J. Mihailov, and Robert B. Walker. "Long-term thermal stability tests at 1000 C of silica fibre Bragg gratings made with ultrafast laser radiation." Measurement Science and Technology 17, no. 5 (2006): 1009.

73. Mihailov, Stephen J. "Fiber Bragg grating sensors for harsh environments." Sensors 12, no. 2 (2012): 1898-1918.

74. Ciattoni, Alessandro, and Claudio Palma. "Optical propagation in uniaxial crystals orthogonal to the optical axis: paraxial theory and beyond." *JOSA A* 20, no. 11 (2003): 2163-2171.

75. Li, Jiang, Hongbing Jiang, Jun Xiao, and Qihuang Gong. "The mechanism of multi-focusing of lasers into uniaxial crystals." Journal of Optics A: Pure and Applied Optics 9, no. 7 (2007): 664.

76. Deng, Leimin, Peng Liu, Jun Duan, Xiaoyan Zeng, Baoye Wu, and Xizhao Wang. "Numerical simulation of laser focusing properties inside birefringent crystal." Applied optics 55, no. 4 (2016): 853-860.

77. Busch, Matthias, Wolfgang Ecke, Ines Latka, Daniel Fischer, Reinhardt Willsch, and Hartmut Bartelt. "Inscription and characterization of Bragg gratings in single-crystal sapphire optical fibres for high-temperature sensor applications." Measurement Science and Technology 20, no. 11 (2009): 115301.

78. Mihailov, Stephen J., Dan Grobnic, Christopher W. Smelser, Ping Lu, Robert B. Walker, and Huimin Ding. "Induced Bragg gratings in optical fibers and waveguides using an ultrafast infrared laser and a phase mask." Laser Chemistry 2008 (2008).

79. Elsmann, Tino, Tobias Habisreuther, Albrecht Graf, Manfred Rothhardt, and Hartmut

Bartelt. "Inscription of first-order sapphire Bragg gratings using 400 nm femtosecond laser radiation." Optics express 21, no. 4 (2013): 4591-4597.

80. Busch, Matthias, Wolfgang Ecke, Ines Latka, Daniel Fischer, Reinhardt Willsch, and Hartmut Bartelt. "Inscription and characterization of Bragg gratings in single-crystal sapphire optical fibres for high-temperature sensor applications." Measurement Science and Technology 20, no. 11 (2009): 115301.

10 LIST OF ACRONYMS AND ABBREVIATIONS

APC, angled physical contact

APD, avalanche photodetector

CCD, charge-coupled device

CL, confinement loss

CPT, Center for Photonics Technology

CTE, coefficient of thermal expansion

EFG, Edge defined Film Fed Growth

EMI, electromagnetic interference

FBG, fiber Bragg grating

FC, ferrule connector

FEM, Finite Element Method

FICT, fiber in ceramic tube

FM, fundamental mode

F-P, Fabry Perot

GI, graded index

GW, gigawatts

HF, hydrofluoric acid

HOM, higher order modes

ID, inner diameter

LHPG, Laser Heated Pedestal Growth

LMV, low modal volume

MMF, multimode fiber

NA, numerical aperture

OD, outer diameter

OSA, optical spectrum analyzer

PD, photodetector

PTFE, polytetrafluoroethylene

RDTS, Raman distributed temperature sensor

REIM, radial effective index method

SC, single crystal

SCSF, single crystal sapphire fiber

SEM, scanning electron microscope

SFBG, sapphire fiber Bragg grating

SI, step index

SLED, superluminescent light emitting diode

SMF, single mode fiber

SNR, signal to noise ratio

TIA, Telecommunications Industry Standard

TRL, Technology Readiness Level

U.S., United States

UV-VIS, ultraviolet-visible

VT, Virginia Tech